気象庁
Japan Meteorological Agency

CLIMATE CHANGE MONITORING REPORT 2020

July 2021

Published by the
Japan Meteorological Agency

3-6-9 Toranomon, Minato City, Tokyo 105-8431, Japan

Telephone +81 3 3584 8603
Facsimile +81 3 3434 9009
E-mail iao-jma@met.kishou.go.jp

CLIMATE CHANGE MONITORING REPORT
2020

July 2021

JAPAN METEOROLOGICAL AGENCY

Preface

The Japan Meteorological Agency (JMA) has published annual reports under the title of *Climate Change Monitoring Report* since 1996 to provide up-to-date information on climate change in Japan and around the world based on the outcomes of its observations and its monitoring of the atmosphere and oceans.

Extreme meteorological phenomena around the world in 2020 included abnormally high temperatures in Siberia and Australia as well as heavy rain in the middle and lower reaches of the Yangtze River in China. Japan experienced particularly significant rainfall and a lack of sunshine, especially in eastern and western parts during the Heavy Rain Event of July 2020. Snowfall in winter (December 2019 – February 2020) was quite low nationwide, and was the lowest since records began on the Sea of Japan side of northern and eastern Japan.

Long-term changes in the incidence of such extreme weather events are associated with global warming. The Meteorological Research Institute conducts research on the effects of climate change on individual phenomena, such as the Heavy Rain Event of July 2017 in Kyushu's Hokubu area, the Heavy Rain Event of July 2018, and Typhoon Hagibis (Typhoon No. 19 of 2019).

As global warming continues, the frequency and scale of extreme events are expected to increase. Urgent response to global warming-related climate change requires national and global efforts as promoted under initiatives including the Paris Agreement (a new international framework implemented in 2020) and the 2018 Climate Change Adaptation Act.

Against this background, JMA released *Climate Change in Japan 2020 – Assessment Report on Observed and Projected Climate Change in the Atmosphere, on Land and in Oceans –* in December 2020 in conjunction with Japan's Ministry of Education, Culture, Sports, Science and Technology. The report presents scientific expertise on climate change in Japan, including differences observed and future projections for the global average temperature changes detailed in the RCP 2.6 and 8.5 scenarios (called the "2°C and 4°C warming scenarios" in the report). The findings of previous *Climate Change Monitoring Report*s are also used here to help highlight observed changes.

This report is intended to raise awareness of climate change, and is expected to be particularly useful to related organizations and stakeholders worldwide in their responses to climate change.

HASEGAWA Naoyuki
Director-General
Japan Meteorological Agency

Index

News

I Record-high temperatures and low snowfall in winter 2020 (December 2019 – February 2020)

- ○ Winter seasonal mean temperatures were the highest on record since 1946/1947 in eastern and western Japan.
- ○ Winter seasonal snowfall amounts were the lowest on record since 1961/1962 on the Sea of Japan side.
- ○ Winter seasonal sunshine durations were significantly below normal on the Pacific side of eastern Japan, and winter seasonal precipitation amounts were significantly above normal on the Sea of Japan side of western Japan.

I.1 Climate conditions

Winter seasonal mean temperature anomalies in eastern and western Japan were +2.2 and +2.0°C, respectively, which were the highest on record since 1946/1947. At 111 of 153 surface meteorological observation stations nationwide, values were the highest or joint-highest on record. These conditions are attributed to fewer days with typical East Asian Winter Monsoon pressure patterns (featuring the Siberian High and the Aleutian Low) around the nation and weaker-than-normal southward cold-air flow over Japan. The country also experienced significantly lower snowfall than usual in winter 2019/20. On the Sea of Japan side of northern and eastern parts of the country in particular, cumulative snowfall amounts were the lowest for winter since 1961/62, at 44% and 7% of the normal, respectively. Winter seasonal precipitation amounts were significantly below normal on the Sea of Japan side of northern Japan, and were significantly above normal on the Sea of Japan side of western Japan. Winter seasonal sunshine durations were significantly below normal on the Pacific side of eastern Japan in association with periodic low-pressure systems passing over the mainland, and were significantly above normal in Okinawa/Amami due to high-pressure systems and weaker-than-normal cold-air inflow.

I.2 Characteristics of atmospheric circulation

The record-warm climate observed in winter 2019/2020 is primarily attributed to weaker-than-normal Siberian High and Aleutian Low conditions throughout the season, bringing fewer days with typical East Asian Winter Monsoon pressure patterns over and around Japan and consequent weaker-than-normal southward cold-air flow over the country. The synoptic-scale conditions observed nationwide were associated with subtropical jet stream meandering and the positive phase of the Arctic Oscillation (AO) pattern.

The subtropical jet stream meandered northward over and around Japan throughout the season. This may be attributable to southward meandering of the jet stream over southern China in response to suppressed convective activity over and around the Maritime Continent (Figure I.1). Subtropical jet stream meandering was also seen throughout Eurasia. The jet stream shifted northward over the Arabian Peninsula due to enhanced convective activity over the western Indian Ocean, reflecting higher-than-normal sea surface temperatures (SSTs) in the region. From

January 2020 onward, the meander partly originated from the northward meandering of the westerly jet stream over Europe.

In the Indian Ocean, higher-than-normal SSTs in the western part were likely associated with a positive Indian Ocean Dipole mode (IOD)[1] that persisted from summer to autumn 2019. These positive anomalies continued throughout the winter, and negative anomalies in the eastern part continued during December 2019. The suppressed convection observed over the Maritime Continent is considered to be linked to active convection around the equatorial date line, where SSTs were higher than normal.

From January 2020 onward, the positive phase of the AO pattern was dominant in the Northern Hemisphere. In association, a clear polar-front jet stream was observed in northern Eurasia with higher-than-normal temperatures over a broad area from Europe to eastern Siberia (Figure I.2). These conditions were favorable for weakening southward cold-air intrusion from Siberia to Japan. The persistent positive AO observed around March 2020 is considered a factor in the record-high temperatures seen for the month in Japan.

In addition to the above effects from meandering jet streams and a positive AO, a long-term trend of surface air temperature increase due to global warming and exceptionally higher-than-normal tropospheric temperatures throughout the mid-latitudes in the Northern Hemisphere are also considered to have contributed to these extremely warm winter conditions. On a longer time scale, winter surface temperatures worldwide and specifically in Japan have been rising at rates of around 0.79 and 1.19°C per century, respectively. The high tropospheric temperatures observed throughout the mid-latitudes of the Northern Hemisphere are partly attributed to the presence of the clear polar-front jet stream associated with the positive AO, which helped to keep the cold-air mass within the polar region.

Most winter extratropical cyclones in and around Japan took a course over or to the south of the mainland, exerting little or no influence over the northern part of the country. This led to lower snowfall than usual on the nation's Sea of Japan side, especially to the north.

Primary factors behind the record-warm climate conditions observed in winter 2019/2020 are summarized in Figure I.3.

---

[1] See the Glossary for terms relating to Indian Ocean Dipole mode event. The dipole mode index time series is published on JMA's website.
https://ds.data.jma.go.jp/tcc/tcc/products/elnino/iodevents.html

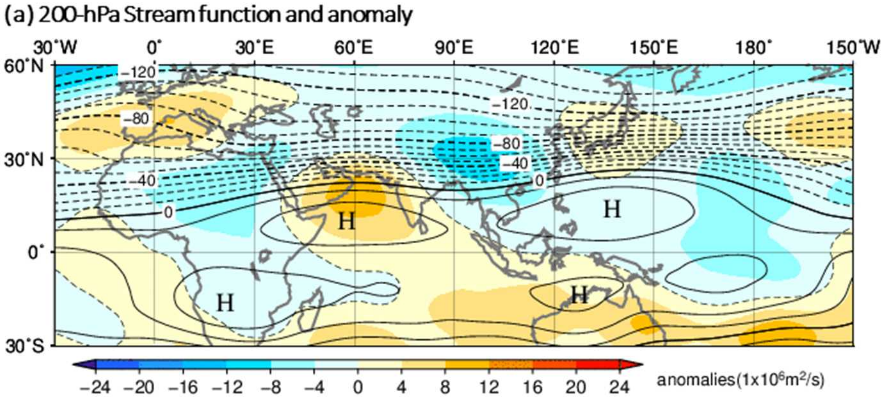

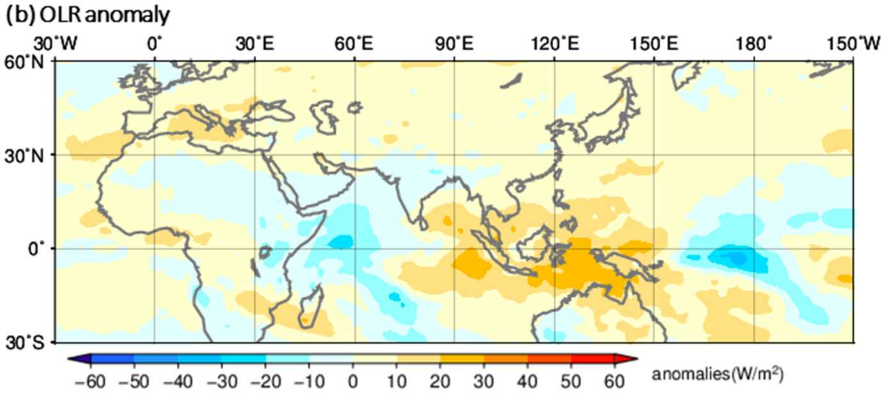

Figure I.1 (a) 200-hPa stream function (contours) and anomaly (shade), (b) outgoing longwave radiation (OLR) anomaly for December 2019 – February 2020

The contours are drawn at intervals of (a) 10 x 10^6 m^2 per s. The base period for the normal is 1981 – 2010.

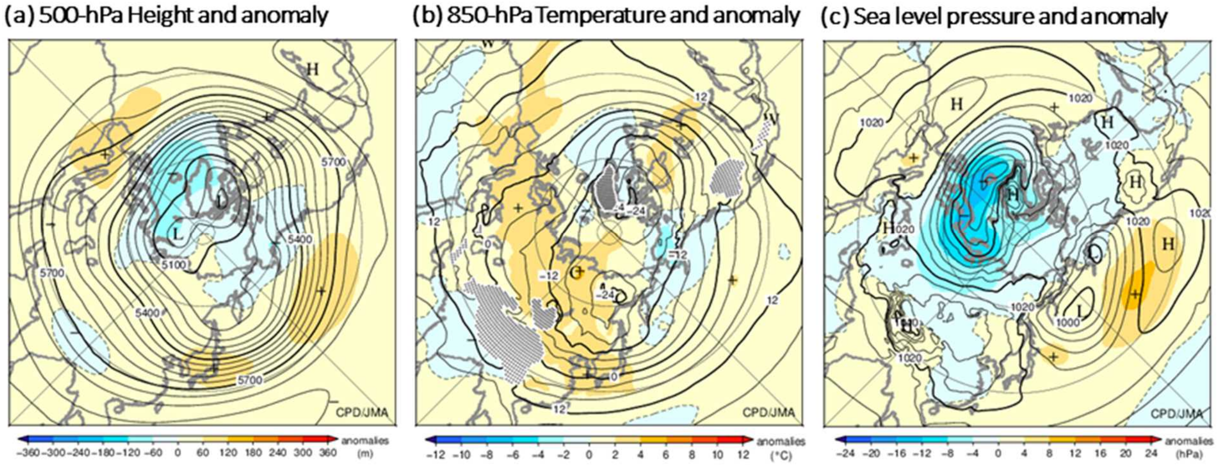

Figure I.2 (a) 500-hPa height (contours) and anomaly (shade), (b) 850-hPa temperature (contours) and anomaly (shade), (c) sea level pressure (contours) and anomaly (shade) for December 2019 – February 2020

The contours are drawn at intervals of (a) 60 m, (b) 4 °C, and (c) 4 hPa. The hatch patterns indicate areas with altitudes exceeding 1,600 m. The base period for the normal is 1981 – 2010.

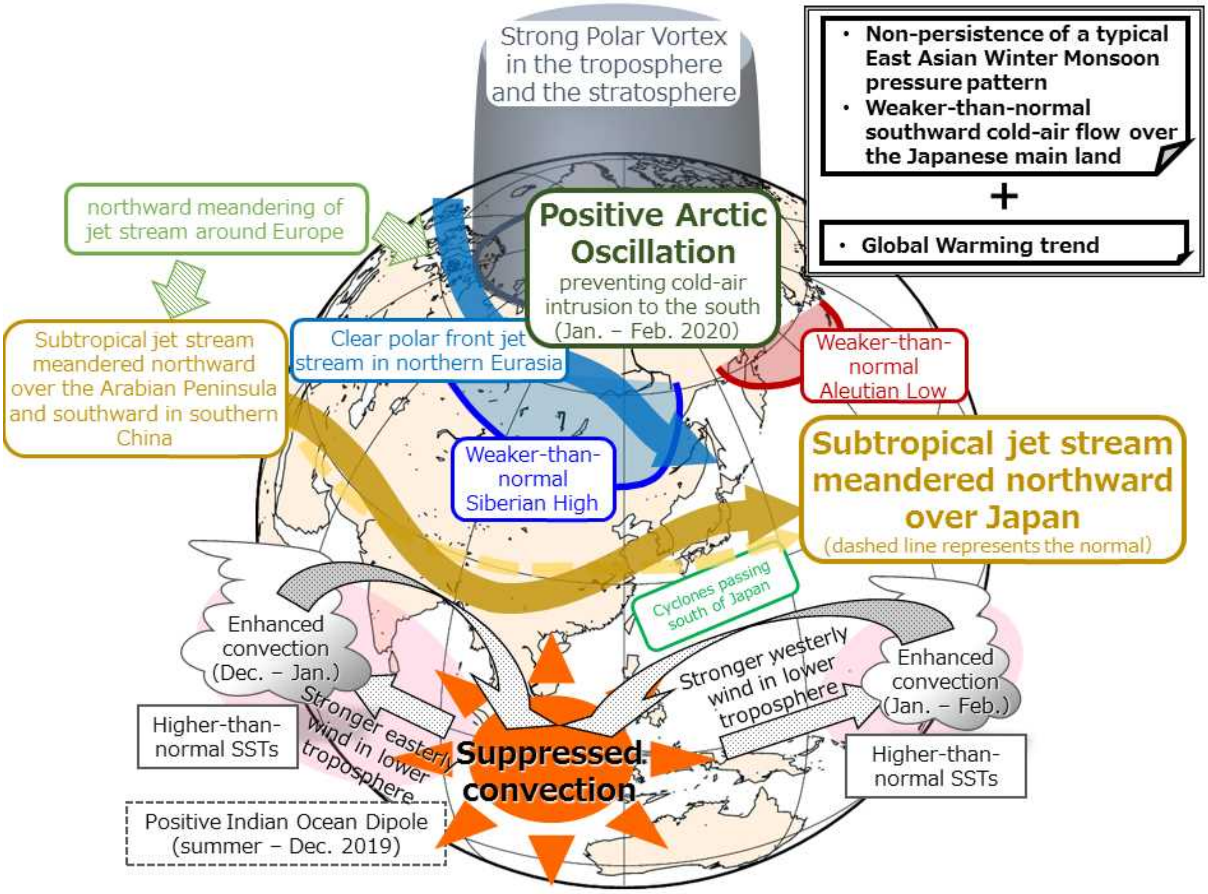

Figure I.3 Large-scale atmospheric circulation associated with the record-warm winter of 2019/2020

II Record-high sea-surface temperatures south of Japan in August 2020

○ Sea surface temperatures south of Japan were much higher than normal in August 2020, and monthly SSTs were the highest since 1982.

JMA monitors sea surface temperatures (SSTs) in the western North Pacific based on satellite, ship and buoy data. Figure II.1, which shows monthly mean SSTs and related anomalies for August 2020, indicates that SSTs south of Japan were much higher than normal, with values exceeding 30°C over wide areas. Figure II.2, which shows area-averaged SSTs for August (and related anomalies), indicates values of 29.8°C (+1.7°C) for the seas off Shikoku and Tokai (Area A in Fig.II.1), 29.3°C (+1.6°C) for the southeastern Kanto region (Area B) and 30.7°C (+2.1°C) for the region east of Okinawa (Area C) in 2020. These were all the highest monthly SSTs since 1982 (the values for 2020 are based on prompt analysis).

In August 2020, the Pacific High was strong over eastern/western Japan and the seas south of Japan, which experienced warm-air coverage and much more solar radiation than usual. These atmospheric conditions and lower typhoon passage over the area are likely factors behind the high SSTs recorded south of Japan.

In January 2021, the National Institute for Environmental Studies (NIES) announced that human-induced climate change had been behind the record-warm northwestern Pacific conditions of August 2020 (Hayashi et al. 2021).

The risk of extreme typhoons approaching Japan rises with higher SSTs around Japan, as such conditions support typhoon development and persistence. As high SSTs also affect socio-economic activity (via effects such as shifting of fishing grounds, aquacultural damage and coral breaching), there is a need for constant monitoring of oceanic variables.

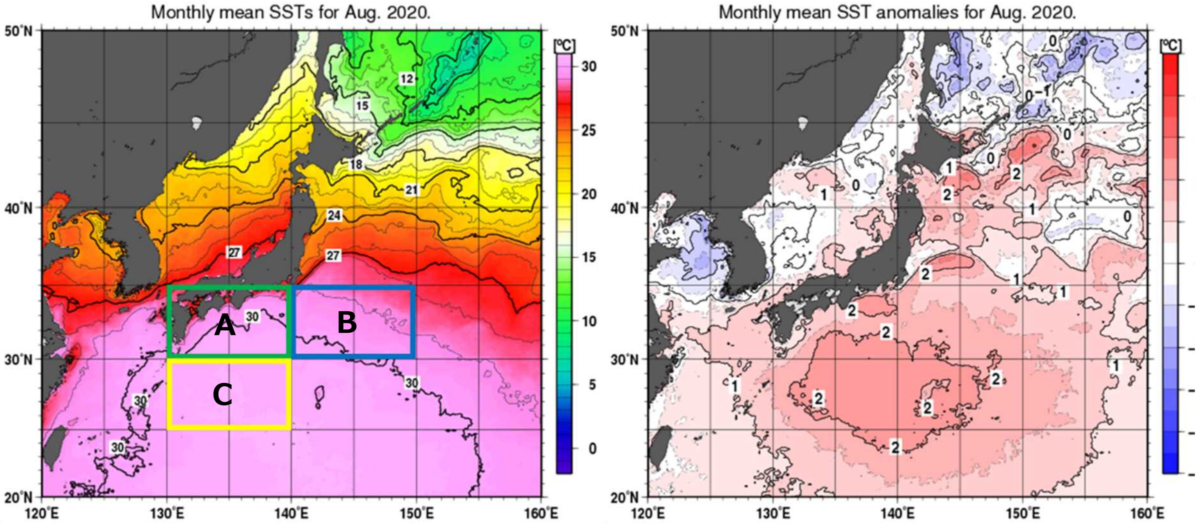

Monthly mean SSTs for Aug. 2020.

Monthly mean SST anomalies for Aug. 2020.

Figure II.1 August mean SSTs (left) and related anomalies (right)

SST anomalies are deviations from the normal for the period 1981 – 2010. SSTs for 2020 are prompt analysis values.

The green, blue and yellow rectangles in the figure on the left indicate averaged areas for the SST time-series representations in Figure II.2.

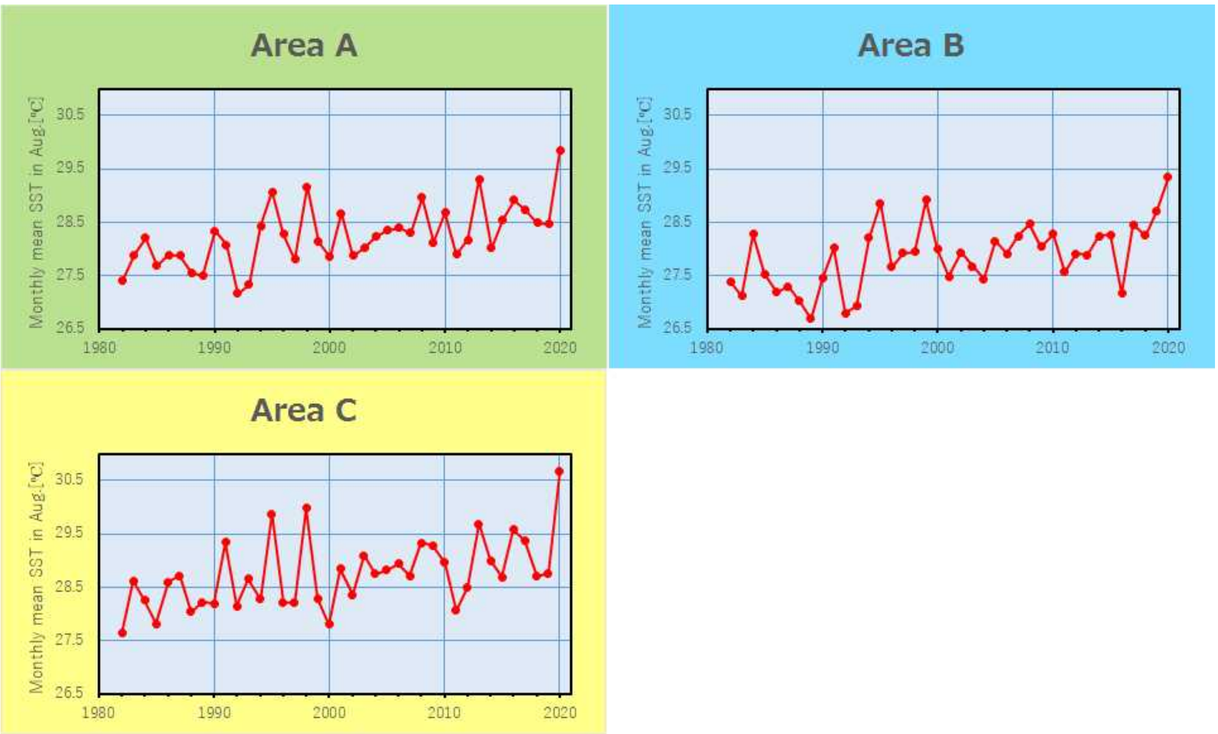

Figure II.2 Mean August sea surface temperatures since 1982 for the rectangle areas shown in Figure II.1

Values for 2020 are based on prompt analysis.

Chapter 1 Climate in 2020

1.1 Global climate summary

○ Extremely high temperatures were observed over a wide area of the world, and record-breaking monthly and seasonal mean temperatures in various countries were frequently reported. The global annual mean temperature was the highest since statistics began in 1891 tied with 2016.

○ Heavy rains in Asian countries and the central part of Eastern Africa, and hurricanes in the southern USA and Central America caused numerous disasters accompanied by many fatalities.

Major extreme climate events[1] and weather-related disasters that occurred in 2020 are shown in Figure 1.1-1 and Table 1.1-1.

Extremely high temperatures were observed over a wide area of the world ((1), (5), (8), (10), (12), (16), (18), (21), (24), (25), (26) in Fig. 1.1-1). In and around Siberia, extremely high temperatures were observed from January to November ((1) in Figure 1.1-1), and the annual mean temperature in Russia in 2020 was the highest on record since 1891 (Hydrometcenter of Russia).

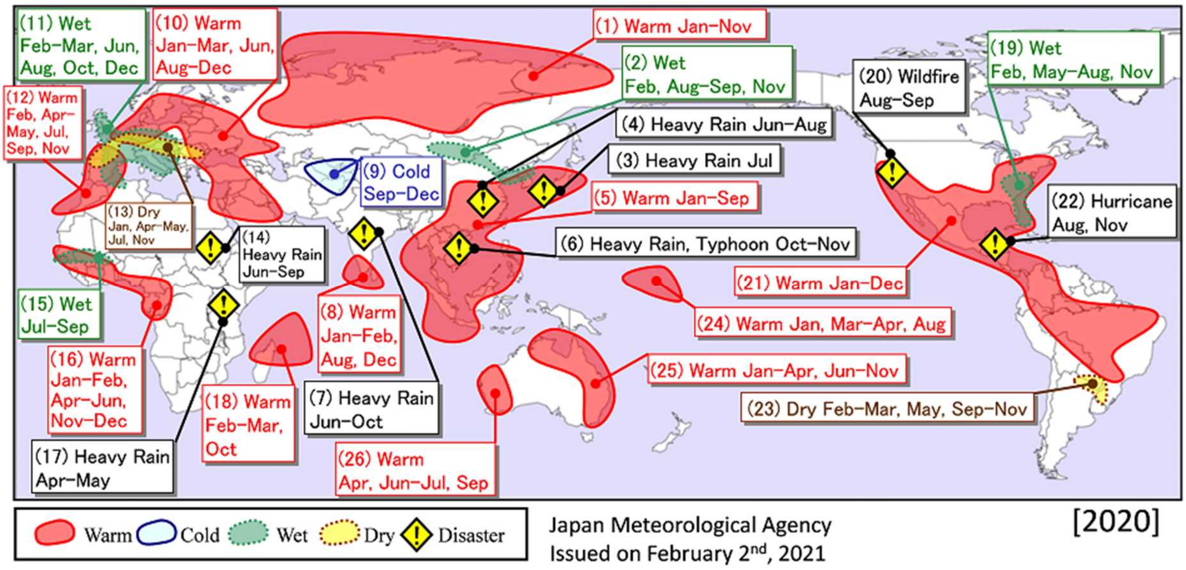

Figure 1.1-1 Major extreme events and weather-related disasters observed in 2020[2]

Schematic representation of major extreme climatic events and weather-related disasters occurring during the year.

"Warm", Cold", "Wet" and "Dry" indicate that monthly extreme events occurred three times or more during the year in these regions. JMA defines an extreme climate event as a phenomenon likely to happen only once every 30 years.

Data and information on disasters are based on official reports of the United Nations and national governments and databases of research institutes (EM-DAT).

EM-DAT: The Emergency Events Database - Université Catholique de Louvain (UCL) - CRED, D. Guha-Sapir - www.emdat.be, Brussels, Belgium.

---

[1] Extreme climate events are defined by anomalies or ratios to climatological normals. Normals represent mean climate conditions at given sites, and are currently based on a 30-year mean covering the period from 1981-2010.

[2] Annual distribution maps for major extreme climatic events and weather-related disasters after 2008 are provided at JMA's website.
https://ds.data.jma.go.jp/tcc/tcc/products/climate/annual/index.html

On the other hand, in and around the southern part of Central Asia, extremely low temperatures were observed from September to December ((9) in Figure 1.1-1).

From western to southern Europe, extremely high precipitation amounts was observed from February to March and in June, August, October and December ((11) in Figure 1.1-1). In the UK, monthly precipitation amount in February was the highest on record since 1862 (UK Met Office). On the other hand, from northern Argentina to southern Brazil, extremely low precipitation amounts was observed in February, March, May and September to November ((23) in Figure 1.1-1).

Heavy rains in the middle and lower Yangtze River basin from June to August ((4) in Figure 1.1-1) left a total of more than 270 persons dead or missing in China (the government of China). Heavy rains, four Typhoons ("SAUDEL", "MOLAVE", "GONI", and "VAMCO") and two Tropical Storms ("LINFA" and "NANGKA") in October and November ((6) in Figure 1.1-1) caused more than 340 fatalities from the Philippines to the Indochina Peninsula (Government of the Philippines, Government of Viet Nam and European Commission). Heavy rains from June to October ((7) in Figure 1.1-1) caused more than 2,700 fatalities in and around South Asia (Government of India, Government of Nepal, Government of Pakistan, EM-DAT). Heavy rains in western Yemen from June to August, and in Sudan and Niger from June to September ((14) in Figure 1.1-1) caused more than 370 fatalities (UNHCR, EMDAT). In the western United States, wildfires ((20) in Figure 1.1-1) in August and September caused more than 30 fatalities (US Government). In the southern USA and Central America, Hurricane LAURA in August and Hurricanes ETA and IOTA in November ((22) in Figure 1.1-1) caused more than 360 fatalities (US Government, OCHA, EMDAT).

Annual mean temperatures were above normal in the most parts of the world, and were very high in Siberia, from the eastern part of East Asia to Southeast Asia, in and around Europe, in and around Madagascar, from the southern part of North America to South America, and in Australia (Figure 1.1-2).

Annual precipitation amounts were above normal from Western Siberia to the eastern part of East Asia, in the southern part of Southeast Asia, from the southern part of Central Asia to South Asia, from northern to western Europe, in Western Africa, from the eastern part of North America to Caribbean countries, in the eastern part of South America, and from central to southeastern Australia. Annual precipitation amounts were below normal from the western part of Central Asia to the central part of East Asia, from the central to western part of Northern Africa, from the western USA to central Mexico, and in the southern part of South America (Figure 1.1-3).

Table 1.1-1 Major extreme events and weather-related disasters occurring in 2020

No.	Event
(1)	Warm: in and around Siberia (January – November)
(2)	Wet: from central Mongolia to the Korean Peninsula (February, August – September, November)
(3)	Heavy Rain: from eastern to western Japan (July)
(4)	Heavy Rain: China (June – August)
(5)	Warm: from the eastern part of East Asia to Southeast Asia (January – September)
(6)	Heavy Rain and Typhoon: from the Philippines to the Indochina Peninsula (October – November)
(7)	Heavy Rain: in and around South Asia (June – October)
(8)	Warm: from southern India to Sri Lanka (January – February, August, December)
(9)	Cold: in and around the southern part of Central Asia (September – December)
(10)	Warm: from northern Europe to the central Middle East (January – March, June, August – December)
(11)	Wet: from western to southern Europe (February – March, June, August, October, December)
(12)	Warm: from western Europe to the western part of Northern Africa (February, April – May, July, September, November)
(13)	Dry: from eastern to southwestern Europe (January, April – May, July, November)
(14)	Heavy Rain: western Yemen, Sudan, Niger (June – September)
(15)	Wet: from the central to western part of Western Africa (July – September)
(16)	Warm: from the western part of Western Africa to the western part of Middle Africa (January – February, April – June, November – December)
(17)	Heavy Rain: in and around the central part of Eastern Africa (April – May)
(18)	Warm: in and around northern Madagascar (February – March, October)
(19)	Wet: from the eastern to southeastern USA (February, May – August, November)
(20)	Wildfire: The western USA (August – September)
(21)	Warm: from the southern part of North America to the central part of South America (January – December)
(22)	Hurricane: from the southern USA to Central America (August, November)
(23)	Dry: from northern Argentina to southern Brazil (February – March, May, September – November)
(24)	Warm: in and around southeastern Micronesia (January, March – April, August)
(25)	Warm: from northern to southeastern Australia (January – April, June – November)
(26)	Warm: western Australia (April, June – July, September)

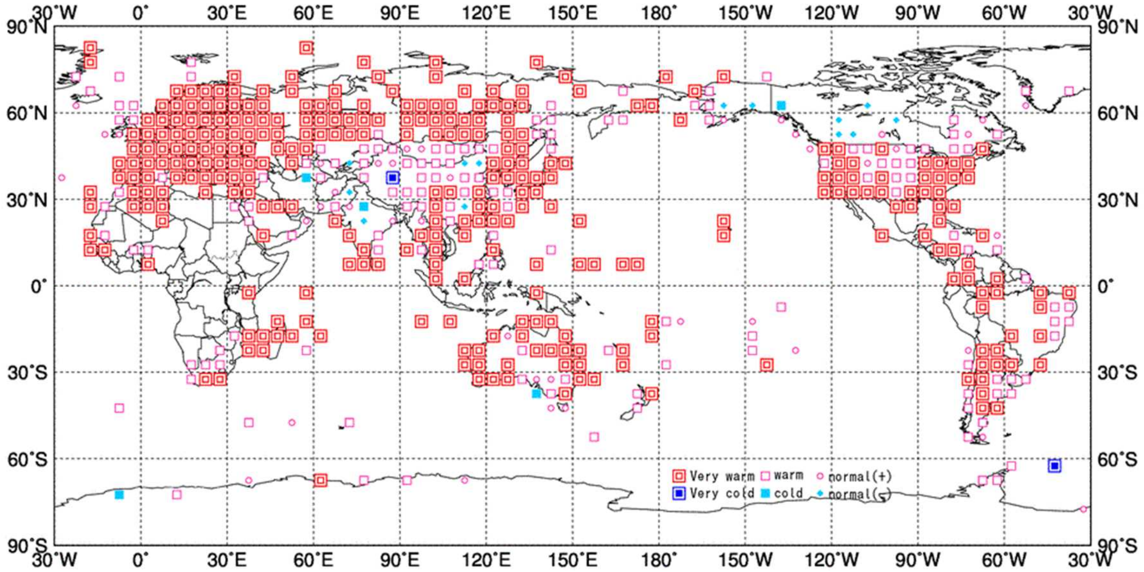

Figure 1.1-2　Annual mean temperature anomalies in 2020[3]

Categories are defined by the annual mean temperature anomaly against the normal divided by its standard deviation and averaged in 5° × 5° grid boxes. Red/blue marks indicate values above/below the normal calculated for the period from 1981 to 2010. The thresholds of each category are –1.28, –0.44, 0, +0.44 and +1.28[4]. Areas over land without graphical marks are those where observation data are insufficient or normal data are unavailable.

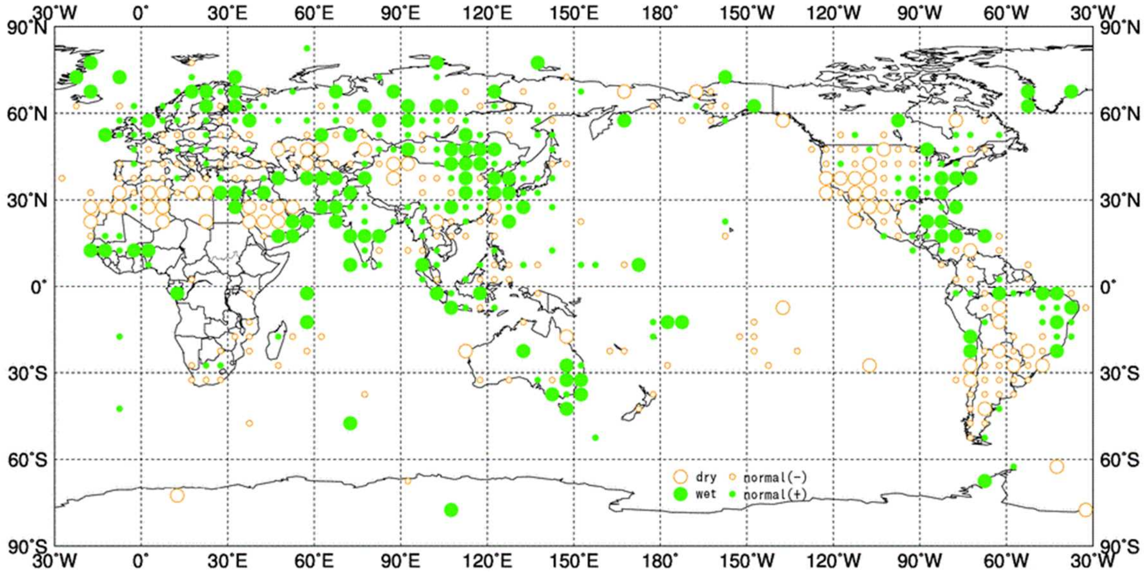

Figure 1.1-3　Annual total precipitation amount ratios in 2020

Categories are defined by the annual precipitation ratio to the normal averaged in 5° × 5° grid boxes. Green/yellow marks indicate values above/below the thresholds. The thresholds of each category are 70, 100 and 120% of the normal calculated for the period from 1981 to 2010. Areas over land without graphical marks are those where observation data are insufficient or normal data are unavailable.

---

[3] Distribution maps for normalized annual mean temperature anomaly and precipitation amount ratio to normal after 2008 are provided at JMA's website.
https://ds.data.jma.go.jp/tcc/tcc/products/climate/annual/index.html

[4] In normal distribution, values of 1.28 and 0.44 correspond to occurrence probabilities of less than 10 and 33.3%, respectively.

1.2 Climate in Japan[5]

○ Annual mean temperatures were significantly above normal nationwide due to warmer conditions throughout most of the period.

○ In 2019/2020, seasonal mean temperatures were the highest on record for winter since 1946/1947 in eastern and western Japan, and seasonal snowfall amounts were the lowest on record for winter since 1961/1962 on the Sea of Japan side.

○ In July 2020, areas from western to eastern Japan experienced record-heavy rainfall and record-low sunshine durations.

1.2.1 Annual characteristics

The annual climate anomaly/ratio for Japan in 2020 is shown in Figure 1.2-1.

○ Annual mean temperatures were significantly above normal nationwide.

○ Annual precipitation was significantly above normal on the Sea of Japan side of western Japan, above normal on the Sea of Japan side of northern Japan, the Pacific side of eastern/western Japan and in Okinawa/Amami, and near normal on the Pacific side of northern Japan and on the Sea of Japan side of eastern Japan.

○ Annual sunshine durations were above normal on the Pacific side of eastern Japan and western Japan, below normal on the Pacific side of northern and eastern Japan, and near normal in Okinawa/Amami.

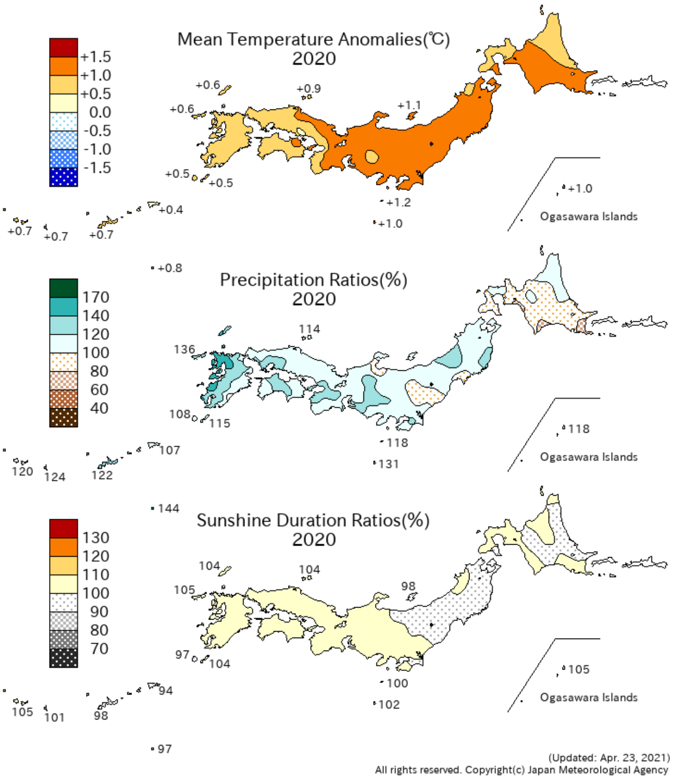

Figure 1.2-1 Annual climate anomaly/ratio for Japan in 2020
The base period for the normal is 1981 – 2010.

---

[5] The term *significantly above normal* is used for cases in which observed mean temperatures or precipitation amounts exceed the 90th percentile for the base period (1981 – 2010), and *significantly below normal* is used when the corresponding figures fall below the 10th percentile.

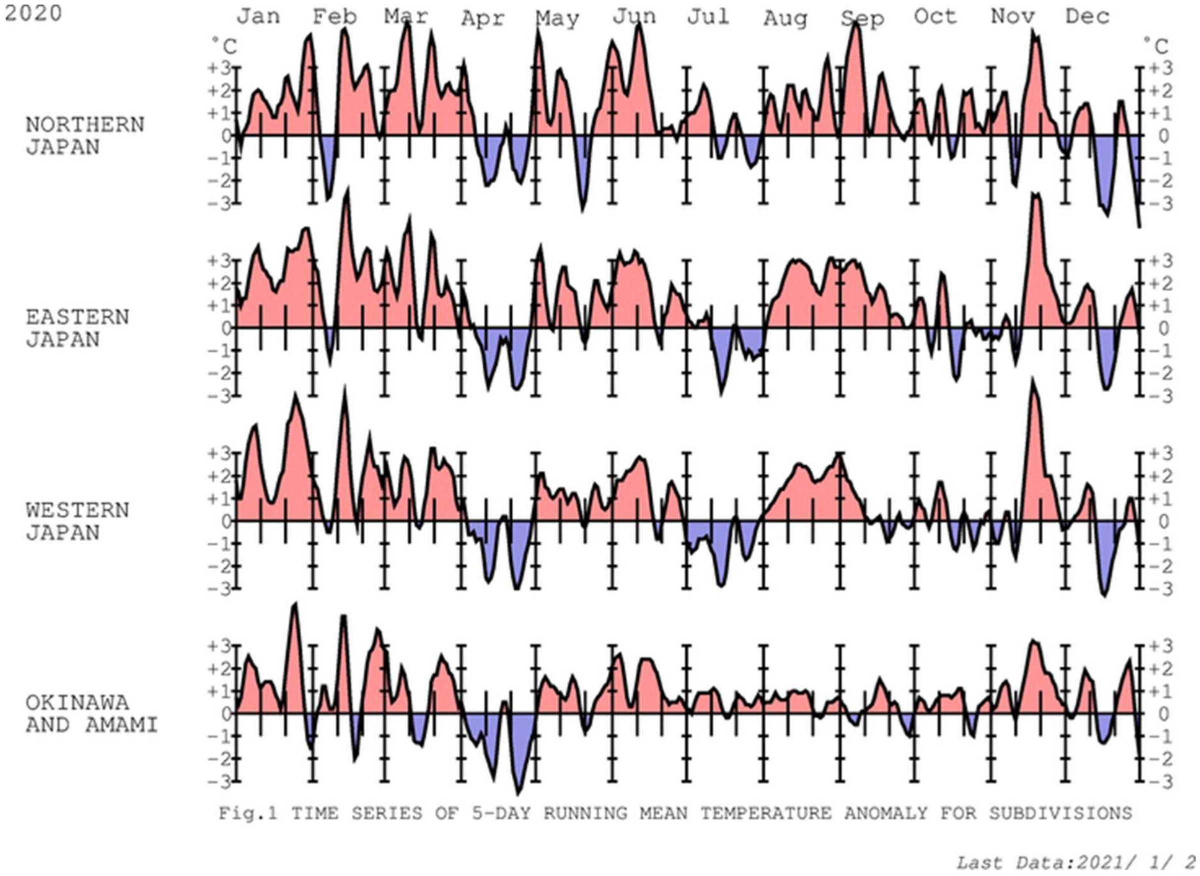

Figure 1.2-2 Five-day running mean temperature anomaly for divisions (January – December 2020)

The base period for the normal is 1981 – 2010.

1.2.2 Seasonal characteristics

Five-day running mean temperature anomalies for different divisions (January – December 2020) are shown in Figure 1.2-2, and seasonal anomalies/ratios for Japan in 2020 are shown in Figure 1.2-3. Numbers of observatories reporting record monthly and annual mean temperatures, precipitation amounts and sunshine durations (2020) are shown in Table 1.2-1.

(1) Winter (December 2019 – February 2020) (See topic for details)

- Seasonal mean temperatures were the highest on record for winter since 1946/1947 in eastern and western Japan.
- Seasonal snowfall amounts were the lowest on record for winter since 1961/1962 on the Sea of Japan side of northern and eastern Japan.
- Seasonal precipitation amounts were significantly below normal on the Sea of Japan side of northern Japan and significantly above normal on the Sea of Japan side of western Japan.

Seasonal mean temperatures were the highest on record for winter since 1946/1947 in eastern and western Japan in association with a weaker-than-normal winter monsoon and cold-air inflow. Seasonal snowfall amounts were the lowest on record for winter since 1961/1962 on the Sea of Japan side of northern and eastern Japan. Seasonal precipitation amounts were significantly below normal on the Sea of Japan side of northern Japan and significantly above normal on the Sea of Japan side of western Japan. Seasonal sunshine durations were significantly below normal on the Pacific side of eastern Japan in association with the periodic passing of low-pressure systems over mainland Japan, and significantly above normal in Okinawa/Amami due to high-pressure systems and weaker-than-normal cold-air inflow.

(2) Spring (March – May 2020)

- Seasonal mean temperatures were significantly above normal in northern Japan.
- Seasonal sunshine durations were significantly above normal in western Japan and on the Pacific side of eastern Japan.
- Seasonal precipitation amounts were above normal in northern Japan and Okinawa/Amami.

Seasonal mean temperatures were significantly above normal in northern Japan due to warm-air inflow into the region. Seasonal sunshine durations were significantly above normal in western Japan and on the Pacific side of eastern Japan, as these regions were repeatedly under the influence of high-pressure systems. Seasonal precipitation amounts were above normal in northern Japan and Okinawa/Amami due to developing low-pressure systems, fronts and moist southerly air inflow.

(3) Summer (June – August 2020)

- Seasonal mean temperatures were significantly above normal in eastern Japan and Okinawa/Amami.
- Seasonal precipitation amounts were significantly above normal in eastern and western Japan and Okinawa/Amami.
- Seasonal sunshine durations were below normal on the Sea of Japan side of eastern Japan and Okinawa/Amami.

Due to stagnation of the active Meiyu-Baiu front and moist southerly air inflow, seasonal precipitation amounts were significantly above normal in eastern and western Japan and Okinawa/Amami, and seasonal sunshine durations were below normal on the Sea of Japan side of eastern Japan and Okinawa/Amami. In particular, areas from western to eastern Japan experienced record-heavy rainfall and record-low sunshine durations in July.

In August, the North Pacific high was stronger than normal and extended toward western and eastern Japan, which brought significantly above-normal sunshine durations and significantly below-normal rainfall. Seasonal mean temperatures were significantly above normal in eastern Japan and Okinawa/Amami and above normal in western and northern Japan.

(4) Autumn (September – November 2020)

- Seasonal mean temperatures were significantly above normal in northern Japan and Okinawa/Amami.
- Seasonal precipitation amounts were above normal on the Pacific side of western Japan.
- Seasonal sunshine durations were below normal in northern Japan.

Seasonal mean temperatures were significantly above normal in northern Japan and Okinawa/Amami due to remarkable warm-air inflow in the second half of November. Seasonal precipitation amounts were above normal on the Pacific side of western Japan and below normal on the Pacific side of northern Japan, the Sea of Japan side of eastern Japan and in Okinawa/Amami. Seasonal sunshine durations were below normal in northern Japan and above normal on the Sea of Japan side of eastern and western Japan.

(5) Early Winter (December 2020)

Monthly mean temperatures were below normal in northern and western areas due to cold-air inflow mainly in the middle of December. Monthly precipitation amounts were significantly below normal on the Pacific side of northern Japan, and monthly sunshine durations were significantly below normal on the Sea of Japan side of northern Japan due to the strong winter monsoon. In Okinawa/Amami, monthly precipitation amounts were significantly above normal and monthly sunshine durations were significantly below normal due to the active front and moist-air inflow.

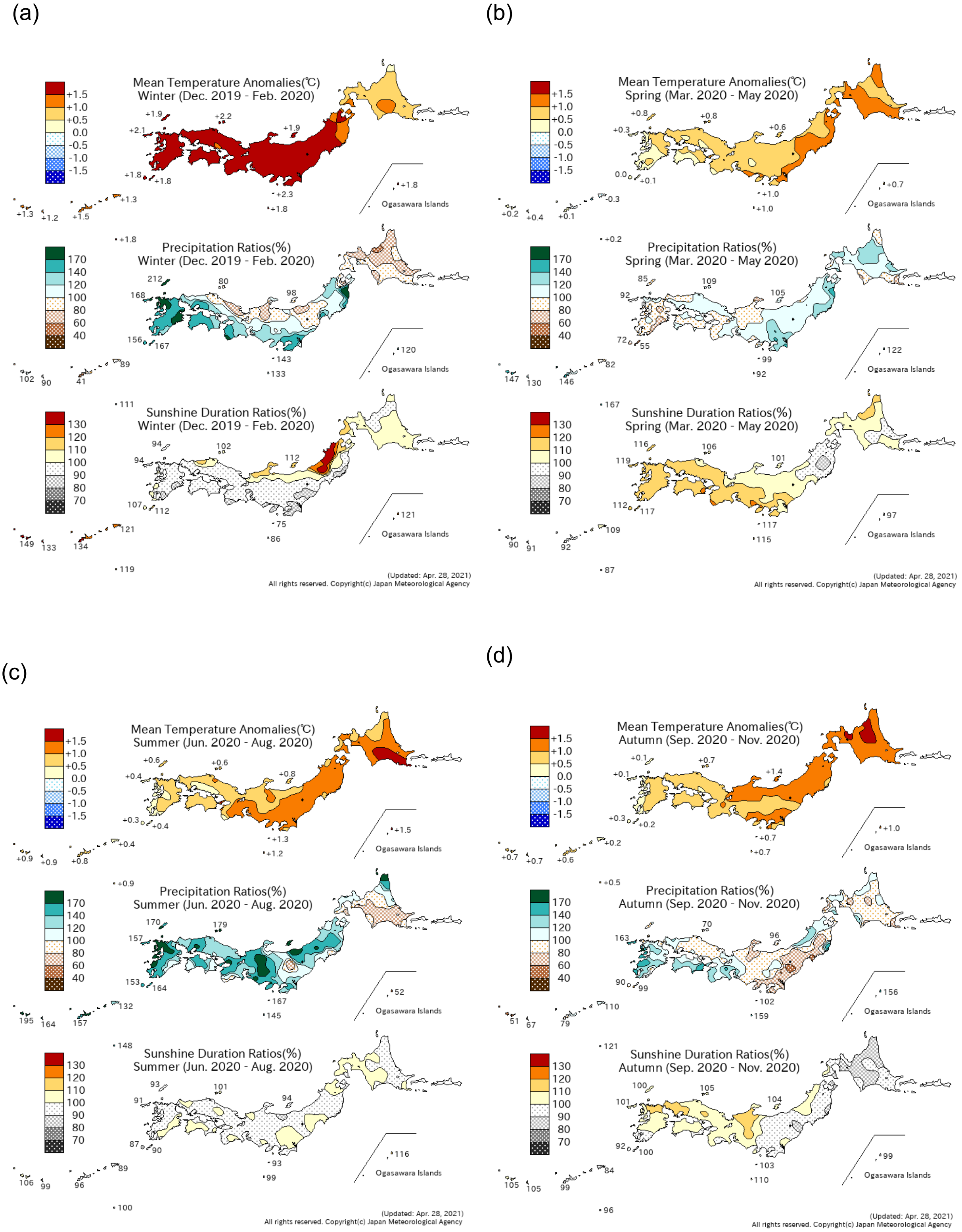

Figure 1.2-3 Seasonal anomalies/ratios for Japan in 2020
(a) Winter (December 2019 to February 2020), (b) spring (March to May 2020), (c) summer (June to August 2020), (d) autumn (September to November 2020). The base period for the normal is 1981 – 2010.

Table 1.2-1 Number of observatories reporting record(include tie record) monthly and annual mean temperatures, precipitation amounts and sunshine durations (2020)

From 153 surface meteorological stations across Japan.

	Temperature		Precipitation amount		Sunshine duration	
	Highest	Lowest	Heaviest	Lightest	Longest	Shortest
January	105		2	4		
February	23			2	1	
March	38					
April			5	2	26	
May	2		1	6		
June	50			1		
July	2		17		1	46
August	50		1	5	12	
September	1					
October	1					
November	1			1	4	
December			3	9	6	4
year	36		1			

1.3 Atmospheric circulation and oceanographic conditions[6]

○ In winter 2019/2020, seasonal mean temperatures from Europe to East Asia were widely higher than normal in association with the Arctic Oscillation in its positive phase dominating atmospheric circulation over the Northern Hemisphere.

○ Subsequent to a positive Indian Ocean Dipole event from summer to autumn 2019, sea surface temperatures (SSTs) in the Indian Ocean were higher than normal throughout 2020. In July 2020, tropical convection was enhanced over the western Indian Ocean and suppressed in the Asian monsoon region, which delayed the northward migration of the subtropical jet stream over Eurasia and induced a southwestward expansion of the North Pacific Subtropical High, resulting in an unusually persistent Meiyu-Baiu front[7] from the Yangtze River basin to Japan.

○ A La Niña event emerged and developed from summer to autumn 2020 onward in association with remarkably positive SST anomalies in the western equatorial Pacific and remarkably negative anomalies from central to eastern parts. The tropical lower-tropospheric circulation anomalies observed in autumn from the Indian Ocean to the Pacific are associated with the prevailing La Niña conditions.

Monitoring of atmospheric and oceanographic conditions (e.g., upper air flow, tropical convective activity, sea surface temperatures (SSTs) and the Asian monsoon) is key to understanding the causes of extreme weather events[8]. This section briefly outlines the

---

[6] See the Glossary for terms relating to sea surface temperature variations and monsoon.

[7] The Meiyu-Baiu front causes the East Asian rainy season observed before mid-summer. It appears at the border between a warm, moist tropical air mass and a relatively cool, dry air mass over the Asian continent and subpolar seas in early summer, and is characterized by a significant gradient of equivalent potential temperature.

[8] The main charts used for monitoring of atmospheric circulation and oceanographic conditions are: sea surface temperature

characteristics of atmospheric circulation and oceanographic conditions seen in 2020.

1.3.1 Characteristics of individual seasons[9]

(1) Winter (December 2019 – February 2020)

Remarkably positive SST anomalies were observed in the western part of the equatorial Pacific. Subsequent to a positive Indian Ocean Dipole event occurring from summer to autumn 2019, remarkably positive SST anomalies were observed over most of the tropical Indian Ocean (Figure 1.3-1 (a)).

Tropical convection was enhanced over the western tropical Indian Ocean, around the date line in the equatorial Pacific, and over the latitude band of 10°N in the central tropical North Pacific, and was suppressed over the Maritime Continent (Figure 1.3-1 (b)). In the lower troposphere of the tropical region, cyclonic circulation anomalies straddling the equator were seen west of the date line in the tropical Pacific, and anti-cyclonic circulation anomalies straddling the equator were seen from the central tropical Indian Ocean to the Maritime Continent (Figure 1.3-1 (c)).

In the 500-hPa height field, positive anomalies were seen over Japan, the mid-latitude central and eastern North Pacific, and southern Europe, and negative anomalies were seen over Alaska and near Iceland (Figure 1.3-1 (d)). The westerly jet stream shifted southward from its normal position from northern South Asia to southern China, and meandered northward over the mid-latitude western North Pacific. The sea level pressure (SLP) field indicates that the Arctic Oscillation in its positive phase dominated the Northern Hemisphere, and that the Aleutian Low and the Siberian High were weaker than normal (Figure 1.3-1 (e)). Temperatures at 850 hPa were above normal over eastern North America and a wide area from Europe to East Asia, and below normal over Alaska and the seas south of Greenland (Figure 1.3-1 (f)).

(2) Spring (March – May 2020)

Remarkably positive SST anomalies were observed in the western equatorial Pacific and most of the tropical Indian Ocean (Figure 1.3-2 (a)).

Tropical convection was enhanced over the southwestern tropical Indian Ocean and suppressed over the South China Sea, from the central to the eastern tropical South Pacific, and over northwestern South America (Figure 1.3-2 (b)). In the lower troposphere of the tropical region, anti-cyclonic circulation anomalies were seen from east of New Guinea to the central tropical South Pacific. (Figure 1.3-2 (c)).

In the 500-hPa height field, the polar vortex in the Northern Hemisphere was stronger than normal. A wave train was dominant from northern Eurasia to the northern part of the North Pacific

---

(SST) maps representing SST distribution for monitoring of oceanographic variability elements such as El Niño/La Niña phenomena; outgoing longwave radiation (OLR) maps representing the strength of longwave radiation from the earth's surface under clear sky conditions into space or from the top of clouds under cloudy conditions into space for monitoring of convective activity; 850-hPa stream function maps representing air flow in the lower troposphere for monitoring of atmospheric circulation variability elements such as the Pacific High and the monsoon trough associated with the Asian summer monsoon; 500-hPa height maps representing air flow at a height of approximately 5,500 meters for monitoring of atmospheric circulation variability elements such as westerly jet streams and the Arctic Oscillation; sea level pressure maps representing air flow and pressure systems on the earth's surface for monitoring of the Pacific High, the Siberian High, the Arctic Oscillation and other phenomena; 850-hPa temperature maps representing air temperature at a height of approximately 1,500 meters; and temperature calculated from thickness in the troposphere for monitoring of mean temperature of the troposphere.

[9] JMA publishes Monthly Highlights on the Climate System including information on the characteristics of climatic anomalies and extreme events around the world, atmospheric circulation and oceanographic conditions. It can be found at https://ds.data.jma.go.jp/tcc/tcc/products/clisys/highlights/index.html.

with positive 500-hPa height anomalies over Western and Central Siberia and the south of Alaska, and negative anomalies over northeastern Europe (Figure 1.3-2 (d)). The subtropical jet stream shifted southward from its normal position from southern Eurasia to Japan, and the westerly jet stream was stronger than normal from North America to the central North Atlantic. Positive SLP anomalies were seen over central Europe and the south of Alaska, and negative SLP anomalies were seen from the northern polar region to Western Russia and over Japan (Figure 1.3-2 (e)). Temperatures at 850-hPa were above normal over Western and Central Siberia and the south of Alaska, and below normal over Canada, northeastern Europe and northern South Asia (Figure 1.3-2 (f)).

(3) Summer (June – August 2020)

A La Niña event emerged in association with remarkably positive SST anomalies in the western equatorial Pacific and remarkably negative anomalies in the eastern part. In the Indian Ocean, remarkably positive SST anomalies were observed over most of the tropical region (Figure 1.3-3 (a)).

Tropical convection was enhanced over the western Indian Ocean and suppressed over the western and central equatorial Pacific (Figure 1.3-3 (b)). In the lower troposphere of the tropical region, anti-cyclonic circulation anomalies straddling the equator were seen over the western tropical Pacific (Figure 1.3-3 (c)).

In the 500-hPa height field, positive anomalies were seen over the seas southeast of Japan, the latitude band of 40°N in the central and eastern North Pacific, and central Canada, and negative anomalies were seen from the Caspian Sea to northwestern East Asia and over northwestern North America (Figure 1.3-3 (d)). The subtropical jet stream shifted southward from its normal position from Central Asia to western East Asia. The North Pacific Subtropical High (NPSH) expanded southwestward of its climatological extent over the seas south of Japan and toward mainland Japan from early to mid-August (Figure 1.3-3 (e)). In July, suppressed convection in the Asian monsoon region delayed the northward migration of the subtropical jet stream over Eurasia and induced the southwestward expansion of the NPSH, resulting in an unusually persistent Meiyu-Baiu front from the Yangtze River basin to Japan and severe damage due to a series of heavy rainfall events in the region (Figure 1.1-1 (3), (4)). Temperatures at 850-hPa were above normal from the northern polar region to Central Siberia, over the seas east of Japan, and from central Canada to the western USA, and below normal over the western part of the Sea of Okhotsk (Figure 1.3-3 (f)).

(4) Autumn (September – November 2020)

In the equatorial Pacific, remarkably positive SST anomalies were observed west of 150°E, and remarkably negative anomalies were observed in central to eastern parts in association with the development of La Niña conditions (Figures 1.3-4 (a)).

Tropical convection was enhanced from the northern Indian Ocean to the Maritime Continent and over the Caribbean Sea, and was suppressed from west of the date line in the equatorial Pacific to the central tropical North Pacific (Figure 1.3-4 (b)). In the lower troposphere of the tropical region, cyclonic circulation anomalies straddling the equator were seen over the tropical Indian Ocean and the tropical Atlantic, and anti-cyclonic circulation anomalies straddling the equator were seen over the tropical Pacific (Figure 1.3-4 (c)). Lower-tropospheric circulation anomalies observed from the tropical Indian Ocean to the tropical Pacific were associated with the prevailing La Niña conditions.

In the 500-hPa height field, the polar vortex in the Northern Hemisphere shifted toward North America. Positive anomalies in the 500-hPa height field were seen over a wide range encompassing northern Eurasia, southern China, the seas southeast of Japan and the area from the eastern North Pacific via the USA to the mid-latitude central North Atlantic (Figure 1.3-4 (d)). The subtropical jet stream over Eurasia shifted northward from its normal position, and the westerly jet stream shifted northward from its normal position over the North Pacific and the area from eastern North America to the North Atlantic. In the SLP field, a clear annular pattern was seen with positive anomalies over a wide area of the mid-latitudes in the Northern Hemisphere and negative anomalies over the northern polar region. In particular, positive SLP anomalies were significant over the mid-latitude North Atlantic and from Western Russia to Central Asia (Figure 1.3-4 (e)). Temperatures at 850-hPa were above normal over a wide area of northern Eurasia and the eastern Mediterranean Sea, and were below normal over Central Asia (Figure 1.3-4 (f)).

(a) SST anomaly

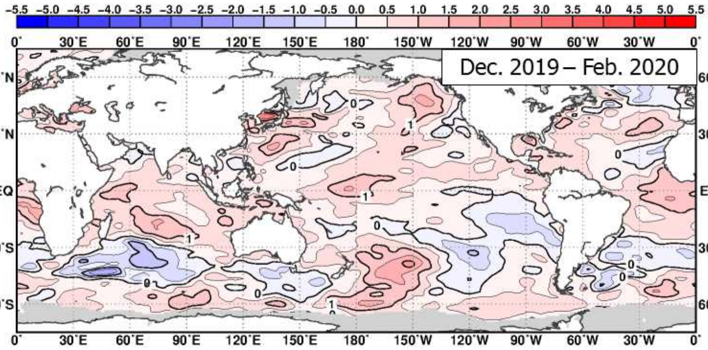

(b) OLR anomaly

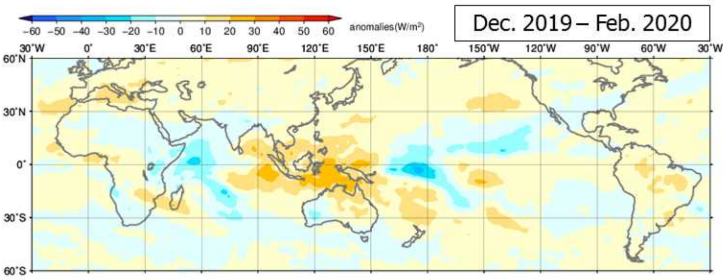

(c) 850-hPa stream function and anomaly

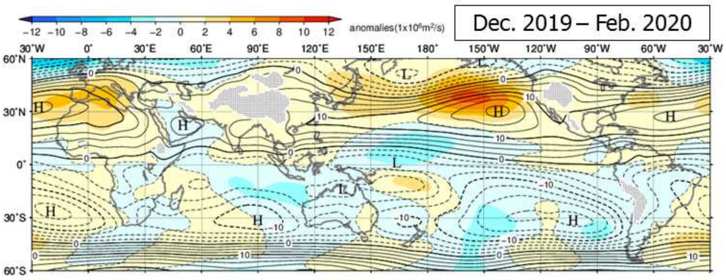

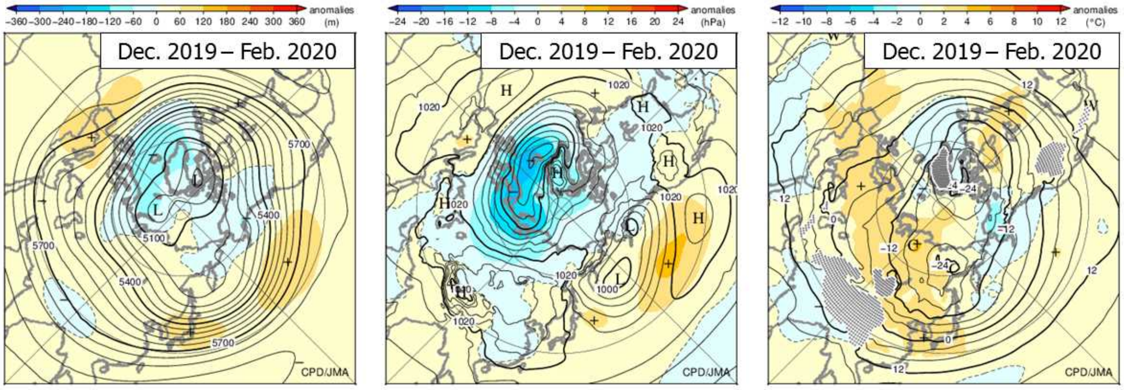
(d) 500-hPa height and anomaly

(e) SLP and anomaly

(f) 850-hPa temp. and anomaly

Figure 1.3-1 Three-month mean (a) sea surface temperature (SST) anomaly, (b) outgoing longwave radiation (OLR) anomaly, (c) 850-hPa stream function and anomaly, (d) 500-hPa height and anomaly in the Northern Hemisphere (NH), (e) sea level pressure (SLP) and anomaly in NH, and (f) 850-hPa temperature and anomaly in NH (December 2019 – February 2020)

The base period for the normal is 1981 – 2010. (a) The contour interval is 0.5°C. Sea ice coverage areas are shaded in gray. (b) Negative (cold color) and positive (warm color) OLR anomalies show enhanced and suppressed convection, respectively, compared to the normal. (c) The contour interval is 2.5 x 10^6 m^2 per s. “H” and “L” denote high- and low-pressure systems, respectively. Original data provided by NOAA. (d) Contours show 500-hPa height at intervals of 60 m, and shading indicates height anomalies. “H” and “L” denote high- and low-pressure systems, respectively. (e) Contours show sea level pressure at intervals of 4 hPa, and shading indicates sea level pressure anomalies. “H” and “L” denote high- and low-pressure systems, respectively. (f) Contours show temperature at intervals of 4 degree C, and shading indicates temperature anomalies. “W” and “C” denote warm and cold conditions, respectively.

(a) SST anomaly

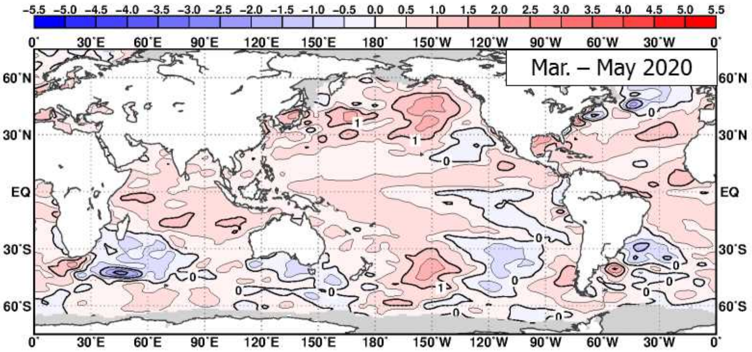

(b) OLR anomaly

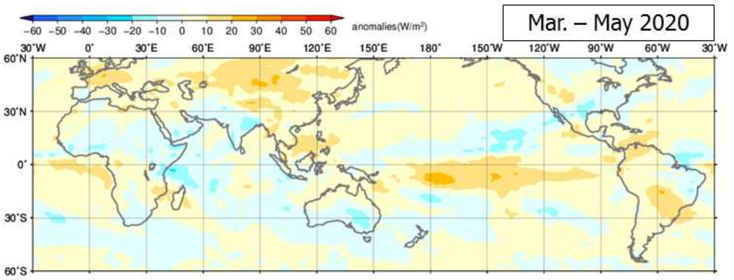

(c) 850-hPa stream function and anomaly

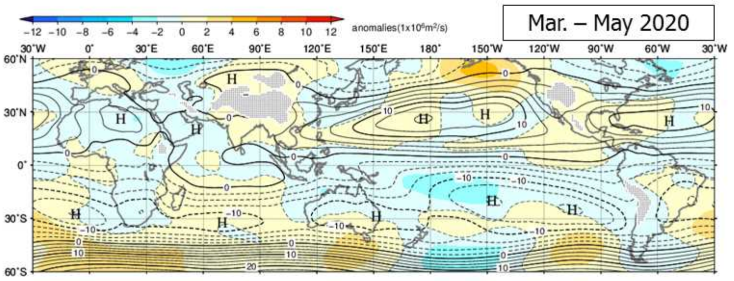

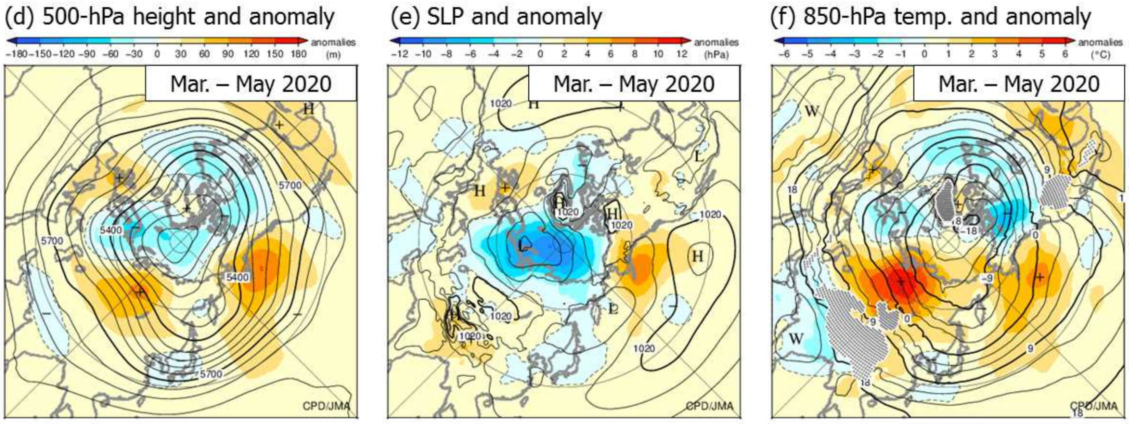
(d) 500-hPa height and anomaly
(e) SLP and anomaly
(f) 850-hPa temp. and anomaly

Figure 1.3-2 As per Figure 1.3-1, but for March – May 2020
In (f), contour interval is 3 degree C.

(a) SST anomaly

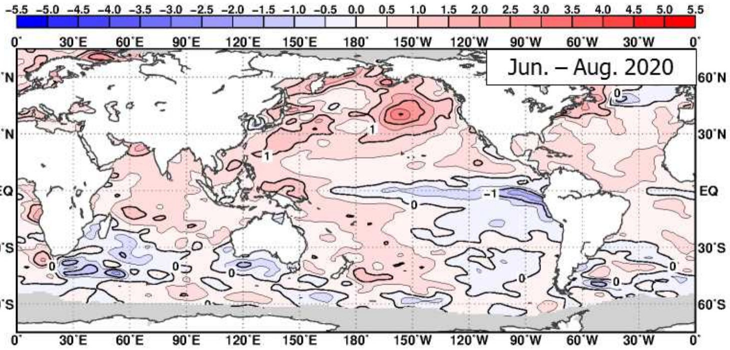

(b) OLR anomaly

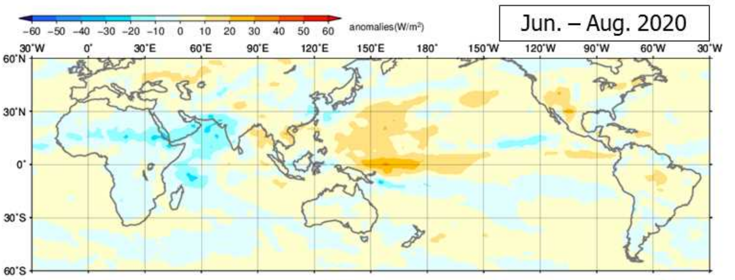

(c) 850-hPa stream function and anomaly

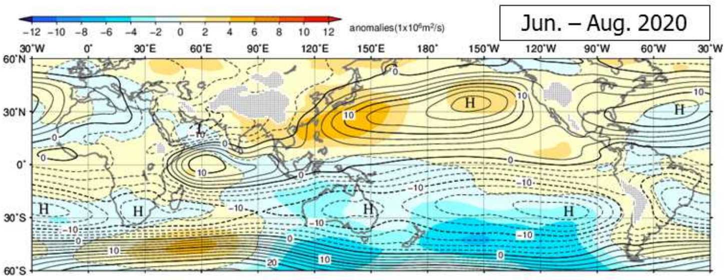

(d) 500-hPa height and anomaly (e) SLP and anomaly (f) 850-hPa temp. and anomaly

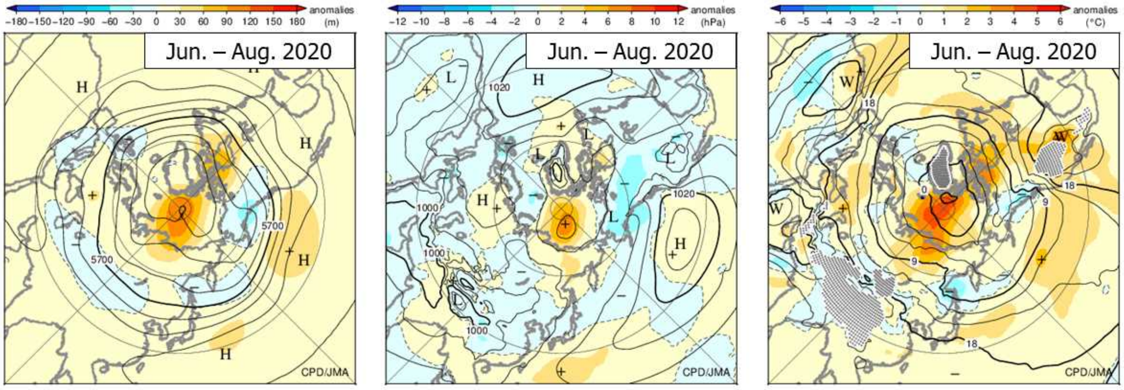

Figure 1.3-3 As per Figure 1.3-1, but for June – August 2020
In (f), contour interval is 3 degree C.

(a) SST anomaly

(b) OLR anomaly

(c) 850-hPa stream function and anomaly

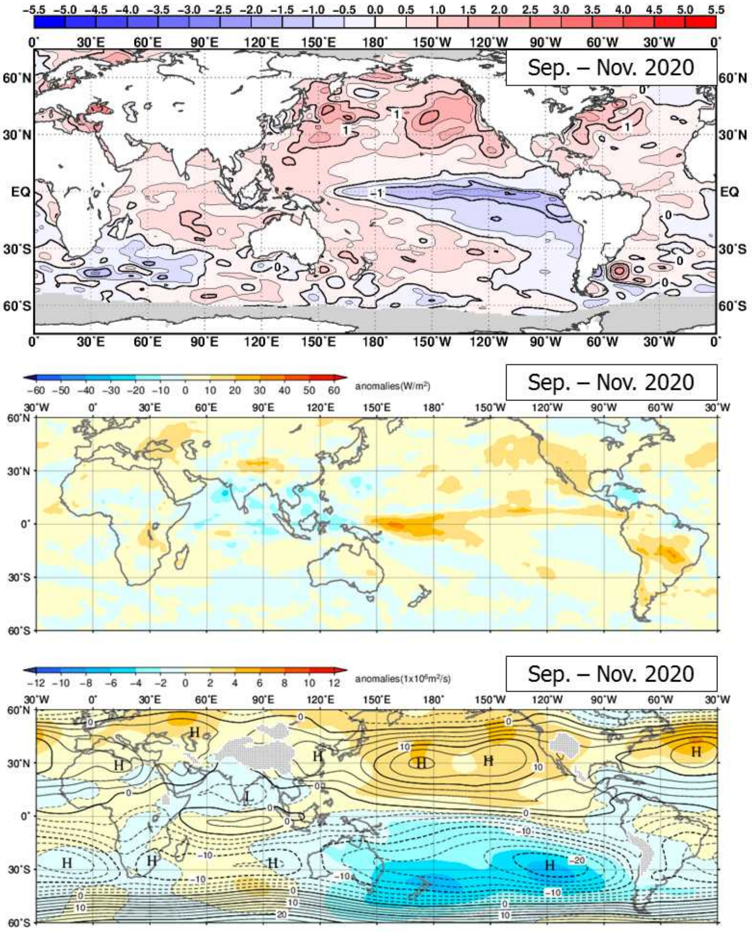

(d) 500-hPa height and anomaly

(e) SLP and anomaly

(f) 850-hPa temp. and anomaly

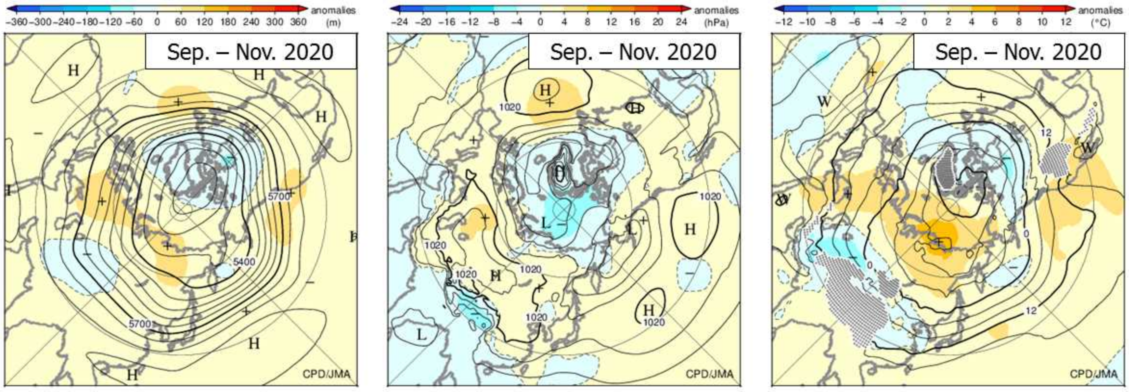

Figure 1.3-4 As per Figure 1.3-1, but for September – November 2020

1.3.2 Global average temperature in the troposphere

The global average temperature in the troposphere (Figure 1.3-5) increased from spring 2018 to early 2020 and remained higher than normal thereafter. Values in July and November 2020 were the highest on record for these months since 1958 (Figure 1.3-6).

Figure 1.3-5 Time-series representation of global average temperature anomalies calculated from thickness in the troposphere (2009 to 2020)

The thin and thick lines show monthly mean and five-month running mean values, respectively. The base period for the normal is 1981 – 2010.

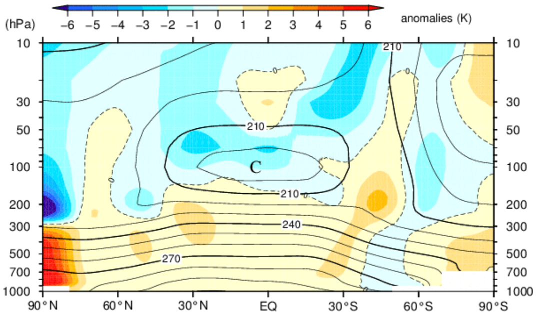

Figure 1.3-6 Latitude-height cross section of zonal mean temperature and anomaly (July 2020)

Contours show zonal mean temperature at intervals of 10 K, and shading indicates temperature anomalies. The base period for the normal is 1981 – 2010. “W” and “C” denote warm and cold conditions, respectively.

1.3.3 Asian summer monsoon

Convection during the 2020 Asian summer monsoon season (June – September) was generally suppressed except for a period of enhancement in early August as indicated by the OLR index (SAMOI (A)[10], JMA, 1997; Figure 1.3-7). In July 2020, remarkably suppressed convection in the region delayed the northward migration of the subtropical jet stream over Eurasia and resulted in an unusually persistent Meiyu-Baiu front from the Yangtze River basin to Japan. Enhanced convection in the region in early August may have been a factor in the expansion of the NPSH toward mainland Japan.

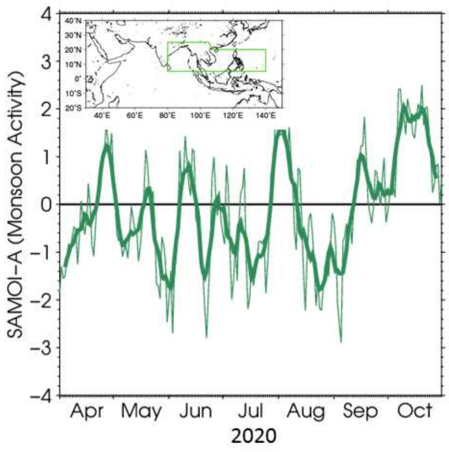

Figure 1.3-7 Time-series representation of the Asian summer monsoon OLR index (SAMOI (A)) (April – October 2020)

The thin and thick green lines indicate daily and seven-day running mean values, respectively. SAMOI (A) indicates the overall activity of the Asian summer monsoon, and positive and negative values indicate enhanced and suppressed convective activity, respectively, compared to the normal. The base period for the normal is 1981 – 2010. Original OLR data provided by NOAA.

---

[10] SAMOI (A) is defined as reversed-sign area-averaged OLR anomalies normalized by its standard deviation. The area for average is enclosed by green line in the map of Figure 1.3-7.s

1.3.4 Tropical cyclones over the western North Pacific and the South China Sea

In 2020, 23 tropical cyclones (TCs) with maximum wind speeds of ≥ 34 kt formed over the western North Pacific and the South China Sea (Figure 1.3-8, Table 1.3-1), which was below the normal of 25.6 (1981 – 2010 average). A total of 2 TCs formed from January to July, which was below the normal of 7.7. TC Sinlaku was the second-latest formation of the third named TC of the year (00 UTC, 1 August 2020) since records began in 1951. This is attributable to enhanced convective activity in the Indian Ocean due to warmer-than-normal SSTs and relative suppression of those in the South China Sea and the sea east of Philippines, where tropical cyclones form (see Section 1.3.1). A total of 21 TCs formed from August to December, which was above the normal of 17.8.

A total of 7 TCs came within 300 km of the Japanese archipelago, which was below the normal of 11.4. No TCs made landfall on Japan for the first time since 2008 and only the fifth time since records began in 1951.

Among the 7 TCs approaching Japan, TC Haishen passed very near the Kyushu region, bringing unprecedented winds to the Nansei Islands, the Kyushu region and elsewhere, along with heavy rain in and around Miyazaki Prefecture, causing significant damage and widespread power blackouts. TC Chan-hom passed near the Okinawa region, the main islands of Japan and the Izu Islands, bringing extremely heavy rain to the southern Izu Islands and causing landslides in the Tokai region and the Izu Islands.

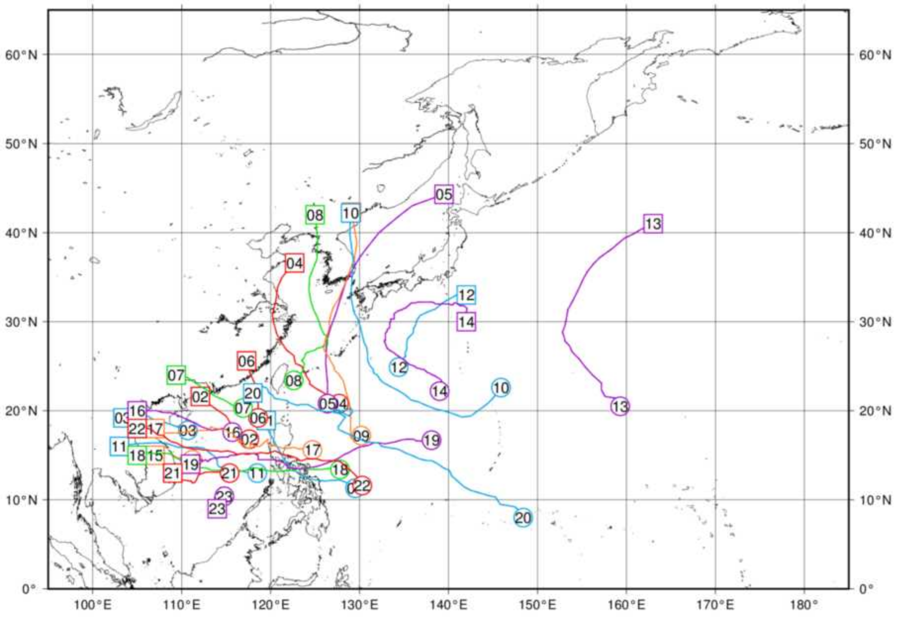

Figure 1.3-8 Tracks of TCs with maximum wind speeds of ≥ 34 kt in 2020

Numbered circles indicate positions of the TC formed (maximum wind speeds of ≥ 34 kt), and numbered squares indicate positions of the TC dissipated (maximum wind speeds lower than 34 kt). Source: RSMC Tokyo-Typhoon Center data

Table 1.3-1 TCs with maximum wind speeds of ≥ 34 kt in 2020 (Source: RSMC Tokyo-Typhoon Center data)

Number ID	Tropical Cyclone	Duration (UTC)	Maximum Wind[1)] (kt)	Number ID	Tropical Cyclone	Duration (UTC)	Maximum Wind[1)] (kt)
2001	VONGFONG	1200, 12 May - 1200, 16 May	85	2013	KUJIRA	1800, 26 Sep - 0600, 30 Sep	60
2002	NURI	1200, 12 Jun - 0000, 14 Jun	40	2014	CHAN-HOM	0000, 05 Oct - 1800, 11 Oct	70
2003	SINLAKU	0000, 01 Aug - 1800, 02 Aug	40	2015	LINFA	1800, 10 Oct - 1200, 11 Oct	45
2004	HAGUPIT	0600, 01 Aug - 1200 05 Aug	70	2016	NANGKA	0600, 12 Oct - 1200, 14 Oct	45
2005	JANGMI	1800, 08 Aug - 0600, 11 Aug	45	2017	SAUDEL	0000, 20 Oct - 1200, 25 Oct	65
2006	MEKKHALA	0000, 10 Aug - 0600, 11 Aug	50	2018	MOLAVE	0600, 24 Oct - 1800, 28 Oct	90
2007	HIGOS	0000, 18 Aug - 1800, 19 Aug	55	2019	GONI	1800, 28 Oct - 1200, 05 Nov	120
2008	BAVI	0000, 22 Aug - 0600, 27 Aug	85	2020	ATSANI	1800, 02 Nov - 0600, 07 Nov	50
2009	MAYSAK	0600, 28 Aug - 0600, 03 Sep	95	2021	ETAU	1800, 08 Nov - 1200, 10 Nov	45
2010	HAISHEN	1200, 31 Aug - 1800, 07 Sep	105	2022	VAMCO	1200, 09 Nov - 1200, 15 Nov	85
2011	NOUL	1800, 15 Sep - 1800, 18 Sep	45	2023	KROVANH	0000, 20 Dec - 0600, 22 Dec	35
2012	DOLPHIN	0000, 21 Sep - 0600, 24 Sep	60				

1) Estimated maximum 10-minute mean wind speed

Chapter 2 Climate Change

2.1 Changes in temperature[12]

- ○ The annual anomaly of the global average surface temperature in 2020 was +0.45ºC, tied with 2016 as the highest since 1891. On a longer time scale, it is virtually certain that the annual global average surface temperature has risen at rates of 0.75ºC per century.
- ○ The annual anomaly of the average temperature over Japan was +0.95ºC, the highest since 1898. On a longer time scale, it is virtually certain that the annual average temperature over Japan has risen at rates of 1.26ºC per century.
- ○ It is virtually certain that the annual number of days with maximum temperatures of 35 ºC or higher ($T_{max} \geq 35$ºC) and that with minimum temperatures of 25ºC or higher ($T_{min} \geq$ 25ºC) have increased, while the annual number of days with minimum temperatures below 0ºC ($T_{min} <$ 0ºC) has decreased.

2.1.1 Global surface temperature

The annual anomaly of the global average surface temperature in 2020 (i.e., the combined average of the near-surface air temperature over land and the SST) was +0.45ºC above the 1981 – 2010 average. This was tied with 2016 as the highest since 1891. The years from 2014 to 2020 were the top-seven warmest on record in terms of global temperature. The global average temperature fluctuates on different time scales ranging from years to decades. On a longer time scale, it is virtually certain that the global average surface temperature has risen at a rate of 0.75ºC per century[13] (statistically significant at a confidence level of 99%[14]).

The surface temperature anomalies over the Northern Hemisphere and the Southern Hemisphere were +0.67ºC (the highest) and +0.23ºC (the 5th highest) above the 1981 – 2010 average, respectively (Figure 2.1-1). It is virtually certain that average surface temperatures over the Northern Hemisphere and the Southern Hemisphere have risen at rates of 0.82ºC and 0.70ºC per century, respectively (both statistically significant at a confidence level of 99%).

Linear temperature trends for 5° × 5° latitude/longitude grid boxes indicate that most areas of the world, especially in the high latitudes of the Northern Hemisphere, have experienced long-term warming (Figure 2.1-2). These long-term trends in annual average temperatures can be largely attributed to global warming caused by increased concentrations of greenhouse gases such as CO_2. On a shorter time scale, temperatures fluctuate due to the influence of natural climate dynamics over different time scales ranging from years to decades.

---

[12] Monthly, seasonal and annual estimates of mean temperatures averaged over the globe and Japan are published on JMA's website.
https://www.data.jma.go.jp/cpdinfo/temp/index.html (Japanese)
https://ds.data.jma.go.jp/tcc/tcc/products/gwp/gwp.html (English)

[13] According to IPCC AR5, the global average surface temperature has risen about 0.85°C (The 90% uncertainty interval is 0.65 to 1.06°C) over the period 1880 to 2012. The values given in IPCC AR5 and those in this report are considered to show no remarkable difference that have risen on a longer time scale and are higher since the mid-1990s, although they do not correspond exactly because of differences in dataset calculation methods and the statistical period examined.

[14] For evaluation and clarification of the significance statistics used here, see "Explanatory note on detection of statistical significance in long-term trends" at the end of the report.

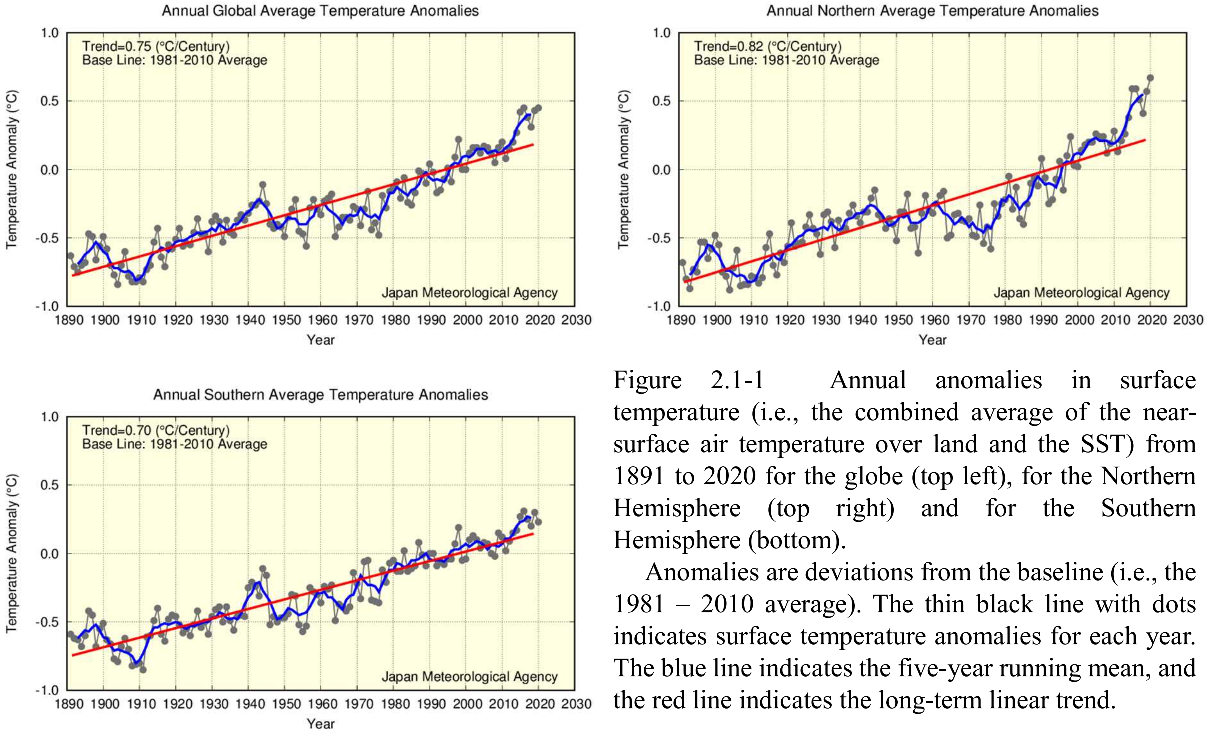

Figure 2.1-1 Annual anomalies in surface temperature (i.e., the combined average of the near-surface air temperature over land and the SST) from 1891 to 2020 for the globe (top left), for the Northern Hemisphere (top right) and for the Southern Hemisphere (bottom).

Anomalies are deviations from the baseline (i.e., the 1981 – 2010 average). The thin black line with dots indicates surface temperature anomalies for each year. The blue line indicates the five-year running mean, and the red line indicates the long-term linear trend.

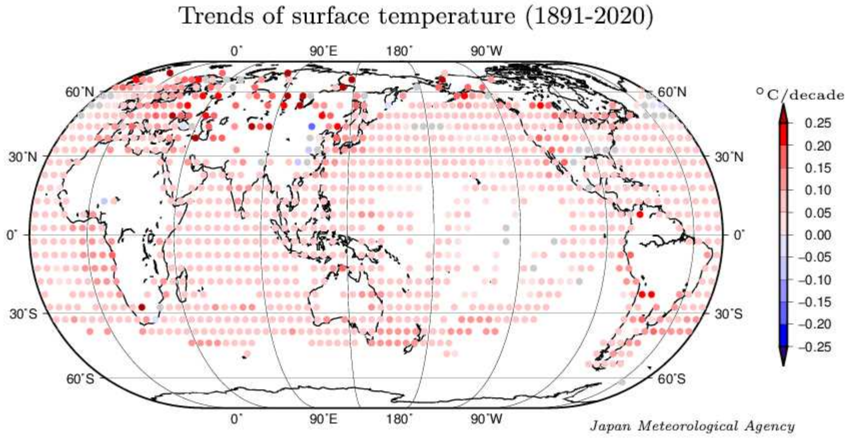

Figure 2.1-2 Linear temperature trends for 5° × 5° latitude/longitude grid boxes for the period of 1891 to 2020
The grid boxes with gray circles have no statistically significant trend (not statistically significant at a confidence level of 90%). Blank areas indicate those with insufficient data to analyze long-term trends.

2.1.2 Surface temperature over Japan

Long-term changes in the surface temperature over Japan are analyzed using observational records dating back to 1898. Table 2.1-1 lists the meteorological stations whose data are used to derive annual mean surface temperatures.

Table 2.1-1 Observation stations whose data are used to calculate surface temperature anomalies over Japan
Miyazaki and Iida were relocated in May 2000 and May 2002, respectively, and their temperatures have been adjusted to eliminate the influence of the relocation.

Element	Observation stations
Temperature (15 stations)	Abashiri, Nemuro, Suttsu, Yamagata, Ishinomaki, Fushiki, Iida, Choshi, Sakai, Hamada, Hikone, Tadotsu, Miyazaki, Naze, Ishigakijima

The mean surface temperature in Japan for 2020 is estimated to have been 0.95ºC above the 1981 – 2010 average, which is the highest since 1898 (Figure 2.1-3). The surface temperature fluctuates on different time scales ranging from years to decades. On a longer time scale, it is virtually certain that the annual mean surface temperature over Japan has risen at a rate of 1.26ºC per century (statistically significant at a confidence level of 99%). Similarly, it is virtually certain that the seasonal mean temperatures for winter, spring, summer and autumn have risen at rates of about 1.19, 1.49, 1.14 and 1.26ºC per century, respectively (all statistically significant at a confidence level of 99%).

It is noticeable from Figure 2.1-3 that the annual mean temperature remained relatively low before the 1940s, started to rise and reached a local peak around 1960, entered a cooler era through to the mid-1980s and then began to show a rapid warming trend in the late 1980s. The warmest years on record have all been observed since the 1990s.

The high temperatures seen in recent years have been influenced by fluctuations over different time scales ranging from years to decades, as well as by global warming resulting from increased concentrations of greenhouse gases such as CO_2.

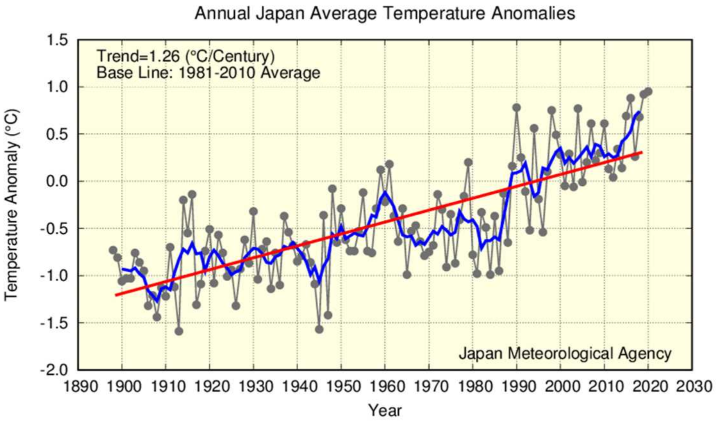

Figure 2.1-3 Annual surface temperature anomalies from 1898 to 2020 in Japan.
Anomalies are deviations from the baseline (i.e., the 1981 – 2010 average). The thin black line indicates the surface temperature anomaly for each year. The blue line indicates the five-year running mean, and the red line indicates the long-term linear trend.

2.1.3 Long-term trends of extreme temperature events[15] in Japan

This section describes long-term trends of extremely high/low-temperature events in Japan, as derived from analysis of temperature records from the 15 observation stations. Though monthly mean temperatures of the stations in Miyazaki and Iida have been adjusted to eliminate the influence of their relocation, records from these two stations are not used for analysis of daily temperatures due to the difficulty of adjustment in regard to the relocation.

(1) Long-term trends of monthly extreme temperatures

It is virtually certain that the frequency of extremely high monthly temperatures has increased during the period from 1901 to 2020, while that of extremely low monthly temperatures has decreased (both statistically significant at the confidence level of 99%) (Figure 2.1-4). The frequency of extremely high monthly temperatures has largely increased since about 1990.

---

[15] Here, judgment of extremely high/low temperatures is based on the fourth-highest/lowest monthly values on records over the 120-year period from 1901 to 2020. The frequency of occurrence of the highest/lowest to the fourth-highest/lowest values over this period is once approximately every 30 years, which is close to JMA's definition of extreme climate events as those occurring once every 30 years or longer (See the Glossary for terms relating to Extreme climate event).

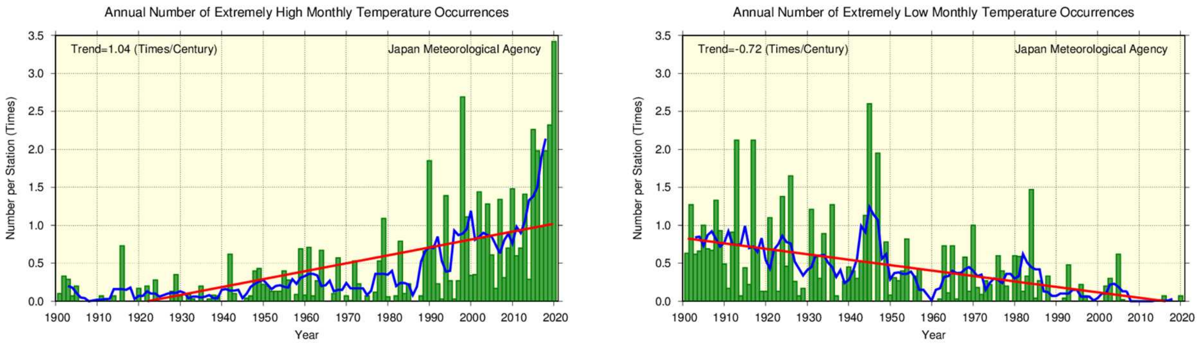

Figure 2.1-4 Annual number of extremely high/low monthly mean temperature occurrences from 1901 to 2020
The graphs show the annual number of occurrences of the highest/lowest first-to-forth values for each month during the period from 1901 to 2020. The green bars indicate annual occurrences of extremely high/low monthly mean temperatures divided by the total number of monthly observation data sets available for the year (i.e., the average occurrence per station). The blue line indicates the five-year running mean, and the straight red line indicates the long-term linear trend.

(2) Annual number of days with maximum temperatures of ≥ 30°C and ≥ 35°C

The annual number of days with maximum temperatures (T_{max}) of ≥ 30°C and T_{max} ≥ 35°C is virtually certain to have increased during the period from 1910 to 2020 (both statistically significant at a confidence level of 99%) (Figure 2.1-5). Especially, the annual number of days with T_{max} ≥ 35°C has largely increased since about mid-1990s.

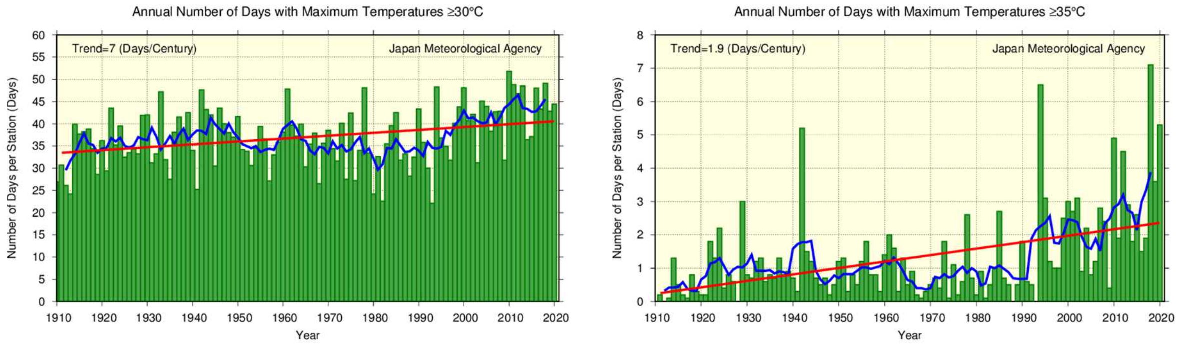

Figure 2.1-5 Annual number of days with maximum temperatures of ≥ 30°C and ≥ 35°C from 1910 to 2020
The green bars indicate the annual number of days per station for each year. The blue line indicates the five-year running mean, and the straight red line indicates the long-term linear trend.

(3) Annual number of days with minimum temperatures of < 0°C and ≥ 25°C

It is virtually certain that the annual number of days with minimum temperatures (T_{min}) of < 0°C has decreased, while the annual number of days with T_{min} ≥ 25°C has increased during the period from 1910 to 2020 (both statistically significant at a confidence level of 99%) (Figure 2.1-6).

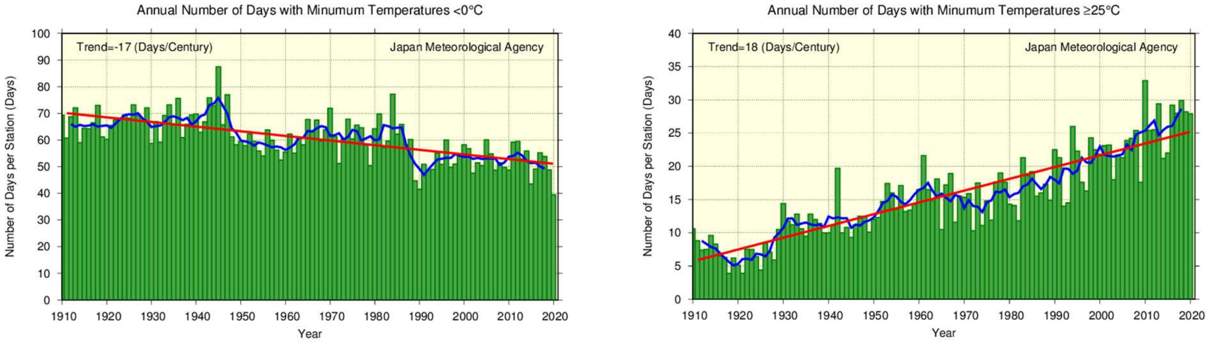

Figure 2.1-6 Annual number of days with minimum temperatures of <0°C and ≥ 25°C from 1910 to 2020
As per Figure 2.1-5.

2.1.4 Urban heat island effect at urban stations in Japan

The long-term trends of annual average temperatures are more pronounced for urban observation stations whose data are homogeneous over a long period (Sapporo, Sendai, Tokyo, Yokohama, Niigata, Nagoya, Kyoto, Osaka, Hiroshima, Fukuoka, Kagoshima) than for the average of the 15 rural observation stations (Table 2.1-2 and Figure 2.1-7). Although values varied by location, annual mean temperatures at urban stations (by way of example) were around 0.5 – 1.8ºC higher than the 15 station averages.

Table 2.1-2 Long-term trends of annual and seasonal average temperatures at urban stations in Japan
These figures are based on data from 1927 to 2020. The trend of the 15 rural station averages (Table 2.1-1) is also listed. Values shown in italics are not statistically significant at a confidence level of 90%. For stations with asterisks (5 urban stations, and Iida and Miyazaki among the 15 rural stations), trends are calculated after adjustment to eliminate the influence of relocation.

Station	Long-term temperature trend (°C/century)														
	Average					Daily maximum					Daily minimum				
	Ann	Win	Spr	Sum	Aut	Ann	Win	Spr	Sum	Aut	Ann	Win	Spr	Sum	Aut
Sapporo	2.6	3.3	3.0	1.8	2.5	1.0	1.5	1.7	*0.6*	*0.5*	4.4	5.6	4.7	3.3	4.2
Sendai	2.5	3.0	2.9	1.5	2.5	1.4	1.7	1.8	1.0	1.0	3.2	3.7	3.8	2.0	3.3
Tokyo*	3.3	4.3	3.3	2.1	3.4	1.9	2.1	2.2	1.4	1.8	4.4	5.9	4.6	3.0	4.4
Yokohama	2.8	3.5	3.1	1.8	2.8	2.5	2.8	3.0	1.9	2.4	3.5	4.6	3.7	2.2	3.5
Niigata*	2.1	2.3	2.6	1.4	1.9	2.0	2.8	2.8	0.9	1.7	2.2	2.4	2.7	1.9	1.8
Nagoya	2.9	3.0	3.1	2.3	3.1	1.5	1.6	1.8	1.1	1.4	3.9	3.9	4.4	3.2	4.3
Kyoto	2.7	2.7	3.0	2.3	2.8	1.2	0.9	1.7	1.1	0.9	3.8	3.8	4.1	3.3	4.0
Osaka*	2.6	2.7	2.7	2.0	2.9	2.2	2.2	2.4	1.9	2.1	3.5	3.2	3.5	3.2	4.0
Hiroshima*	2.0	1.7	2.3	1.5	2.5	1.0	0.8	1.7	1.1	0.5	3.1	2.9	3.3	2.6	3.9
Fukuoka	3.1	3.0	3.4	2.2	3.7	1.8	1.8	2.2	1.4	1.7	4.9	4.4	5.8	3.6	6.0
Kagoshima*	2.5	2.6	2.8	2.0	2.9	1.3	1.3	1.7	1.1	1.4	3.9	3.6	4.4	3.2	4.6
15 station averages*	1.5	1.7	1.9	1.1	1.5	1.2	1.3	1.7	0.8	0.9	1.9	1.9	2.1	1.6	1.9

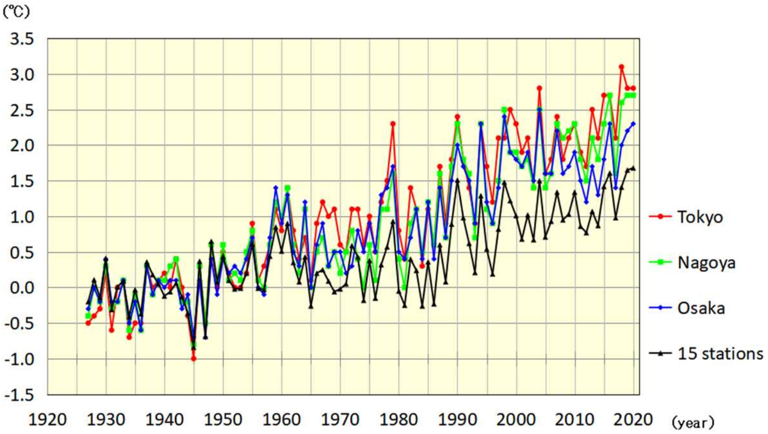

Figure 2.1-7 Annual temperature anomalies at Tokyo, Nagoya and Osaka and values averaged over 15 rural stations in Japan from 1927 to 2020

Anomalies are deviations from the baseline (i.e., the 1927 – 1956 average). Values averaged between 1927 and 1956 for respective stations all equal zero.

As it can be assumed that the long-term trends averaged over the 15 rural stations reflect large-scale climate change, the differences in the long-term trends of urban stations from the average of the 15 stations largely represent the influence of urbanization.

Detailed observation reveals that the long-term trends are more significant in winter, spring and autumn than in summer and more pronounced for minimum temperatures than for maximum temperatures at every urban observation station.

Records from urban stations whose data are not affected by relocation are used to determine long-term trends for the annual number of days with minimum temperatures of < 0°C and ≥ 25°C and maximum temperatures of ≥ 30°C and ≥ 35°C. The number of days with $T_{min} < 0°C$ is very likely to have decreased with statistical significance at all urban stations, and the number with $T_{min} \geq 25°C$, $T_{max} \geq 30°C$ and $T_{max} \geq 35°C$ is very likely to have increased with statistical significance at most stations except Sapporo (Table 2.1-3).

Table 2.1-3 Long-term trends for the annual number of days with minimum temperatures of < 0°C and ≥ 25°C and maximum temperatures of ≥ 30°C and ≥ 35°C.

These figures are based on data from 1927 to 2020. The trend of the 13 rural station averages (Table 2.1-1, excluding Iida and Miyazaki) is also listed. Values shown in italics are not statistically significant at a confidence level of 90%.

Station	Annual number of days			
	Trend (days/decade)			
	$T_{min} < 0°C$	$T_{min} \geq 25°C$	$T_{max} \geq 30°C$	$T_{max} \geq 35°C$
Sapporo	−4.4	*0.0*	*0.2*	*0.0*
Sendai	−5.9	0.4	1.0	0.1
Yokohama	−5.9	3.1	2.2	0.3
Nagoya	−6.8	3.8	1.3	1.1
Kyoto	−7.2	3.7	1.3	1.4
Fukuoka	−4.9	4.7	1.1	1.1
13 station averages	−2.1	1.8	0.6	0.2

2.2 Changes in precipitation[16]

- ○ The annual anomaly of global precipitation (for land areas only) in 2020 was +39 mm.
- ○ The annual anomaly of precipitation in 2020 was +210.2 mm in Japan. Annual precipitation over Japan shows no discernible long-term trend.
- ○ The annual number of days with daily and hourly extreme precipitation has increased in Japan, while that with wet days has decreased.
- ○ Snow depth on the Sea of Japan side has decreased.

2.2.1 Global precipitation over land

Annual precipitation (for land areas only) in 2020 was +39 mm above the 1981 – 2010 average (Figure 2.2-1), and the figure has fluctuated periodically since 1901. In the Northern Hemisphere, records show large amounts of rainfall around 1930, in the 1950s and after the mid-2000s. Long-term trends are not analyzed because the necessary precipitation data for sea areas are not available.

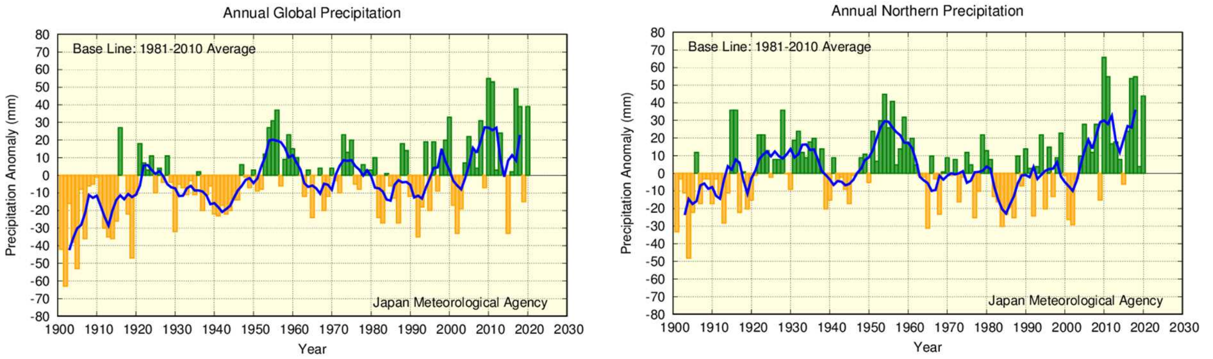

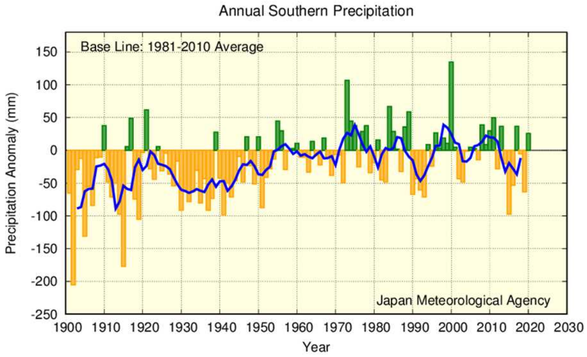

Figure 2.2-1 Annual anomalies in precipitation (over land areas only) from 1901 to 2020 for the globe (top left), for the Northern Hemisphere (top right) and for the Southern Hemisphere (bottom). Anomalies are deviations from the baseline (i.e., the 1981 – 2010 average).

The bars indicate the precipitation anomaly for each year, and the blue line indicates the five-year running mean.

2.2.2 Precipitation over Japan

This section describes long-term trends in precipitation over Japan as derived from analysis of precipitation records from 51 observation stations (Table 2.2-1).

Annual precipitation in 2020 was +210.2 mm above the 1981 – 2010 average. Japan experienced relatively large amounts of rainfall until the mid-1920s and around the 1950s. The annual figure exhibits greater variability for the period from the 1970s to the 2000s (Figure 2.2-2).

---

[16] Data on annual precipitation around the world and in Japan are published on JMA's website. https://www.data.jma.go.jp/cpdinfo/temp/index.html (Japanese)

Table 2.2-1 List of 51 observation stations whose data are used to calculate precipitation anomalies and long-term trends in Japan

Element	Observation stations
Precipitation (51 stations)	Asahikawa, Abashiri, Sapporo, Obihiro, Nemuro, Suttsu, Akita, Miyako, Yamagata, Ishinomaki, Fukushima, Fushiki, Nagano, Utsunomiya, Fukui, Takayama, Matsumoto, Maebashi, Kumagaya, Mito, Tsuruga, Gifu, Nagoya, Iida, Kofu, Tsu, Hamamatsu, Tokyo, Yokohama, Sakai, Hamada, Kyoto, Hikone, Shimonoseki, Kure, Kobe, Osaka, Wakayama, Fukuoka, Oita, Nagasaki, Kumamoto, Kagoshima, Miyazaki, Matsuyama, Tadotsu, Kochi, Tokushima, Naze, Ishigakijima, Naha

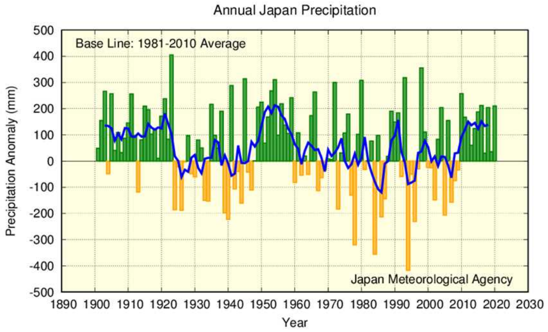

Figure 2.2-2 Annual anomalies in precipitation from 1898 to 2020 in Japan. Anomalies are deviations from the baseline (i.e., the 1981 – 2010 average).

The bars indicate the precipitation anomaly for each year, and the blue line indicates the five-year running mean.

2.2.3 *Long-term trends of extreme precipitation events in Japan*

This section describes long-term trends in frequencies of extremely wet/dry months and heavy daily precipitation events in Japan based on analysis of precipitation data from 51 observation stations.

(1) Extremely wet/dry months[17]

It is virtually certain that the frequency of extremely dry months increased during the period from 1901 to 2020 (statistically significant at a confidence level of 99%) (Figure 2.2-3 left). There has been no discernible trend in the frequency of extremely wet months (Figure 2.2-3 right).

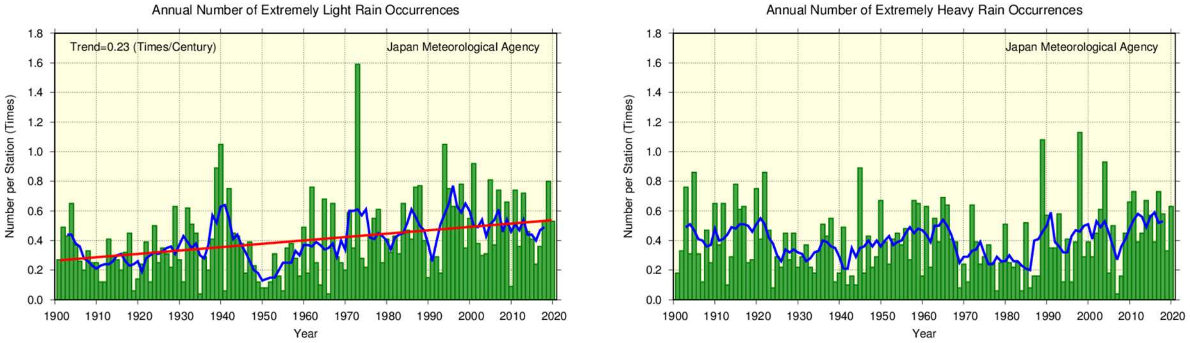

Figure 2.2-3 Annual number of extremely wet/dry months from 1901 to 2020

The graphs show the annual number of occurrences of the first-to-forth heaviest/lightest precipitation values for each month during the period from 1901 to 2020. The green bars indicate annual occurrences of extremely heavy/light monthly precipitation divided by the total number of monthly observation data sets available for the year (i.e., the average occurrence per station). The blue line indicates the five-year running mean, and the straight red line indicates the long-term liner trend.

(2) Annual number of days with precipitation of ≥ 100 mm, ≥ 200 mm and ≥ 1.0 mm

---

[17] Here, judgment of extremely heavy/light precipitation is based on the fourth–highest/lowest monthly values on record over the 120-year period from 1901 to 2020. The frequency of occurrence of the highest/lowest to the fourth–highest/lowest values over this period is once approximately every 30 years, which is close to JMA's definition of extreme climate events as those occurring once every 30 years or longer (See the Glossary for terms relating to Extreme climate event).

The annual number of days with precipitation of ≥ 100 mm and ≥ 200 mm are virtually certain to have increased during the period from 1901 to 2020 (both statistically significant at a confidence level of 99%) (Figure 2.2-4) . The annual number of days with precipitation of ≥ 1.0 mm (Figure 2.2-5) is virtually certain to have decreased over the same period (statistically significant at a confidence level of 99%). These results suggest decrease in the annual number of wet days including light precipitation and in contrast, an increase in extremely wet days.

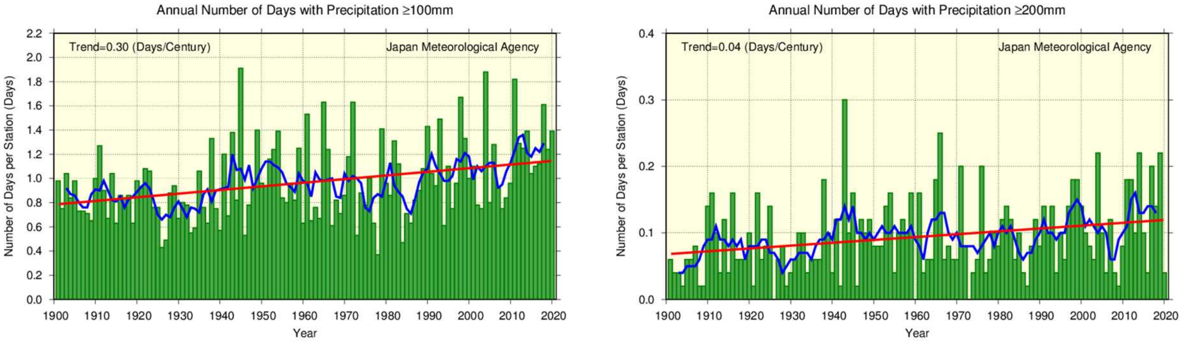

Figure 2.2-4 Annual number of days with precipitation ≥ 100 mm and ≥ 200 mm from 1901 to 2020
The green bars indicate the annual number of days per station for each year. The blue line indicates the five-year running mean, and the straight red line indicates the long-term liner trend.

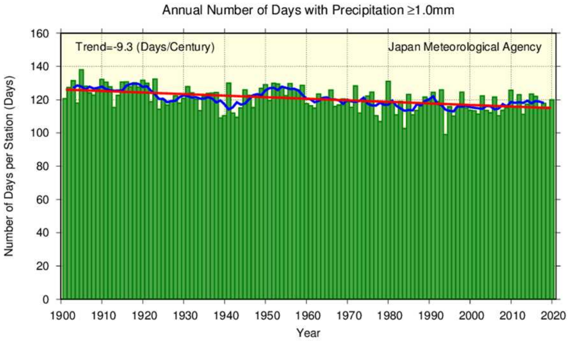

Figure 2.2-5 Annual number of days with precipitation of ≥ 1.0 mm from 1901 to 2020
As per figure 2.2-4.

2.2.4 Long-term trends of heavy rainfall analyzed using AMeDAS data

JMA operationally observes precipitation at about 1,300 unmanned regional meteorological observation stations all over Japan (collectively known as the Automated Meteorological Data Acquisition System, or AMeDAS). Observation was started in the latter part of the 1970s at many points, and observation data covering the approximately 45-year period through to 2020 are available[18]. Although the period covered by AMeDAS observation records is shorter than that of Local Meteorological Observatories or Weather Stations (which have observation records for the past 100 years or so), there are around eight times as many AMeDAS stations as Local Meteorological Observatories and Weather Stations combined. Hence, AMeDAS is better equipped to capture heavy precipitation events that take place on a limited spatial scale.

It is virtually certain that the annual numbers of events with precipitation of ≥ 50 mm and ≥ 80 mm per hour have increased (both statistically significant at a confidence level of 99%)

---

[18] The number of AMeDAS station was about 800 in 1976, and had gradually increased to about 1,300 in 2020. To account for these numerical differences, the annual number of precipitation events needs to be converted to a per-1,300-station basis. Data from wireless robot precipitation observation stations previously deployed in mountainous areas are also excluded.

(Figure 2.2-6). For the annual number of days with precipitation of ≥ 50 mm per hour, the number averaged for the last 10 years of the records (2010 – 2020) is about 334 on a per-1,300-station basis, which is about 1.5 times as many as that averaged for the first 10 years (1976 – 1985) of about 226.

The annual number of days with precipitation of ≥ 200 mm and ≥ 400 mm is extremely likely to have increased (both statistically significant at a confidence level of 95%) (Figure 2.2-7).

As the frequency of extreme precipitation events is low and the period covered by observation records is still relatively short, the addition of future observations to the data series is expected to increase the reliability of statistical trend detection.

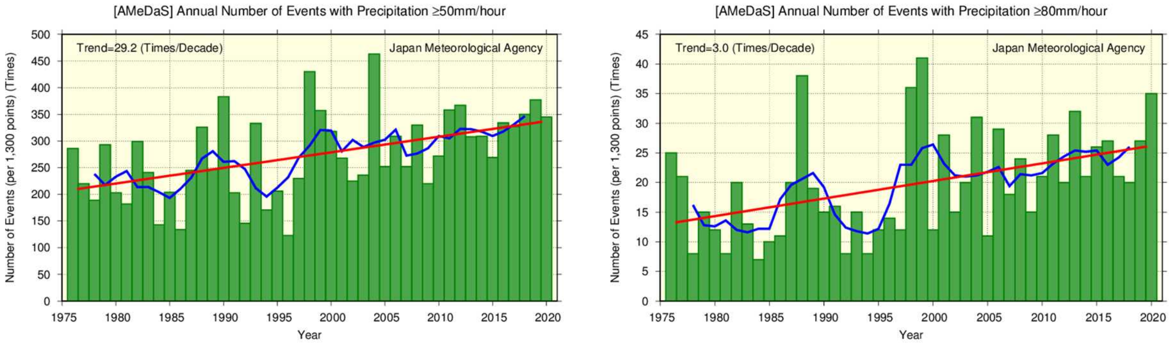

Figure 2.2-6 Annual number of events with precipitation of ≥ 50 mm and ≥ 80 mm per hour from 1976 to 2020
The green bars indicate the annual number of events per 1,300 AMeDAS stations for each year. The blue line indicates the five-year running mean, and the straight red line indicates the long-term liner trend.

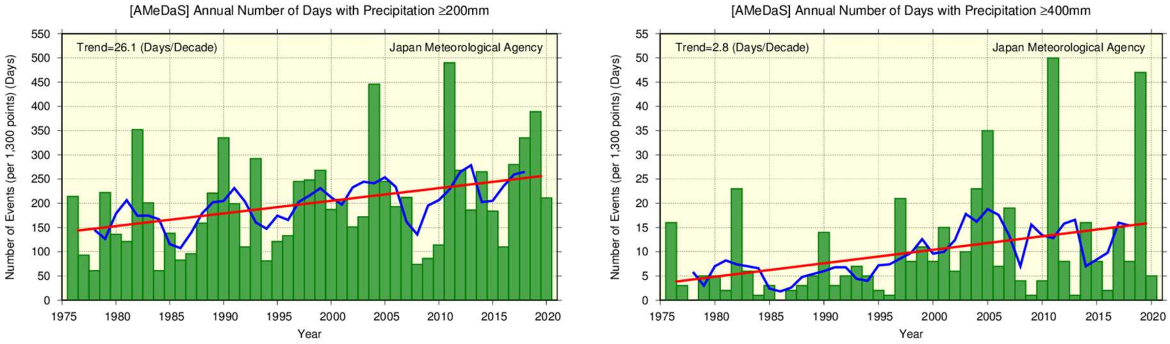

Figure 2.2-7 Annual number of days with precipitation of ≥ 200 mm and ≥ 400 mm from 1976 to 2020
The green bars indicate the annual number of days per 1,300 AMeDAS stations for each year. The blue line indicates the five-year running mean, and the straight red line indicates the long-term liner trend.

2.2.5 Snow depth in Japan

Long-term trends in the annual maximum snow depth (represented in terms of a ratio against the 1981 – 2010 average) in Japan since 1962 are analyzed using observational records from stations located on the Sea of Japan coast (Table 2.2-2).

Table 2.2-2 Observation stations whose data are used to calculate snow depth ratios in Japan

Region	Observation stations
Sea of Japan side of northern Japan	Wakkanai, Rumoi, Asahikawa, Sapporo, Iwamizawa, Suttsu, Esashi, Kutchan, Wakamatsu, Aomori, Akita, Yamagata
Sea of Japan side of eastern Japan	Wajima, Aikawa, Niigata, Toyama, Takada, Fukui, Tsuruga
Sea of Japan side of western Japan	Saigo, Matsue, Yonago, Tottori, Toyooka, Hikone, Shimonoseki, Fukuoka, Oita, Nagasaki, Kumamoto

The annual maximum snow depth ratio in 2020 was 43% relative to the 1981 – 2010 average for the Sea of Japan side of northern Japan, 13% for the same side of eastern Japan, and 24% for the same side of western Japan (Figure 2.2-8). On a longer time scale, the annual maximum snow depth ratio from 1962 onward on the Sea of Japan side of northern Japan is extremely likely to have decreased at rates of 4.1% per decade (statistically significant at a confidence level of 95%), that on the Sea of Japan side of eastern Japan is virtually certain to have decreased at rates of 12.4% per decade (statistically significant at a confidence level of 99%), and that on the Sea of Japan side of western Japan is extremely likely to have decreased at rates of about 14.3% per decade (statistically significant at a confidence level of 95%). The annual maximum snow depth reached a local peak in the early 1980s followed by a sharp decline until around the early 1990s. The decline was particularly striking on the Sea of Japan side of eastern and western Japan.

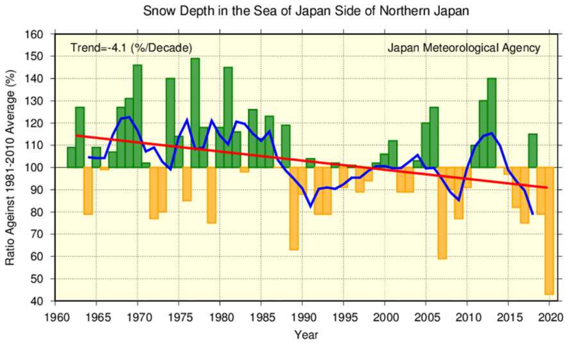

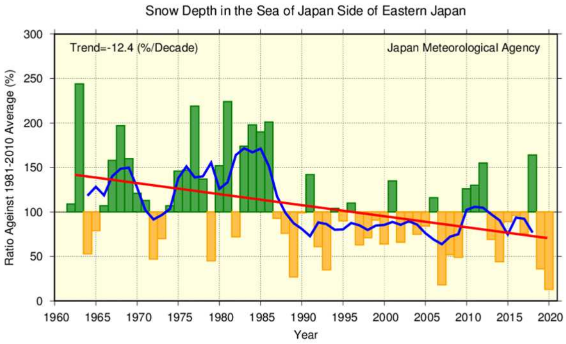

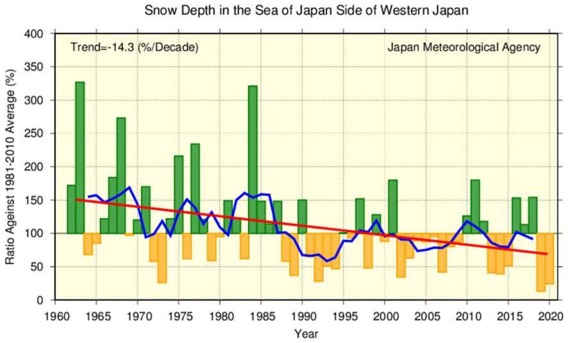

Figure 2.2-8 Annual maximum snow depth ratio from 1962 to 2020 on the Sea of Japan side for northern Japan (top left), eastern Japan (top right) and western Japan (bottom). Annual averages are presented as ratios against the baseline (i.e., the 1981 – 2010 average).

The bars indicate the snow depth ratio for each year. The blue line indicates the five-year running mean, and the red line indicates the long-term linear trend.

2.3 Changes in the phenology of cherry blossoms and acer leaves in Japan

○ It is virtually certain that cherry blossoms have been flowering earlier.
○ It is virtually certain that acer leaves have been changing color later.

JMA implements phenological observation to monitor seasonal progress, geographical variations and long-term changes in relation to the climate. Observation covers the first/full flowering and foliage color changes in several types of flora.

As part of its phenological monitoring, JMA observes cherry blossoms at 58 stations and acer leaves at 51 stations. Figure 2.3-1 shows interannual changes in the first reported dates of cherry blossom flowering and acer leaf color change between 1953 and 2020. The former exhibits a long-term advancing trend at a rate of 1.0 days per decade, while the latter shows a delaying trend at a rate of 2.8 days per decade (99% level of confidence for both cases). Table 2.3-1 compares climatological normals (based on 30-year averages) of the first reported date of cherry blossom flowering between 1961 – 1990 and 1981 – 2010 at stations in major Japanese cities. These phenomena are closely related to the surface mean temperature in the period before the event, and long-term warming is considered to be a major factor behind the trends observed.

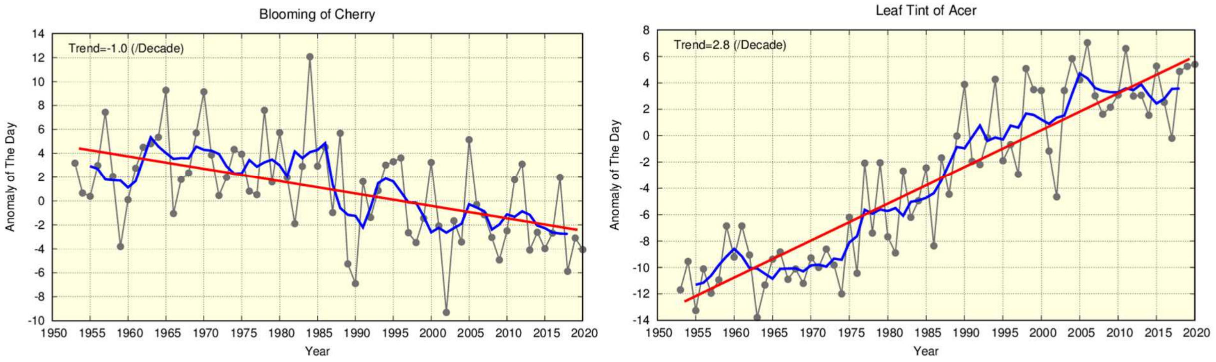

Figure 2.3-1 First reported dates of cherry blossom flowering (left) and acer leaf color change (right)
The black lines show annual anomalies of the first reported date averaged over all observation stations nationwide based on the normals for 1981 – 2010, and the blue lines indicate five-year running means. The red lines show the linear trend (cherry blossoms: −1.0 days per decade; acer leaves: +2.8 days per decade).

Table 2.3-1 Comparison of first reported dates of cherry blossom flowering
Differences in climatological normals for the first reported date of cherry blossom flowering between 1981 – 2010 and 1961 – 1990 at stations in major Japanese cities

Station	1961-1990 average	1981-2010 average	Difference (days)		1961-1990 average	1981-2010 average	Difference (days)
Kushiro	May 19	May 17	-2	Osaka	Apr 1	Mar 28	-4
Sapporo	May 5	May 3	-2	Hiroshima	Mar 31	Mar 27	-4
Aomori	Apr 27	Apr 24	-3	Takamatsu	Mar 31	Mar 28	-3
Sendai	Apr 14	Apr 11	-3	Fukuoka	Mar 28	Mar 23	-5
Niigata	Apr 13	Apr 9	-4	Kagoshima	Mar 27	Mar 26	-1
Tokyo	Mar 29	Mar 26	-3	Naha	Jan 16	Jan 18	+2
Nagoya	Mar 30	Mar 26	-4	Ishigakijima	Jan 15	Jan 16	+1

2.4 Tropical cyclones over the western North Pacific and the South China Sea

- ○ A total of 23 tropical cyclones (TCs) with maximum wind speeds of 34 kt[19] or higher formed over the western North Pacific and the South China Sea in 2020, which was below normal.
- ○ The numbers of formations show no significant long-term trend.

In 2020, 23 tropical cyclones (TCs) with maximum wind speeds of ≥ 34 kt formed over the western North Pacific and the South China Sea (Figure 2.4-1), which was below the normal (i.e., the 1981 – 2010 average) of 25.6. The numbers of formations show no discernible long-term trend during the analysis period from 1951 to 2020, while they have often been below the normal from the latter half of the 1990s to the early 2010s. Numbers of TCs with maximum wind speeds of ≥ 34 kt approaching and making landfall in Japan were 7 and 0 (Figure 2.4-2), both of which were below the normal of 11.4 and 2.7, respectively. The numbers of TCs approaching Japan also show no discernible long-term trend during the same period from 1951 to 2020.

Figure 2.4-3 shows the numbers and rates of strong TCs with maximum wind speeds of ≥ 64 kt to those with maximum wind speeds of ≥ 34 kt from 1977 (the year in which the collection of complete data on maximum wind speeds near TC centers began). The numbers of strong TCs show no discernible trend during the period from 1977 to 2020.

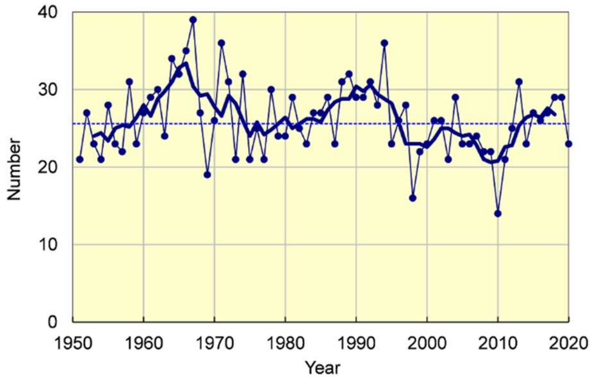

Figure 2.4-1 Time-series of the numbers of TCs with maximum wind speeds of ≥ 34 kt forming in the western North Pacific and the South China Sea from 1951 to 2020. The thin and thick lines represent annual and five-year running means, respectively.

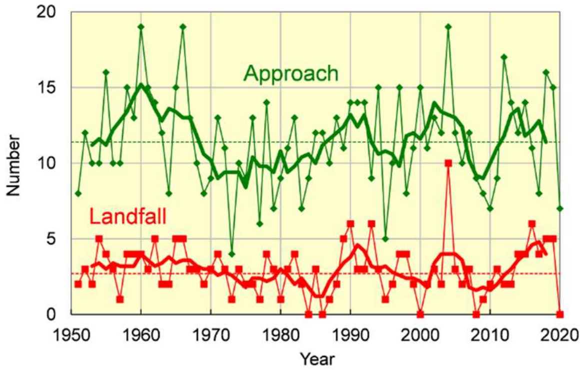

Figure 2.4-2 Time-series of the numbers of TCs with maximum wind speeds of ≥ 34 kt approaching (green) and making landfall in Japan (red) from 1951 to 2020. The thin and thick lines represent annual and five-year running means, respectively.

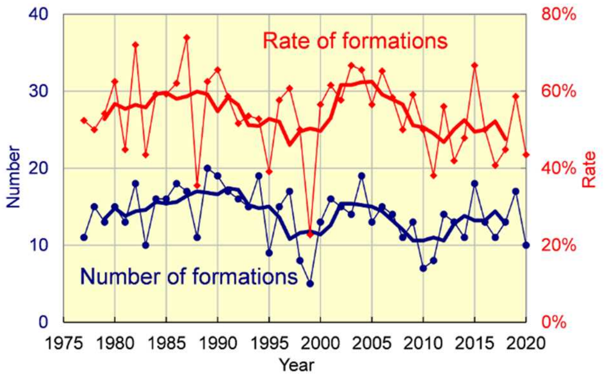

Figure 2.4-3 Time-series of the numbers of strong TCs with maximum wind speeds of ≥ 64 kt (blue) and rates of the strong TCs to the total TCs with maximum wind speeds of ≥ 34 kt (red) forming in the western North Pacific and the South China Sea from 1977 to 2020. The thin and thick lines represent annual and five-year running means, respectively.

---

[19] One knot (kt) is about 0.51 m/s

2.5 Sea surface temperature[20]

- ○ The annual mean global average sea surface temperature (SST) in 2020 was 0.31°C above the 1981 – 2010 average, and was the third highest since 1891 after 2016 (highest) and 2019.
- ○ The global average SST has risen at a rate of about +0.56°C per century.
- ○ Annual average SSTs around Japan have risen by +1.16°C per century.

2.5.1 Global sea surface temperature

The annual mean global average SST in 2020 was 0.31°C above the 1981 – 2010 average. This was the third highest since 1891 after 2016 (highest) and 2019. The years from 2014 to 2020 represent the top-seven warmest since 1891.

The linear trend from 1891 to 2019 shows an increase of +0.56°C per century (Figure 2.5-1). Although magnitudes of the long-term SST trend vary by area, it is extremely likely that SSTs have increased in many parts of the world's oceans (Figure 2.5-2). Global average SSTs and global average surface temperatures (Section 2.1) are affected by natural climate variability on inter-annual to inter-decadal time scales as well as by global warming.

On a multi-year time scale, global average SSTs showed a rising trend from the middle of the 1970s to around 2000, before remaining largely static until the early 2010s and thereafter re-assuming an upward trend (Figure 2.5-1, blue line). This is partly because rising trends overlap with decadal-to-multi-decadal variations in the climate system. It is important to estimate the contribution of these internally induced natural variations in order to properly understand global warming. In the next section, the Pacific Decadal Oscillation (PDO) is presented as a typical example of decadal variability observed in SSTs.

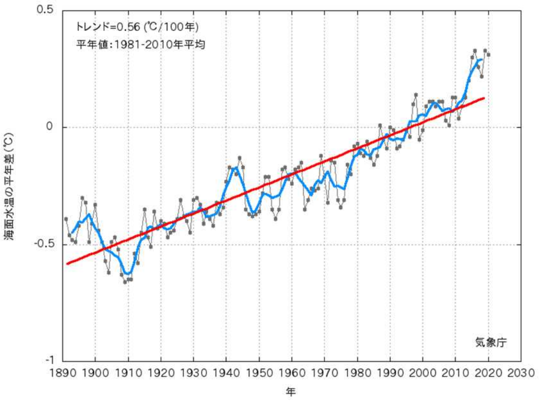

Figure 2.5-1 Time-series representation of global average sea surface temperature anomalies from 1891 to 2020

The black, blue and red lines indicate annual anomalies, the five-year running mean and the long-term linear trend, respectively. Anomalies are deviations from the 1981 – 2010 average.

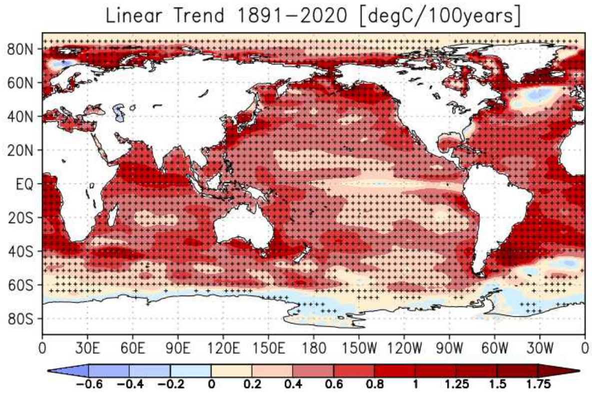

Figure 2.5-2 Linear trend of annual mean sea surface temperature during the period from 1891 to 2020 (°C per century)

Plus signs indicate statistically significant trends with a confidence level of 95%.

---

[20] The results of analysis regarding tendencies of SSTs worldwide and around Japan are published on JMA's website.
https://www.data.jma.go.jp/kaiyou/english/long_term_sst_global/glb_warm_e.html
https://www.data.jma.go.jp/kaiyou/english/long_term_sst_japan/sea_surface_temperature_around_japan.html

2.5.2 Sea surface temperature (around Japan)

Figure 2.5-3 shows increase rates of area-averaged annual mean SSTs for 13 areas around Japan. The average SST of all areas around Japan has risen by +1.16°C per century, which is higher than the corresponding value for the North Pacific (+0.55°C per century).

It is virtually certain (statistically significant at a confidence level of 99%) that SSTs have risen by between +0.78 and +1.75°C per century in the sea off Kushiro, the sea off Sanriku, eastern and southern parts of the sea off Kanto, the sea off Shikoku and Tokai, east of Okinawa, the central and southwestern parts of the Sea of Japan, the Yellow Sea, the East China Sea, and the sea around the Sakishima Islands (areas E1-3, S1-3, N2-3, and W1-4). SSTs in the northeastern part of the Sea of Japan (area N1) exhibit no statistical long-term trend.

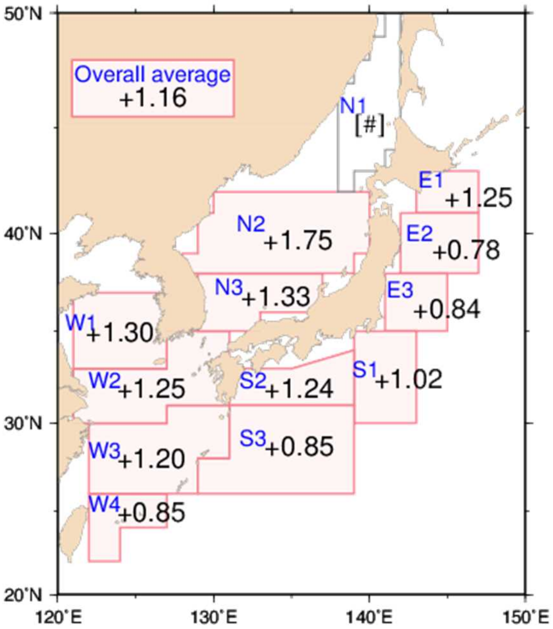

Area number	Area name
E1	Sea off Kushiro
E2	Sea off Sanriku
E3	Eastern part of the sea off Kanto
S1	Southern part of the sea off Kanto
S2	Sea off Shikoku and Tokai
S3	East of Okinawa
N1	Northeastern part of the Sea of Japan
N2	Central part of the Sea of Japan
N3	Southwestern part of the Sea of Japan
W1	Yellow Sea
W2	Northern part of the East China Sea
W3	Southern part of the East China Sea
W4	Sea around the Sakishima Islands

Figure 2.5-3 Increase rates of area-averaged annual mean SSTs around Japan from 1900 to 2020 (°C per century) Areas with no symbol have statistical significant trend at confidence levels of 99%. Areas marked with [#] are those where no discernible trend is seen due to large SST variability factors such as decadal oscillation.

2.6 El Niño/La Niña [21] and PDO (Pacific Decadal Oscillation) [22]

○ A La Niña event emerged in summer 2020 and continued for the rest of the year.

○ Negative PDO index values were generally observed from around 2000 to the early 2010s. Thereafter, the annual mean values have been consecutively positive since 2014.

2.6.1 El Niño/La Niña

An El Niño event is a phenomenon in which sea surface temperatures (SSTs) are above normal over the equatorial Pacific from near the date line to the coast of South America for around a year. In contrast, a La Niña event is a phenomenon in which SSTs are below normal over the same area. Both events occur every few years, causing changes in global atmospheric circulations which result in abnormal weather conditions worldwide. In Japan, cooler summers and warmer winters tend to appear during El Niño events, while hotter summers and colder winters tend to appear during La Niña events.

Figure 2.6-1 shows a time-series representation of SST deviations from climatological means based on a sliding 30-year period for the El Niño monitoring region (5°N – 5°S, 150°W – 90°W) and SST deviations from reference values based on linear extrapolation with respect to the latest sliding 30-year period for the tropical western Pacific region (Eq. – 15°N, 130 – 150°E) since 2010. SSTs in the El Niño monitoring region were near the relevant climatological means from January to May 2020, and have remained below these values since June 2020. SSTs in the Western Pacific region were below the related reference values from January to March of 2020, and have remained above these levels since June 2020. These variations are consistent with the presence of La Niña conditions from summer 2020 onward.

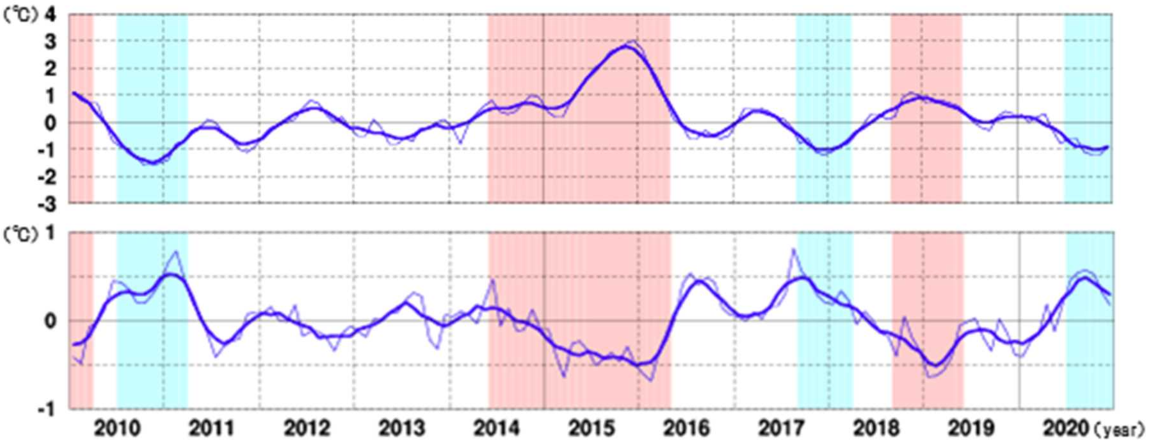

Figure 2.6-1 Time-series representations of SST deviations from the climatological mean based on a sliding 30-year period for the El Niño monitoring region (top) and SST deviations from reference values based on linear extrapolation with respect to the latest sliding 30-year period for the Western Pacific (bottom)

Thin lines indicate monthly means, and smooth thick curves indicate the five-month running mean.

Red shading denotes El Niño periods, and blue shading denotes La Niña periods.

---

[21] See the Glossary for terms relating to El Niño phenomena. Monthly diagnosis reports, ENSO monitoring products, ENSO indices and El Niño outlooks are published on JMA's website.
https://ds.data.jma.go.jp/tcc/tcc/products/elnino/index.html

[22] The PDO index time series is published on JMA's website.
https://ds.data.jma.go.jp/tcc/tcc/products/elnino/decadal/pdo.html

2.6.2 Pacific Decadal Oscillation

SST variability is also observed on time scales ranging from one to several decades in addition to El Niño/La Niña events, whose time scale is several years, and long-term trends associated with global warming. Among these, the atmosphere and oceans tend to co-vary with a period of more than ten years in the North Pacific in a phenomenon known as the Pacific Decadal Oscillation (PDO). When SSTs are lower (higher) than their normals in the central part of the North Pacific, those in its part along the coast of North America are likely to be higher (lower) than their normals. This seesaw pattern changes slowly, and appears repeatedly with a period of more than ten years. The PDO index, which is defined by the SST anomaly pattern in the North Pacific, is used as a measure of phase and strength of the oscillation. Since both the PDO index and SST anomaly patterns associated with PDO are estimated based on monthly mean SST anomalies, it is noted that they include relatively short-timescale variabilities such as El Niño/La Niña events in addition to decadal to multi-decadal components.

When the PDO index is positive (negative), SSTs in the central part of the North Pacific are likely to be lower (higher) than their normals in addition to those along the coast of North America, and those in the equatorial part from near the date line to the coast of South America are likely to be higher (lower) than normal. This tendency is analogous to the patterns observed in El Niño (La Niña) events (Figure 2.6-2). Additionally, sea level pressures (SLPs) in the high latitudes of the North Pacific are likely to be lower (higher) than their normals in the same time (Figure 2.6-3). This indicates that the Aleutian Low is stronger (weaker) than its normal in winter and spring. These atmospheric variations affect meteorological conditions mainly in North America. When the PDO index is positive, winter temperatures tend to be high in the northwestern part of North America and the northern part of South America, and low in the southeastern part of the USA and in parts of China (Mantua and Hare, 2002).

The PDO index was generally positive from the late 1920s to the early 1940s and from the late 1970s to around 2000, and was generally negative from the late 1940s to the mid-1970s and from around 2000 to the early 2010s. From a view point of the decadal variability of the PDO index, the annual mean PDO index value has remained positive since 2014 (Figure 2.6-4).

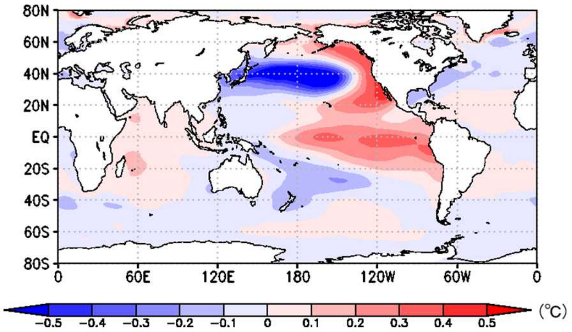

Figure 2.6-2 Typical SST anomaly patterns in the positive phase of the PDO

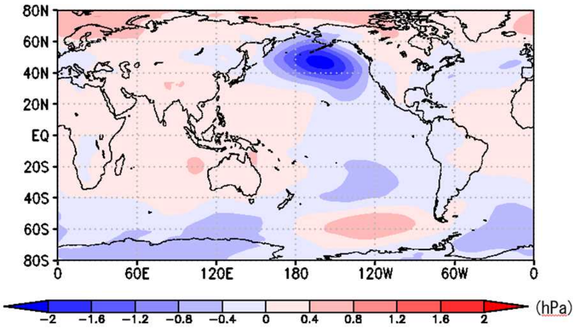

Figure 2.6-3 Typical SLP anomaly patterns in the positive phase of the PDO

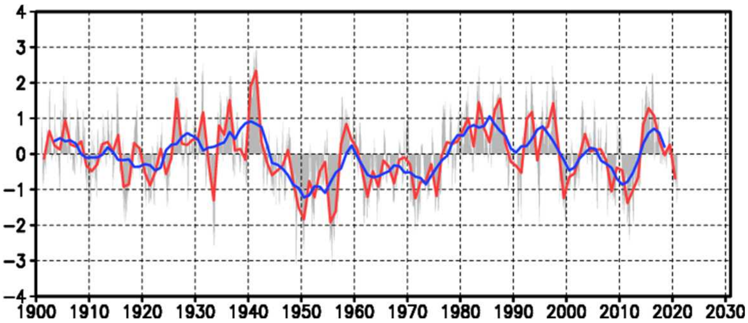

Figure 2.6-4 Time-series of the PDO index

The red line represents annual mean values for the PDO index, the blue line represents five-year running mean values, and the gray bars represent monthly values.

2.7 Global ocean heat content[23]

○ Globally integrated ocean heat content (OHC) exhibits a long-term increase.
○ OHC has exhibited a higher rate of increase since the mid-1990s.

Oceans have a significant impact on the global climate because they cover about 70% of the earth's surface and have high heat capacity. The Intergovernmental Panel on Climate Change Special Report on the Ocean and Cryosphere in a Changing Climate (IPCC, 2019) said that approximately 90% of heat energy in the earth's system was present in oceans since 1970.

It is virtually certain that globally integrated ocean heat content (OHC) from 0 to 2,000 m exhibits a long-term increase (statistically significant at a confidence level of 99%) (Figure 2.7-1). OHC had risen by approximately 43 × 10^{22} J in 2020 relative to 1955. Since the mid-1990s, the rate of increase (9.8× 10^{22} J per decade for 1993 –2020) has risen (3.9 × 10^{22} J per decade for 1955 – 1993). IPCC (2019) also reported an accelerated increase of ocean heat uptake.

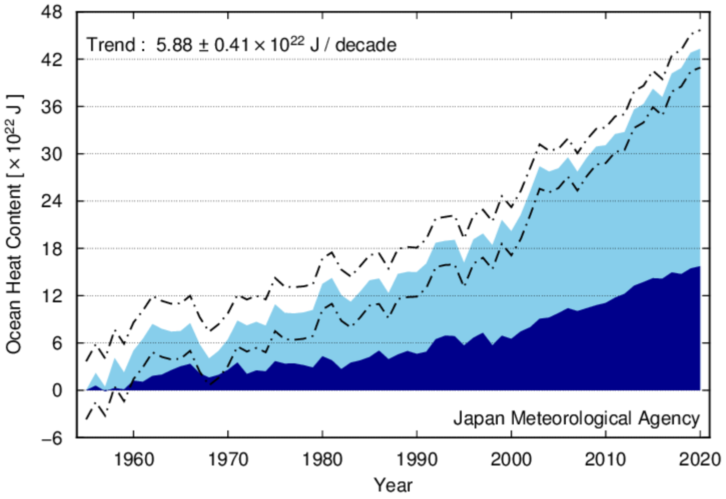

Figure 2.7-1 Time-series representation of globally integrated ocean heat content relative to 1955

The light- and dark-blue areas show annual means for global integrals of 0 to 700 m and 700 to 2,000 m, respectively, for ocean heat content relative to 1955. The dot-dash lines indicate a 95% confidence level for ocean heat content above 2,000 m.

---

[23] The results of ocean heat content analysis are published on JMA's website.
https://www.data.jma.go.jp/gmd/kaiyou/english/ohc/ohc_global_en.html

2.8 Sea levels around Japan [24]

○ No long-term trend of sea level rise has been observed in coastal areas of Japan over the last 100 years, but such a trend has been observed since the 1980s

Sea levels in Japanese coastal areas exhibit no significant rise from 1906 to 2020 (Figure 2.8-1).

This is attributed to variations over 10- to 20-year and 50-year-plus periods for the period from 1906 to 2020. The major factor behind sea level variations with 10- to 20-year periods is the variability of atmospheric circulation over the North Pacific. Westerlies in the mid-latitudes of the Northern Hemisphere are strengthened in boreal winter, and the consequent decadal variations in turn cause sea level variations in the central North Pacific. These propagate westward due to the earth's rotation, causing sea level rise around Japan.

However, a trend of sea level rise has been observed since the 1980s. The annual mean sea level around Japan in 2020 was 87 mm higher than the normal (i.e., the 1981 – 2010 average), making it the highest since 1906.

The IPCC Special Report on the Ocean and Cryosphere in a Changing Climate 2019 (IPCC, 2019) concluded that the global mean sea level (GMSL) has been rising, with acceleration in recent decades due to increasing rates of ice loss from the Greenland and Antarctic ice sheets (very high confidence), as well as continued glacier mass loss and ocean thermal expansion. The report also identified a total GMSL rise for the period from 1902 to 2010 of 0.16 [0.12 to 0.21] m and a GMSL rate for 2006 to 2015 of 3.6 [3.1 to 4.1] mm/year, representing unprecedented levels for the last century (high confidence), and approximately 2.5 times the rate for 1901 to 1990 of 1.4 [0.8 to 2.0] mm/year (values in square brackets show the 95% uncertainty range). In contrast to the globally averaged rate noted in the IPCC report, sea levels in coastal areas of Japan exhibited no significant rise from 1906 to 2010. Recent rates of rise around the country have been 4.1 [0.1 to 8.2] mm/year from 2006 to 2015. These figures are comparable to those observed for the global average in recent years.

Sea levels along the coast of Japan are predominantly variable with decadal cycles, but the contributions of these variations and changes associated with global warming have not been quantitatively evaluated. Continuous monitoring is needed to determine the long-term trend of sea level rise caused by global warming.

---

[24] Sea levels around Japan are published on the JMA's website.
https://www.data.jma.go.jp/gmd/kaiyou/english/sl_trend/sea_level_around_japan.html

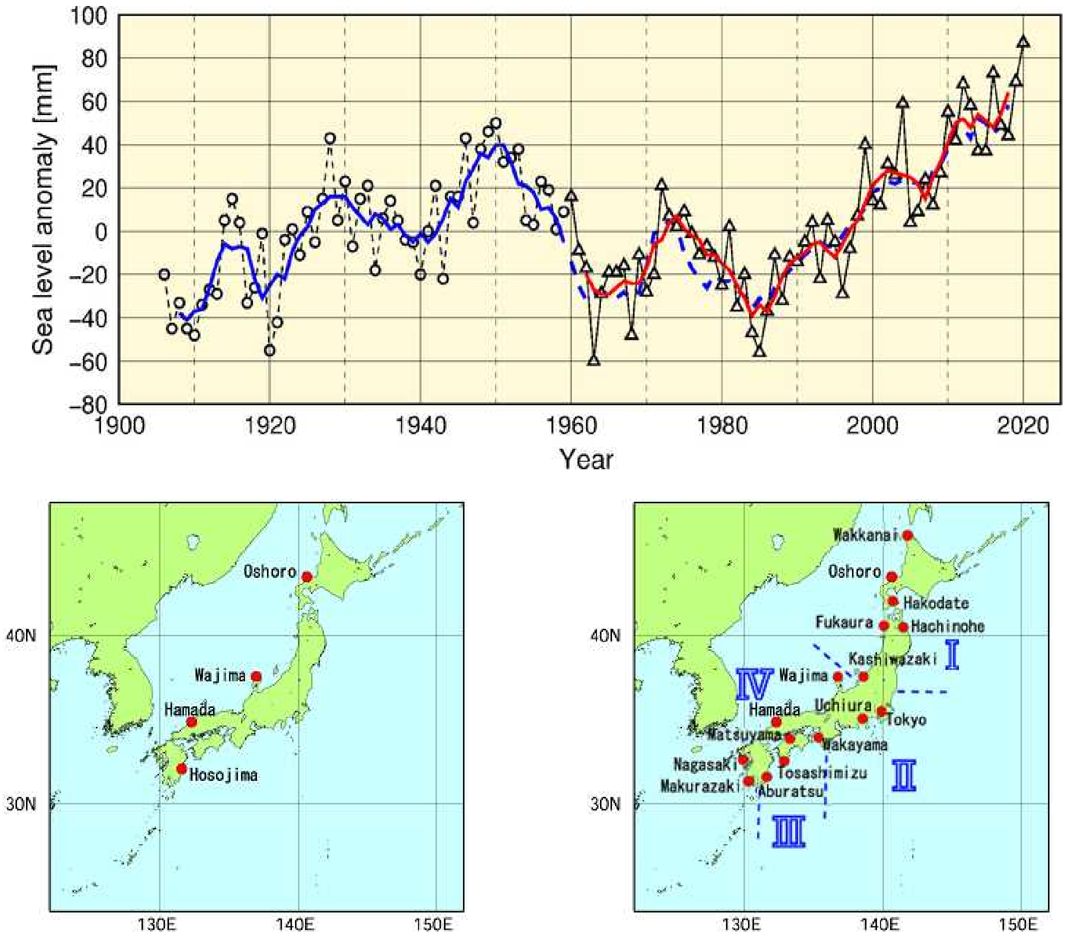

Figure 2.8-1 Time-series representation of annual mean sea levels (1906 – 2020) and locations of tide gauge stations

Tide gauge stations assessed as being affected to a lesser extent by crustal movement are selected. The four stations shown on the map on the left are used for the period from 1906 to 1959, and the sixteen shown on the right are used for the period since 1960. From 1906 to 1959, a time-series representation of mean annual mean sea level anomalies for the selected stations is shown. For the period since 1960, the nation's islands were then divided into four regions based on sea level variation characteristics, annual mean sea level anomalies were averaged for each of the regions, and the variations were plotted in the figure. The four regions are I: from Hokkaido to Tohoku district; II: from Kanto to Tokai district; III: from the Pacific coast of Kinki to that of Kyushu district; and IV: from Hokuriku to East China Sea coast of Kyushu district. Sea level variations are plotted on the chart as a time-series representation of annual mean sea level anomalies for each year, obtained using the 1981 to 2010 average as the normal. The solid blue line represents the five-year running mean of annual sea level anomalies averaged among the four stations shown in the lower left map, while the solid red line represents that averaged among the four divided regions in the lower right map. The dashed blue line represents the value averaged among the four stations shown in the lower left map for the same period shown by the solid red line (after 1960) for reference. The coefficient of correlation between the solid red line and the dashed blue line from 1962 to 2018 is as high as 0.98. Accordingly, the extent to which changing the tide gauge stations used in the monitoring affects the analysis of variance of sea level anomalies can be regarded as small. Among the tide gauge stations, those at Oshoro, Kashiwazaki, Wajima and Hosojima belong to the Geospatial Information Authority of Japan. Sea level data for the Tokyo station are available from 1968 onward. Sea level data for the period from 2011 to 2020 from Hakodate, Fukaura, Kashiwazaki, Tokyo and Hachinohe were not used due to possible influences from the 2011 off the Pacific coast of Tohoku Earthquake.

2.9 Sea ice[25]

○ The sea ice extent in the Arctic Ocean is decreasing. In 2020, the annual minimum sea ice extent in the Arctic Ocean was 3.72 × 10^6 km^2, which was the second-lowest value since 1979.

○ The annual maximum sea ice extent in the Antarctic Ocean is extremely likely to increase.

○ The maximum sea ice extent in the Sea of Okhotsk shows a decreasing trend of 0.061 × 10^6 km^2 per decade.

2.9.1 Sea ice in Arctic and Antarctic areas (Figures 2.9-1, 2.9-2, 2.9-3)

Sea ice is formed when sea water in the Arctic and Antarctic freezes. As the albedo (reflection coefficient) of sea ice is greater than that of the ocean surface, sea ice extent reductions caused by global warming result in more solar energy absorption at the surface, which in turn accelerates global warming. Sea ice also affects deep-ocean circulation because the expelled salt as it forms increases the salinity (and therefore the density) of the water below it causing the water to sink.

It is virtually certain that there has been a long-term trend of decrease in sea ice extent in the Arctic Ocean since 1979 when continuous monitoring of sea ice using satellite sensors with similar properties started (statistically significant at a confidence level of 99%). In particular, the reduction in the annual minimum extent is notable. The rate of decrease in the annual minimum up to 2020 was 0.091 × 10^6 km^2 per year. Meanwhile, it is extremely likely that there has been a long-term trend of increase in sea ice extent at a rate of 0.015 × 10^6 km^2 per year in the annual maximum sea ice extent in the Antarctic Ocean (statistically significant at the confidence level of 95%). The value for the period from 2016 to 2019 was lower than the normal, but began to increase again in 2018 (Figure 2.9-1).

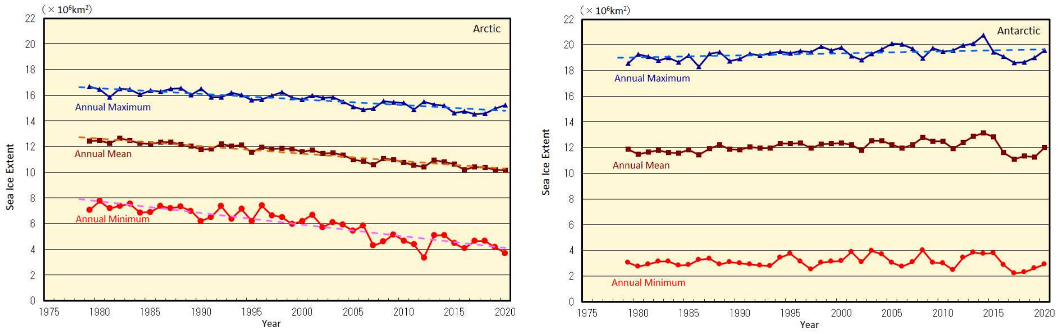

Figure 2.9-1 Time-series representations of annual maximum, annual mean and annual minimum sea ice extent in the Arctic Ocean (including the Sea of Okhotsk and the Bering Sea) (left) and in the Antarctic Ocean (right) from 1979 to 2020

The solid blue, brown and red lines indicate the annual maximum, the annual mean and the annual minimum sea ice extent, respectively. The dashed lines indicate the linear trends. Sea ice extents are calculated from brightness temperature data provided by NASA (the National Aeronautics and Space Administration) and NSIDC (the National Snow and Ice Data Center).

In 2020, the annual maximum Arctic sea ice extent was 15.25 × 10^6 km^2 on March 3, marking the eleventh-lowest value since 1979. The extent subsequently decreased during spring and summer in the Northern Hemisphere and reached its annual minimum of 3.72 × 10^6 km^2 on

---

[25] Information on sea ice in the Arctic/Antarctic, and in the Sea of Okhotsk are published on JMA's website.
https://www.data.jma.go.jp/gmd/kaiyou/english/seaice_global/series_global_e.html (Arctic/Antarctic)
https://www.data.jma.go.jp/gmd/kaiyou/english/seaice_okhotsk/series_okhotsk_e.html (Sea of Okhotsk)

September 8, marking the second-lowest value since 1979. Meanwhile, the Antarctic sea ice extent was at its annual minimum of 2.89 × 10^6 km^2 on February 16, marking the thirteenth-lowest value since 1979. The extent subsequently increased during the autumn and winter months of the Southern Hemisphere and reached its annual maximum of 19.56 × 10^6 km^2 on September 26, marking the thirteenth-highest value since 1979 (Figures 2.9-1, 2.9-2, 2.9-3).

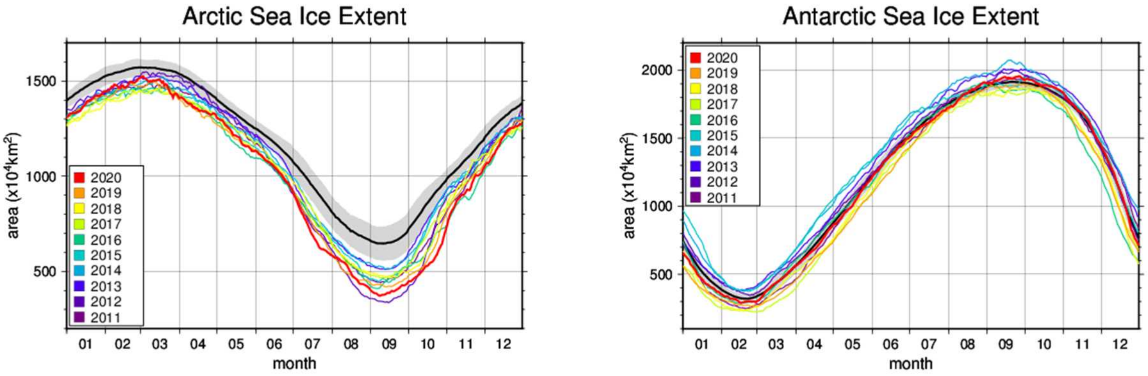

Figure 2.9-2 Annual variations of sea ice extent in the Arctic (left) and Antarctic (right) areas in 2020 (red line) Black lines represent the normal, and shading represents the range of the normal.

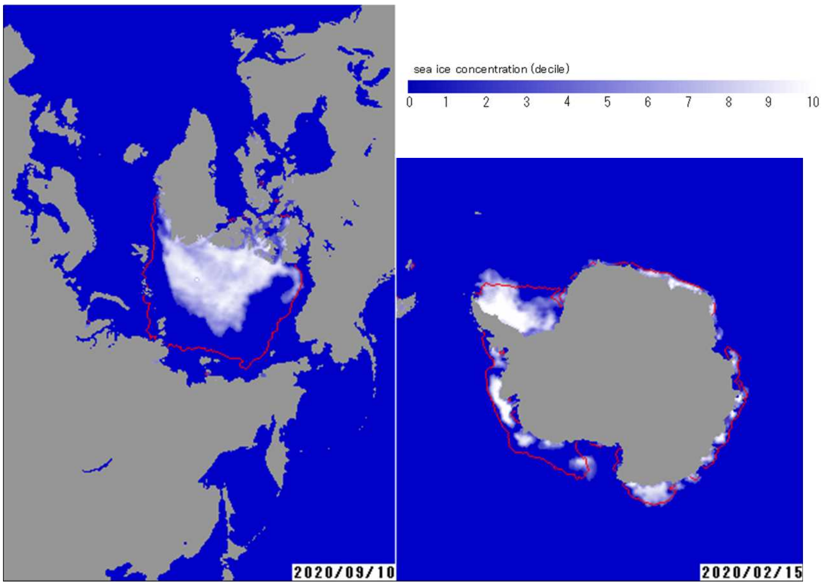

Figure 2.9-3 Annual minimum sea ice distribution for the Arctic and Antarctic

The figure on the left shows Arctic sea ice concentration on September 10 2020, and on the right is Antarctic sea ice concentration on February 15 2020. The red lines represent the normal sea ice edge for the relevant days.

2.9.2 Sea ice in the Sea of Okhotsk (Figure 2.9-4)

The Sea of Okhotsk is the southernmost sea in the Northern Hemisphere where sea ice is observed across a wide area. The variation of the sea ice in the Sea of Okhotsk has effect on climate in coastal area facing the Sea of Okhotsk in Hokkaido and water quality of Oyashio.

The maximum[26] sea ice extent in the Sea of Okhotsk shows large interannual variations. However, it is virtually certain that it exhibited a long-term trend of decrease for the period from 1971 to 2020 (statistically significant at the confidence level of 99%). The maximum extent has decreased by 0.061 × 10^6 km^2 per decade (corresponding to 3.9% of the Sea of Okhotsk's total area).

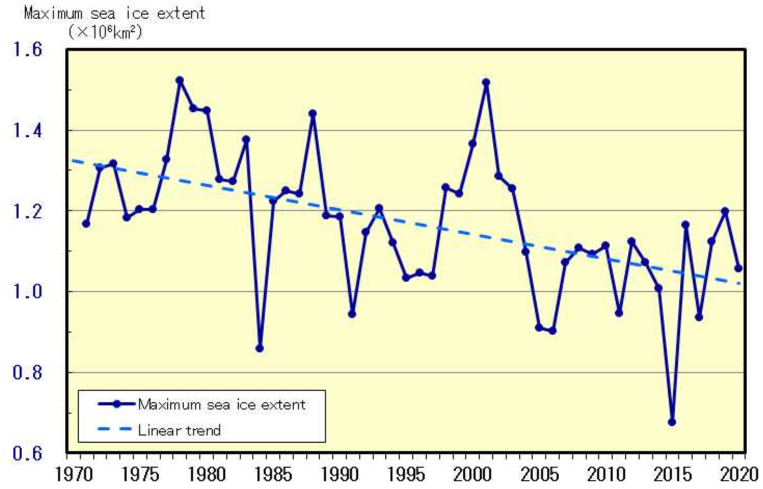

Figure 2.9-4 Time-series representations of maximum sea ice extent for the Sea of Okhotsk from 1971 to 2020
Straight line indicates the linear trend.

2.10 Snow cover in the Northern Hemisphere

○ It is extremely likely that a decreasing trend is observed in the interannual variability of the total snow cover extent in the Northern Hemisphere for January, June and the period from September to December and in Eurasia for January, March, June and the period from September to December.

○ In winter 2019/2020, there were fewer days of snow cover than normal from eastern Europe to Western Russia.

JMA monitors snow-cover variations in the Northern Hemisphere using analysis data from satellite observations[27] based on its own algorithm. The average seasonal migration of snow cover in the Northern Hemisphere normally peaks around January - February and decreases in spring.

In the Northern Hemisphere (north of 30°N), it is extremely likely (statistically significant at a confidence level of 95%) that a decreasing trend is observed in the interannual variability of the total snow cover extent over the 33-year period from 1988 to 2020 for January, June and the period from September to December, while no discernible trend is seen for the period from February to May (Figure 2.10-1 (a) and (c)). In Eurasia (north of 30°N from 0° to 180°E), it is extremely likely (statistically significant at a confidence level of 95%) that a decreasing trend is

---

[26] The maximum sea ice extent: It shows sea ice extent that sea ice was the most expanding of every five days in the winter.

[27] The Defense Meteorological Satellite Program (DMSP) polar-orbiting satellites of the USA, equipped with the Special Sensor Microwave/Imager (SSM/I) and the Special Sensor Microwave Imager Sounder (SSMIS)

observed in the interannual variability of the total snow cover for January, March, June and the period from September to December, while no discernible trend is seen for February, the period from April to May and the period from July to August (Figure 2.10-1 (b) and (d)). In winter (December to February) 2019/2020, there were fewer days of snow cover than normal from eastern Europe to Western Russia (Figure 2.10-1 (e)) in association with the Arctic Oscillation in its positive phase. In November 2020, there were fewer days of snow cover than normal from northern Europe to Western Russia (Figure 2.10-1 (f)).

The albedo of snow-covered ground (i.e., the ratio of solar radiation reflected by the surface) is higher than that of snow-free ground. The variability of snow cover has an impact on the earth’s surface energy budget and radiation balance, and therefore on the climate. In addition, snow absorbs heat from its surroundings and melts, thereby providing soil moisture and related effects on the climate system. The variability of atmospheric circulation and oceanographic conditions affects the amount of snow cover, which exhibits a close and mutual association with climatic conditions. Snow-cover variations in Eurasia and other parts of the Northern Hemisphere may affect climate conditions in Japan, but the mechanisms behind such a potential influence remain unclear. The accumulation of future observation data in addition to the current body of information and the implementation of related research are expected to increase the reliability of statistical work to identify trends of snow cover extent and help to elucidate how snow-cover variations affect climate conditions.

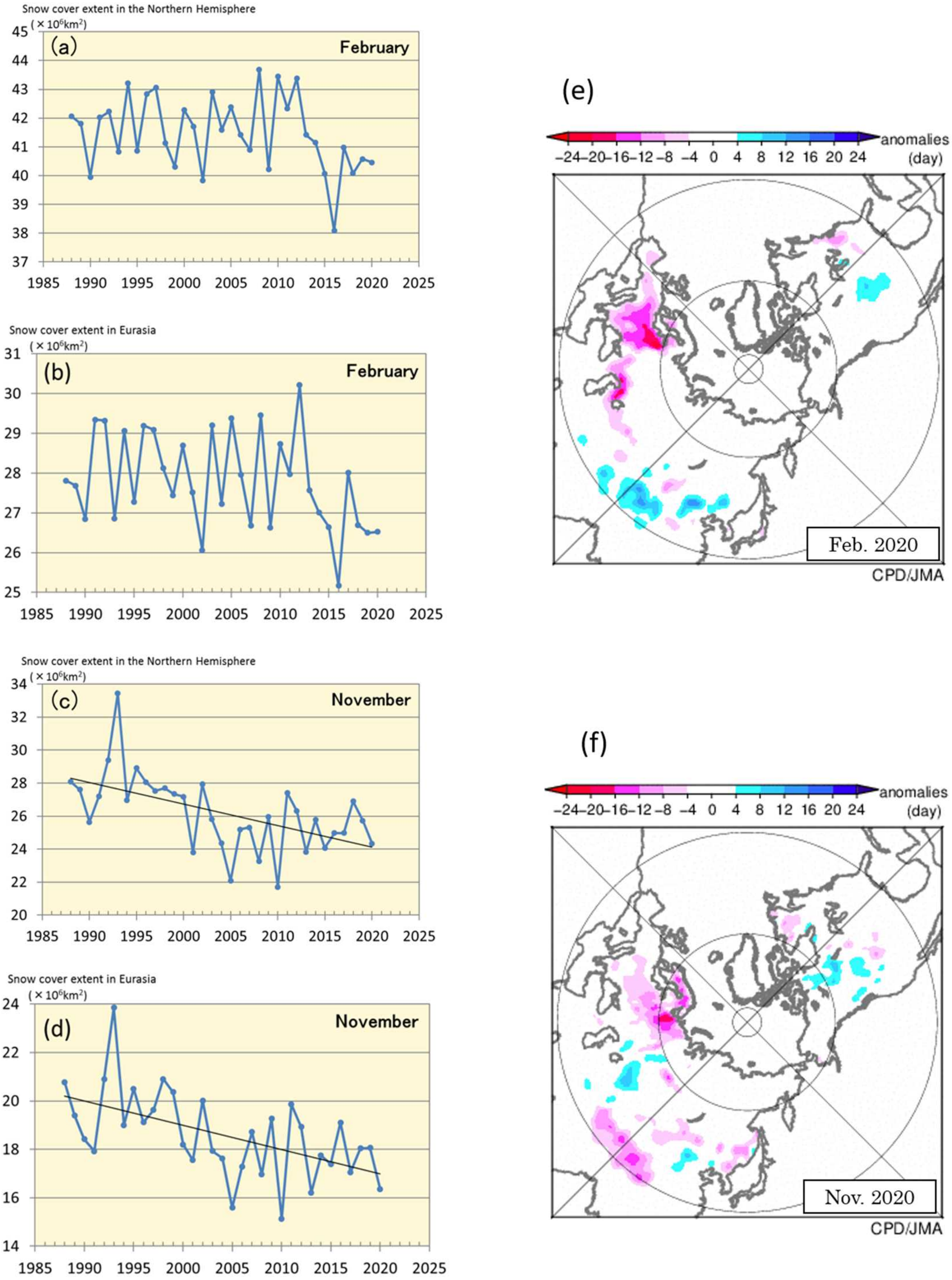

Figure 2.10-1 Interannual variations in the total area of monthly snow cover (km^2) in the Northern Hemisphere (north of 30°N) for (a) February and (c) November and in Eurasia (north of 30°N, from 0° to 180°E) for (b) February and (d) November from 1988 to 2020, and anomalies in the number of days with snow cover for (e) February and (f) November in 2020

(a) - (d): The blue lines indicate the total snow cover area for each year, and the black lines show linear trends (statistically significant at a confidence level of 95%).

(e) - (f): Blue (red) shading indicates more (fewer) days of snow cover.

The base period for the normal is 1989 – 2010.

Chapter 3 Atmospheric and Marine Environment Monitoring[28]

3.1 Monitoring of greenhouse gases[29]

○ Concentrations of carbon dioxide both in the air and in oceans are increasing.

○ Concentrations of atmospheric methane have shown an ongoing increase (with the exception of a stationary phase from 1999 to 2006).

○ Concentrations of atmospheric nitrous oxide are increasing.

○ Among halocarbons, concentrations of atmospheric chlorofluorocarbons are decreasing, while those of hydrofluorocarbons are increasing.

JMA operates the World Data Centre for Greenhouse Gases (WDCGG)[30] to collect, maintain and provide data on greenhouse gases for related monitoring on a global scale under the Global Atmosphere Watch (GAW) Programme of the World Meteorological Organization (WMO). Analysis of data reported to WDCGG shows that the global mean concentration of greenhouse gases with strong impacts on global warming (in particular, carbon dioxide (CO_2), methane (CH_4) and nitrous oxide (N_2O)) continues to increase (Table 3.1-1).

In Japan, JMA monitors surface-air concentrations of greenhouse gases via three observation stations at Ryori in Ofunato, Minamitorishima in the Ogasawara Islands and Yonagunijima in the Nansei Islands. JMA research vessels are used to observe oceanic and atmospheric CO_2 in sea areas near Japan and in the western North Pacific. In addition, sampling of greenhouse gases in upper-air areas using cargo aircraft was commenced in 2011 (Figure 3.1-1).

Table 3.1-1 Atmospheric concentrations of major greenhouse gases (2019)[31]

	Atmospheric mole fraction			Absolute increase from 2018	Relative increase from 2018	Lifetime
	Pre-industrial level around 1750	Global mean in 2019	Relative increase from Pre-industrial level			
Carbon dioxide	About 278 ppm	410.5 ppm	+ 48 %	+2.6 ppm	+0.64 %	-
Methane	About 722 ppb	1,877 ppb	+160 %	+8 ppb	+0.43 %	12.4 years
Nitrous oxide	About 270 ppb	332.0 ppb	+ 23 %	+0.9 ppb	+0.27 %	121 years

---

[28] In this chapter, data from the period until 2019 are used for certain results where time is needed for collection and analysis of observation data regarding greenhouse gases around the world.

[29] Information on greenhouse gas monitoring is published on JMA's website.
https://www.data.jma.go.jp/ghg/info_ghg_e.html (Atmospheric greenhouse gases)
https://www.data.jma.go.jp/gmd/kaiyou/english/oceanic_carbon_cycle_index.html (oceanic greenhouse gases and ocean acidification)

[30] See the WDCGG website for more information.
https://gaw.kishou.go.jp/

[31] Data on the annual mean mole fraction in 2019 and its absolute and relative differences from the previous year are from WMO (2020), while data on pre-industrial levels and lifetime are from IPCC (2013). The lifetime of gas as referred to here describes the time scale over which a local instantaneous increment of gas decays. The increase from pre-industrial levels is calculated from mole fractions for the pre-industrial era and 2019.

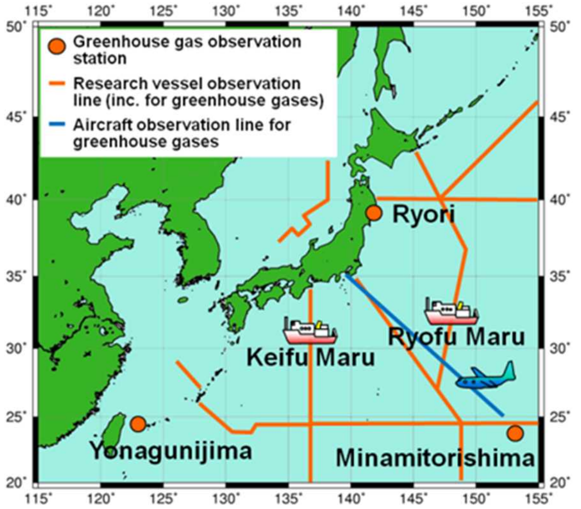

Figure 3.1-1 JMA's greenhouse gas observation network
Observation stations at Ryori, Minamitorishima and Yonagunijima and regular monitoring routes of research vessel and cargo aircraft

3.1.1 Concentration of carbon dioxide

(1) Concentration of global atmospheric carbon dioxide

The global mean concentration of atmospheric CO_2 shows a trend of increase with ongoing seasonal variations (Figure 3.1-2), primarily due to influences associated with human activity such as fossil fuel combustion and deforestation. Some anthropogenic CO_2 is absorbed by the terrestrial biosphere and the oceans, while the rest remains in the atmosphere. As most major sources of CO_2 are located in the Northern Hemisphere, concentrations tend to be higher in the mid- and high latitudes there and lower in the Southern Hemisphere (Figure 3.1-3).

The seasonal variability of CO_2 concentration is generally attributable to terrestrial biosphere activity. In summer, active plant photosynthesis consumes masses of CO_2, while emissions from plant respiration and organic-matter decomposition become dominant in winter. As a result, the annual maximum concentration is observed from March to April in the Northern Hemisphere and from September to October in the Southern Hemisphere. Seasonal variations exhibit larger amplitudes in the mid- and high latitudes of the Northern Hemisphere than in the ocean-rich Southern Hemisphere (Figure 3.1-3). Accordingly, the global mean CO_2 concentration usually peaks around April, reflecting the seasonal variations of the Northern Hemisphere.

WDCGG analysis shows that global mean surface CO_2 concentration increased by 2.6 ppm from 2018 to 2019, reaching as much as 410.5 ppm (Table 3.1-1). The most recent 10-year average annual growth rate is 2.4 ppm/year, as opposed to the corresponding value of 1.5 ppm/year for the 1990s.

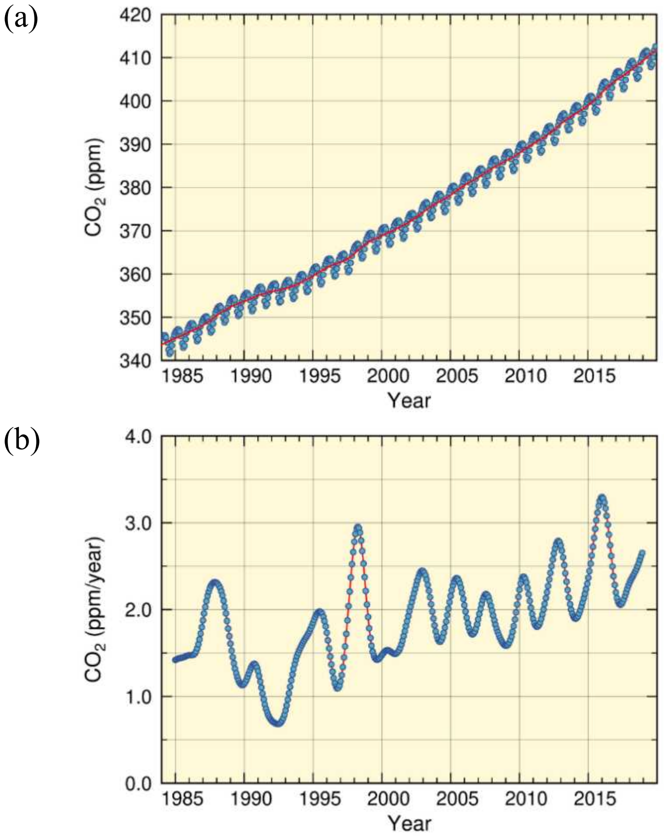

Figure 3.1-2 Global mean concentration of atmospheric CO_2 (a) and annual growth rate (b)

In the upper panel the blue dots are monthly values, and the red line represents the corresponding sequence after removal of seasonal variations. From the latter, the growth rate is derived and shown in the lower panel. Graph content is based on analysis of observation data reported to WDCGG using the method of WMO (2009). Data contributors are listed in WMO (2021).

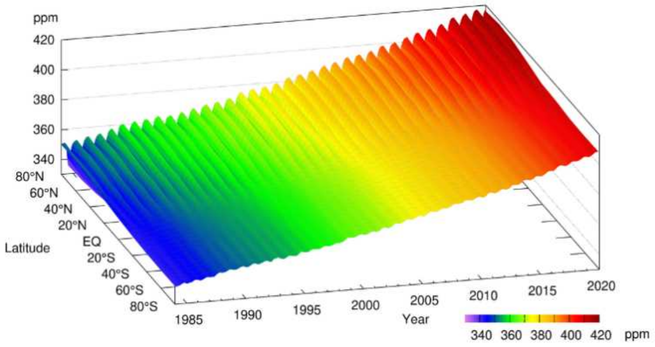

Figure 3.1-3 Latitudinal distribution of atmospheric CO_2 concentrations

The data set and analysis method are as per Figure 3.1-2.

The growth rate of CO_2 concentration exhibits significant interannual variations (Figure 3.1-2 (b)). Major increases in concentration often coincide with El Niño events, largely because the terrestrial biosphere emits more CO_2 than usual under such conditions. In particular, El Niño events bring about high temperatures and droughts in tropical areas and elsewhere, thereby promoting plant respiration and organic-matter decomposition in soil and hindering plant photosynthesis (Keeling *et al.*, 1995; Dettinger and Ghil, 1998).

Figure 3.1-4 illustrates net CO_2 uptake by the terrestrial biosphere as estimated using the method of Le Quéré *et al.* (2016). Here, CO_2 uptake is defined as the amount of anthropogenic emissions minus the increment of atmospheric concentration and the amount of uptake by oceans. The low uptake by the terrestrial biosphere in 2015 and 2016 is generally attributed to the 2014 – 2016 El Niño event (WMO, 2018b). The annual net CO_2 uptake in 2015 and 2016 was 2.1 ± 1.1 GtC/year and 1.8 ± 1.1 GtC/year, respectively, both of which were lower than the 10-year average of 3.2 ± 1.0 GtC/year for the period 2008 – 2017. Similar suppression of net CO_2 uptake was observed in association with the El Niño events of 1997/1998 and 2002/2003. In 1998 in particular, the lowest net uptake since 1990 was recorded. An exception was observed from 1991 to 1992, when net CO_2 uptake by the terrestrial biosphere was large despite the presence of an El Niño event. This is attributable to the eruption of Mt. Pinatubo in June 1991, which triggered worldwide low temperatures and inhibited CO_2 emissions from organic-matter decomposition in soil (Keeling *et al*., 1996; Rayner *et al*., 1999).

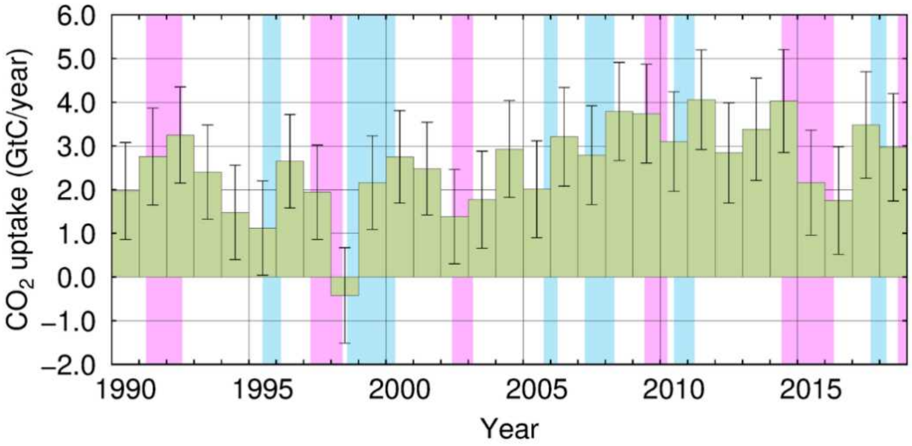

Figure 3.1-4　Annual net CO_2 uptake by the terrestrial biosphere

In this analysis, the net CO_2 uptake is estimated by subtracting the annual increment of atmospheric CO_2 and the amount of uptake by oceans from the amount of anthropogenic emissions. The amount of anthropogenic emissions, stemming from fossil fuel combustion and land-use changes, is based on Friedlingstein *et al*. (2020). The annual increment of atmospheric CO_2 is the annual mean of the monthly means shown in Figure 3.1-2 (b). Oceanic uptake is based on Iida *et al*. (2020; see also Section 3.1.1 (3)), and incorporates emissions associated with the natural carbon cycle, corresponding to 0.7 GtC/year (IPCC 2013). Error bars indicate 68% confidence levels. El Niño and La Niña periods are shaded in red and blue, respectively. A negative CO_2 uptake equates to an emission.

(2) Concentration of atmospheric carbon dioxide in Japan

Concentrations of atmospheric CO_2 at all three of Japan's observation stations have shown a continuous increase along with seasonal variations (Figure 3.1-5 (a)). The amplitude of these variations is greater at Ryori than at the other stations because it tends to be larger in higher latitudes of the Northern Hemisphere in association with significant seasonal variations in terrestrial biosphere activity in the mid- and high latitudes (see Figure 3.1-1). Although Yonagunijima and Minamitorishima have similar latitudes, the former tends to observe higher concentrations and seasonal variations with larger amplitudes because of its greater proximity to the Asian continent, which is characterized by major anthropogenic emissions and an extensive biosphere. The annual mean CO_2 concentration in 2020 was 416.3 ppm at Ryori, 414.5 ppm at Minamitorishima and 417.2 ppm at Yonagunijima (based on preliminary estimations). The increase from the previous year was 2.3 to 2.4 ppm/year, which is comparable to the mean annual absolute increase over the last 10 years. It has been reported that anthropogenic emissions of carbon dioxide in 2020 decreased by about 7% from 2019 due to COVID-19 confinement measures (Friedlingstein *et al*., 2020), but concentrations of atmospheric CO_2 continue to increase. This means that the effects of such measures in the short term cannot be distinguished from natural year-to-year variability (WMO, 2020).

Figure 3.1-5 (b) shows growth rates of CO_2 concentrations observed at the three observation stations. High rates have been observed in most cases during the periods of El Niño events. As a recent example, a sharp increase in CO_2 concentration was observed in association with the event that ran from summer 2014 to spring 2016.

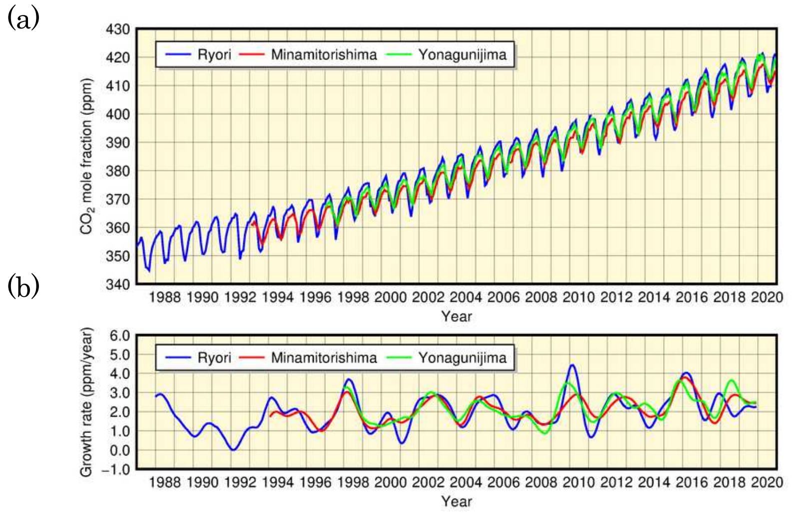

Figure 3.1-5
Monthly mean concentrations (a) and corresponding growth rates (b) of atmospheric CO_2 observed at Ryori (blue), Minamitorishima (red) and Yonagunijima (green)
The method used to calculate the growth rate is described in WMO (2009).

(3) Oceanic carbon dioxide

Based on data collected by JMA research vessels along the 137°E (3 – 34°N) and 165°E (5°S – 35°N) lines, oceanic and atmospheric $p\mathrm{CO}_2$ are increasing in the western North Pacific area (Figures 3.1-6, 3.1-7). The growth rates for oceanic and atmospheric $p\mathrm{CO}_2$ along the 137°E line from 1985 to 2020 were 1.5 – 2.1 and 1.8 – 2.0 µatm/year, respectively, while those along the 165°E line from 1996 to 2020 were 1.6 – 3.0 and 1.7 – 2.1 µatm/year, respectively. Oceanic $p\mathrm{CO}_2$ exhibits seasonal variations, being higher in summer with higher SSTs and lower in winter with lower SSTs, and the range of variation is more volatile at higher latitudes along both lines. Meanwhile, atmospheric $p\mathrm{CO}_2$ is constant and higher than those of oceanic $p\mathrm{CO}_2$ except in summer. Consequently, the ocean absorbs atmospheric CO_2 emissions overall, other than in equatorial areas, resulting in a release of CO_2 into the atmosphere over the year because oceanic $p\mathrm{CO}_2$ values are higher than those of atmospheric $p\mathrm{CO}_2$.

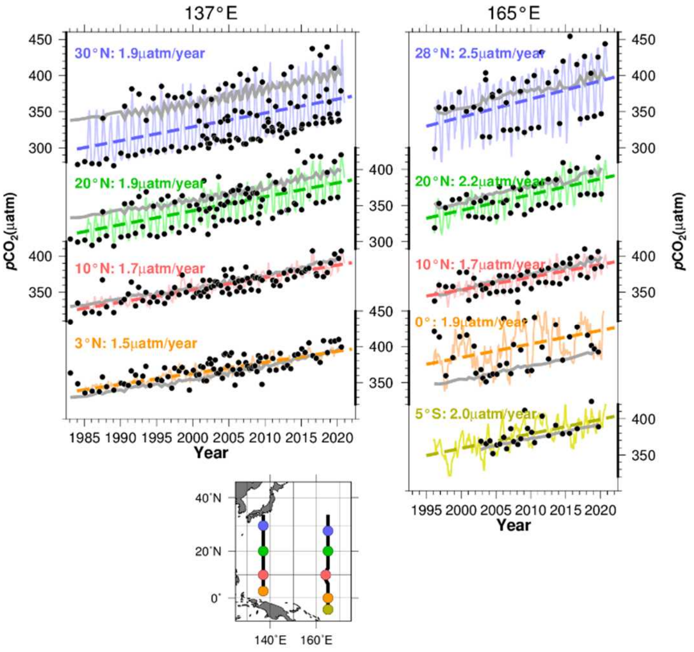

Figure 3.1-6 Annual changes in oceanic and atmospheric $p\mathrm{CO}_2$ along the 137°E (left) and the 165°E (right) lines. Black plots show oceanic $p\mathrm{CO}_2$ observation values. Solid lines represent monthly oceanic $p\mathrm{CO}_2$ values reconstructed using the method of Ishii et al. (2011), dashed lines show the long-term trend of oceanic $p\mathrm{CO}_2$, and gray lines indicate the observed values of atmospheric $p\mathrm{CO}_2$.

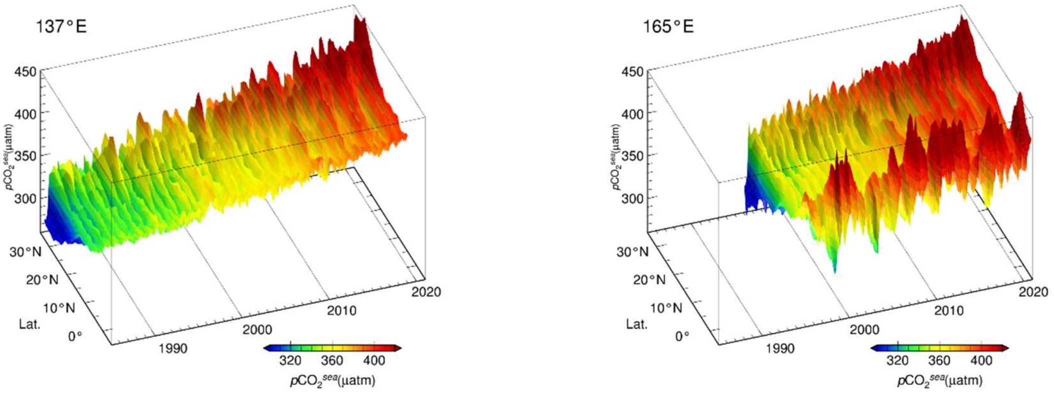

Figure 3.1-7 Time-latitude distribution of oceanic pCO_2 along the 137°E (left) and the 165°E (right) lines. Colors indicate reconstructed monthly oceanic pCO_2 value. The part on the left shows oceanic pCO_2 along the 137°E (3-34°N) since 1985 and the part on the right shows oceanic pCO_2 along the 165°E (5°S-35°N) since 1996.

Analysis of observation data reveals relationships between surface seawater CO_2 concentrations and other oceanographic parameters such as sea surface temperature (SST), salinity and chlorophyll-a concentration, which differ by region. Global oceanic CO_2 concentrations were estimated using datasets of such parameters based on these relationships, and CO_2 exchanges between the atmosphere and the ocean were calculated (Iida *et al.*, 2020). It was found that the ocean releases CO_2 into the atmosphere in equatorial regions and the northern Indian Ocean, where seawater with a high CO_2 concentration upwells and absorbs CO_2 in other regions (Figure 3.1-8 (a)). Lower SSTs in winter and biological CO_2 consumption in spring/autumn result in lower surface ocean CO_2 concentrations and therefore higher CO_2 uptake, especially in the mid-to-high latitudes. Figure 3.1-8 (b) and (c) show monthly and annual variations in global ocean CO_2 uptake, respectively. The estimated mean annual global ocean CO_2 uptake during 1990 to 2019 was 2.0 GtC per year. Considering natural CO_2 efflux of 0.7 GtC per year (IPCC, 2013), which results from riverine input to the oceans, the amount of oceanic CO_2 uptake corresponds to 30 % of all anthropogenic CO_2 emission, which IPCC (2013) estimates to be 9 GtC per year. Global ocean CO_2 uptake is affected by the variability of global SST distribution and biological activity, and decreases/increases in boreal summer/winter (Figure 3.1-8 (b)). The estimated annual global ocean CO_2 uptake has increased since 2000.

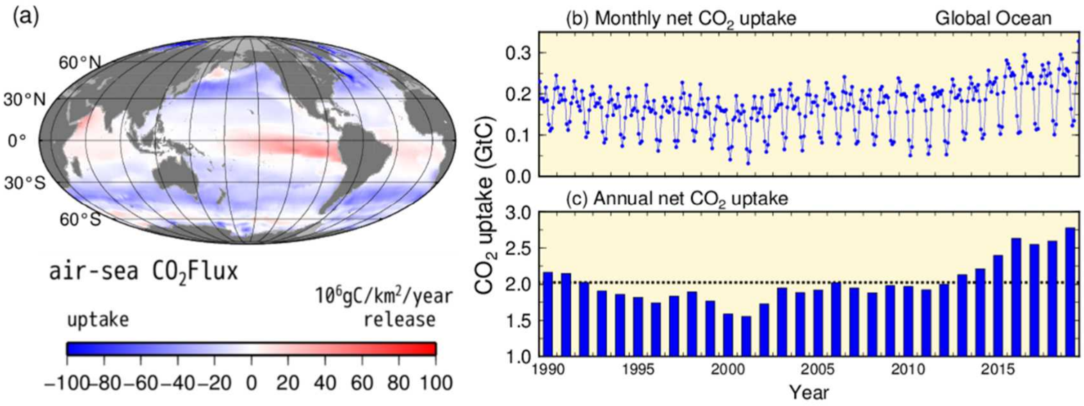

Figure 3.1-8 Distribution of global ocean CO_2 uptake/release for 2019 (a) and time-series representations of monthly (b) and annual (c) CO_2 uptake from 1990 to 2019

The blue/red area in the map on the left (a) indicates ocean uptake/release of CO_2 from/into the atmosphere. The grey area shows the border of the region analyzed. The dotted line in graph (c) shows the 2.0 GtC average for the period from 1990 to 2019.

The column inventory of oceanic CO_2 was estimated using long-term time-series data on dissolved inorganic carbon from 1990s (Figure. 3.1-9). The column inventory rates of oceanic CO_2 between the sea surface and 27.5 σ_θ (1,200 to 1,400 m in depth) along 137°E and 165°E are approximately 5 – 12 and 3 – 12 tC·km^{-2}·year^{-1}, respectively. The column inventory rates of oceanic CO_2 around 20 – 30°N are higher than those at 10°N and 35°N. This is caused by the transport of CO_2 from the surface to the ocean interior by water masses known as North Pacific subtropical mode water and North Pacific intermediate water.

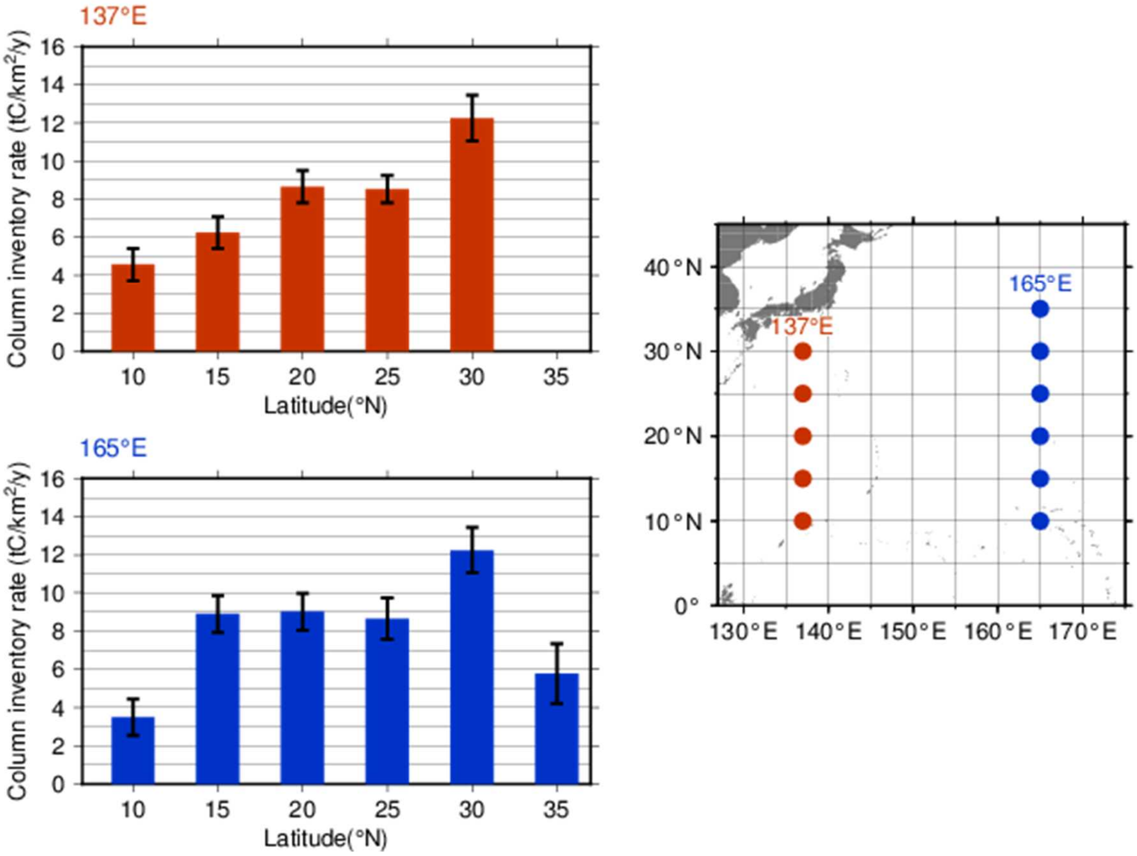

Figure 3.1-9 Changes in oceanic CO_2 between the sea surface and 27.5 σ_θ (approx. 1,200 – 1,400 m in depth) along 137 and 165°E for the periods 1994 – 2020 and 1992 – 2020.

Error bars denote a 95% confidence level

(4) Ocean acidification

The ocean acts as a large sink for CO_2 emitted as a result of human activity, and the chemical properties of seawater have changed due to the uptake and reserve of anthropogenic CO_2. Ocean acidification, known as the decrease in seawater pH (hydrogen ion exponents), is a particular issue of concern because it accelerates global warming by limiting the ocean's capacity of CO_2 uptake from the atmosphere and affects marine ecosystems by disturbing plankton growth. The IPCC AR5 (2013) included an estimate that the average global surface seawater pH has decreased by 0.1 due to ocean uptake of atmospheric CO_2 emitted as a result of human activity since the beginning of the industrial era (1750). According to numerical model experiments based on future CO_2 emission estimates, surface seawater pH will further decease by 0.065 – 0.31 by the end of 21st century. The CO_2 absorbed by the ocean is considered to have been transported into the ocean interior through ocean circulation and biological processes, and to be causing ocean acidification in the interior as well as in the surface layer (Doney et al., 2009).

JMA has long conducted oceanographic observations in the western North Pacific to monitor long-term variability relating to the ocean, such as global warming and ocean acidification. The Agency monitor long-term trends in surface and interior seawater pH along repeat hydrographic lines at 137°E and 165°E, and performs analysis to determine the average decrease in surface seawater pH throughout the Pacific using data on oceanic CO_2 concentration and related factors. The results clearly show a decreasing trend in surface seawater pH for the whole Pacific, and 0.014 to 0.021 and 0.014 to 0.029 per decade at individual stations on the 137°E and 165°E lines, respectively (Figures 3.1-10 and 3.1-11). Ocean interior pH along these lines also shows decreasing trends of 0.009 to 0.034 per decade (Figure 3.1-12) with higher rates in the northern than the southern subtropics due to greater accumulation of anthropogenic CO_2 in the former.

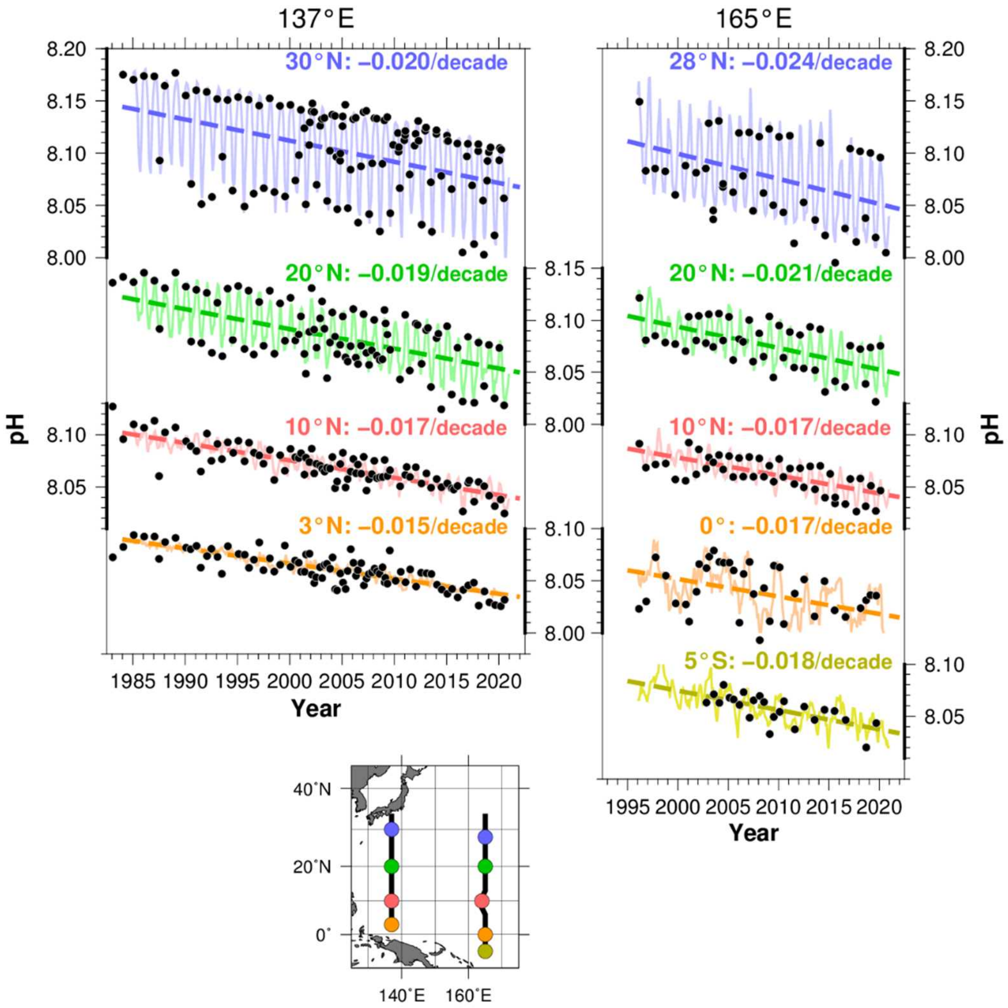

Figure 3.1-10 Long-term trends of pH at each latitude in JMA's repeat hydrographic lines at 137°E (left) and 165°E (right).

Black plots show pH observation values based on pCO_2 observation data. Solid lines represent monthly pH values reconstructed using the method of Ishii et al. (2011), dashed lines show the long-term trend of pH, and numbers indicate rates of change at each latitude.

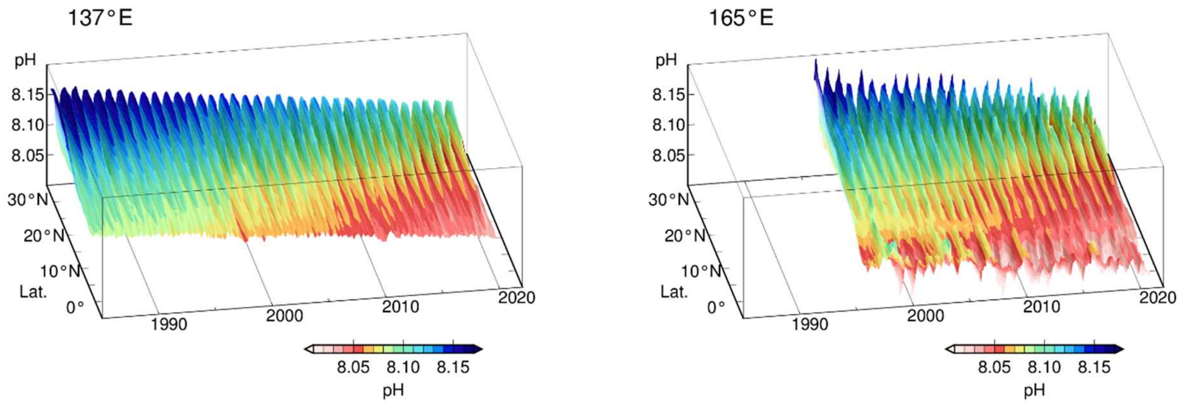

Figure 3.1-11 Time-latitude distribution of pH along the 137°E (left) and the 165°E (right) lines.

Colors indicate reconstructed monthly pH values. The part on the left shows pH along 137°E (3-34°N) since 1985, and the part on the right shows pH along 165°E (5°S-35°N) since 1996.

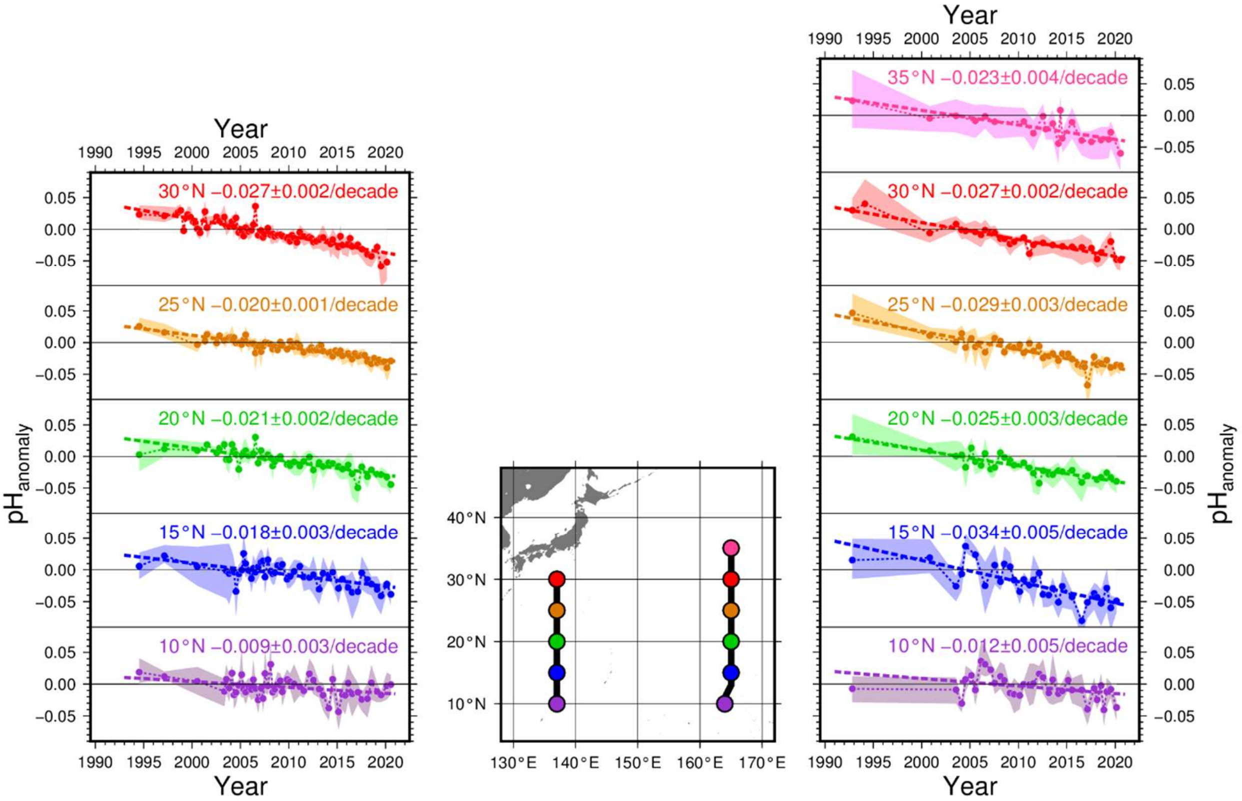

Figure 3.1-12 Long-term trends of pH between 25.0 σ_θ and 26.9 σ_θ (a depth range of about 150~800 m) along 137°E (left) and 165°E (right).

Plots show pH anomalies from averages for the whole period on the isopycnals at each latitude. The shaded areas and bold dotted lines represent the standard deviation range (±1 σ) and the long-term trend, respectively. The numbers indicate rates of change at each latitude.

(5) Concentration of carbon dioxide in the upper air

Since 2011, JMA has monitored upper-air CO_2 concentrations using cargo aircraft with support from Japan Ministry of Defense, with air samples taken along the route from Atsugi Air Base (35.45°N, 139.45°E) to Minamitorishima Island (24.29°N, 153.98°E) during level flight at an altitude of approximately 6 km and during descent[32] to the island once a month (Tsuboi *et al*., 2013; Niwa *et al*., 2014).

Figure 3-1.13 shows measured and averaged concentrations for samples collected during level flight in black and blue dots, respectively. Monthly mean concentrations at the ground-based station on the island are also shown in red. The dashed curves in blue and red represent components after removal of seasonal cycles for aircraft and Minamitorishima, respectively. Concentrations exhibit a gradual increase over time in the upper air as well as on the surface, although values tend to be lower in the former.

Figure 3-1.14 shows the vertical dependence of average seasonal cycles based on air samples collected during descent in addition to level-flight data and ground-based data. To allow direct comparison, these monthly values are calculated by averaging concentrations after removal of long-term trends in surface observation data. At each level, the information shows similar seasonal variations with higher values from winter to spring and lower values from summer to fall, while significant vertical dependence with lower values toward higher altitudes is observed from winter to spring. Consequently, the amplitude of seasonal cycles is smaller in the upper air.

Figure 3-1.15 shows concentrations for samples taken during descent minus the daily mean value recorded at the ground-based station on the flight date for February (left) and August (right).

---

[32] Although some air samples are taken during ascent flights from Minamitorishima Island, all vertical samplings are referred to here as descent samplings.

While concentrations are lower toward higher altitudes in February, there is no clear vertical dependence in August.

The above results suggest that parts of surface air affected by the terrestrial biosphere in continental regions are transported to the ground and upper levels of the island, and that air transport behavior varies with seasons and altitudes. The characteristic of strong vertical dependence from winter to spring and weak dependence from summer to fall is also identified in data from other aircraft observations around North America and Asia (Sweeney *et al*., 2015; Umezawa *et al*., 2018).

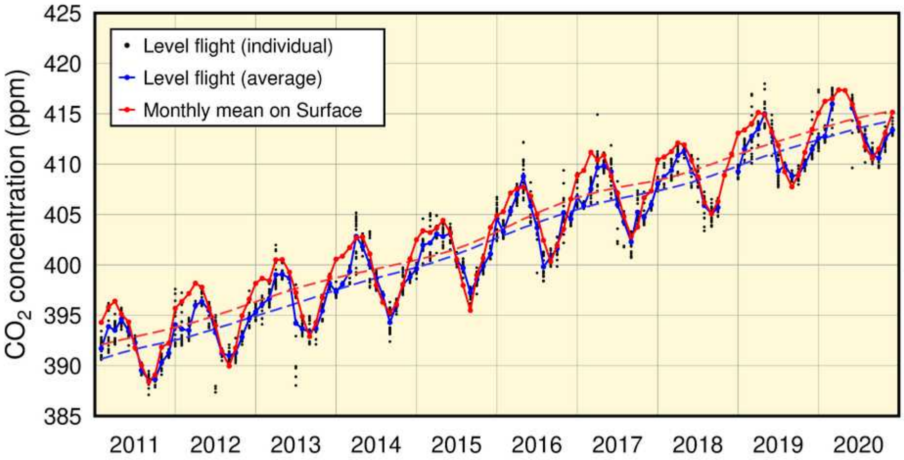

Figure 3.1-13 Measured and averaged CO_2 concentrations for air samples collected during level flight (at a height of approx. 6 km) of cargo aircraft along the route from Atsugi Air Base to Minamitorishima (black and blue dots, respectively) and monthly mean concentrations at the Minamitorishima ground-based station (red dots).

Blue and red dashed lines represent components after the removal of seasonal cycles from the series of blue and red dots, respectively. The analysis is based on WMO (2009).

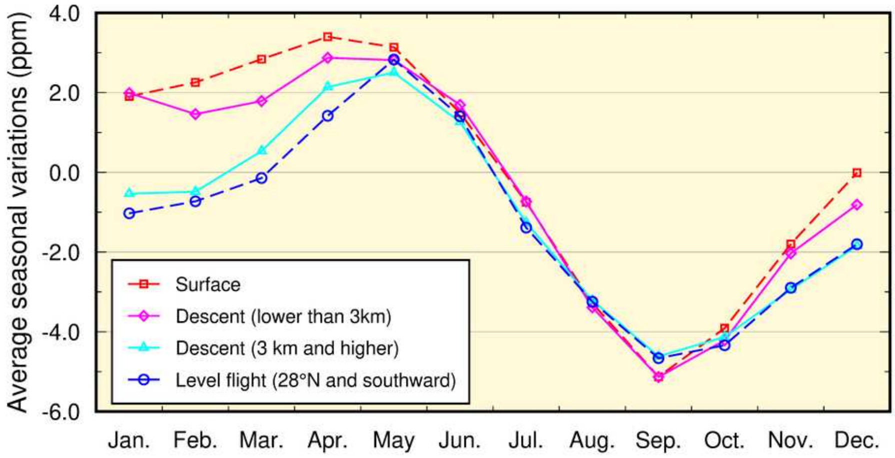

Figure 3.1-14 Vertical dependence of average seasonal cycles around Minamitorishima for monthly mean concentrations on the surface (red), concentrations for air samples taken during level flight at latitudes 28°N and southward (blue), and those taken during descent with altitudes less than 3 km (magenta) and otherwise (cyan).

Monthly values are calculated by averaging concentrations after removal of long-term trends (components without seasonal cycles) for surface observation data (the red dashed line in Figure 3.1-13).

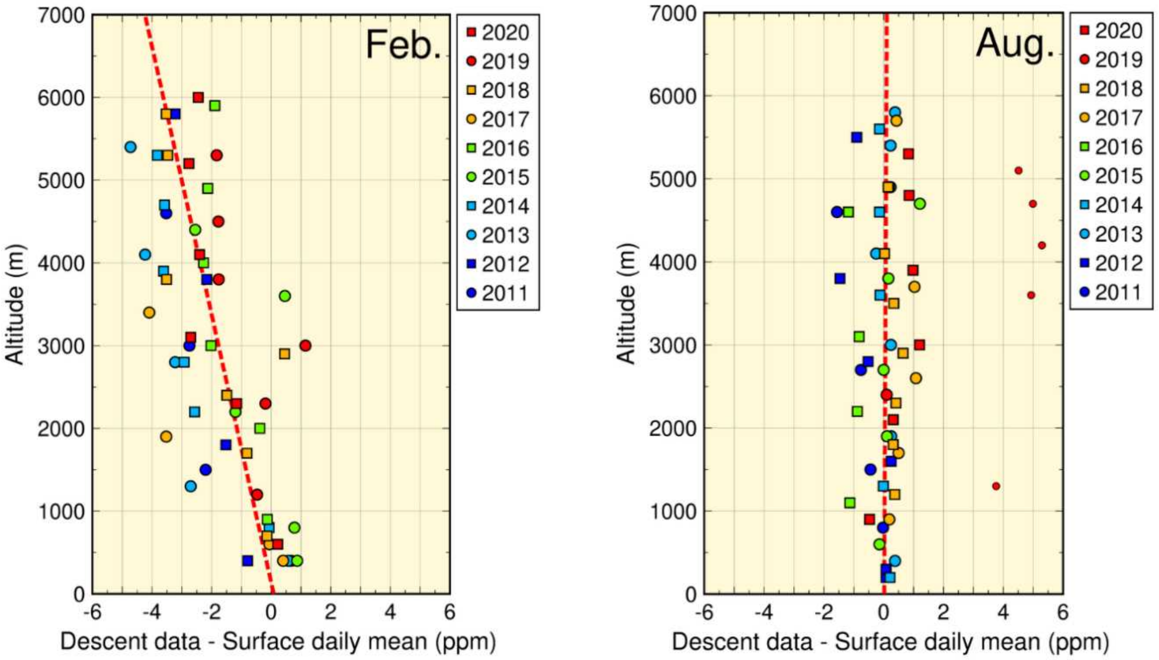

Figure 3.1-15 Vertical variations of CO_2 concentrations over Minamitorishima

Circles and squares show concentrations of air samples taken during descent to the island minus the daily mean value recorded at the ground-based station on the flight date. Symbol colors and shapes represent observation years. Dashed red lines show the vertical gradient of the symbols as determined using the least squares method. To determine representative characteristics for the observation area, outlier data (small symbols) beyond the 3 sigma of the residual standard deviation from the fitted line are excluded from calculation for the vertical gradient. On the flight date in August 2019, daily mean concentration on the surface was 4 – 5 ppm lower than that during descent because continental air masses with low CO_2 concentrations were transported to areas near the ground around Minamitorishima.

3.1.2 Concentration of methane

(1) Concentration of global atmospheric methane

The global mean concentration of atmospheric CH_4 has been increasing since at least the mid-1980s when worldwide monitoring began, except for a stationary phase from 1999 to 2006 (Figure 3.1-16). The mechanism behind the stationary phase remains unclear, but several scenarios have been proposed (IPCC, 2013). The greater concentrations observed since 2007 indicate an increase in CH_4 emissions from tropical wetlands and human activity in the mid-latitudes of the Northern Hemisphere (WMO, 2020).

WDCGG analysis shows that the global mean concentration of CH_4 in 2019 was 1,877 ppb, which is the highest since records began (Table 3.1-1).

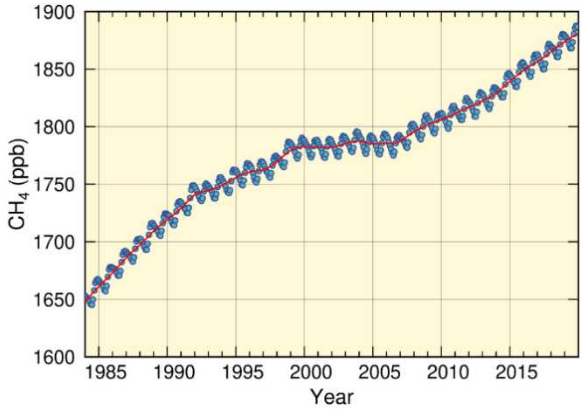

Figure 3.1-16 Global mean concentration of atmospheric CH_4

The blue dots are monthly values, and the red line represents the corresponding sequence after the removal of seasonal variations. Graph content is based on analysis of observation data reported to WDCGG based on the method of WMO (2009). Data contributors are listed in WMO (2021).

Figure 3.1-17 shows the latitudinal dependence of CH_4 concentrations. Values are lower in the tropics than in the high and mid-latitudes of the Northern Hemisphere because CH_4 is mostly emitted from land areas in the Northern Hemisphere, and disappears due to reaction with hydroxyl radicals[33] over tropical oceans during transportation to the Southern Hemisphere. In summer, more CH_4 is destroyed because more hydroxyl radicals are produced as a result of enhanced ultraviolet radiation and water vapor. This reaction contributes to seasonal variations of CH_4 concentrations in both hemispheres, with lower values in summer and higher values in winter (Figures 3.1-16 and 3.1-17).

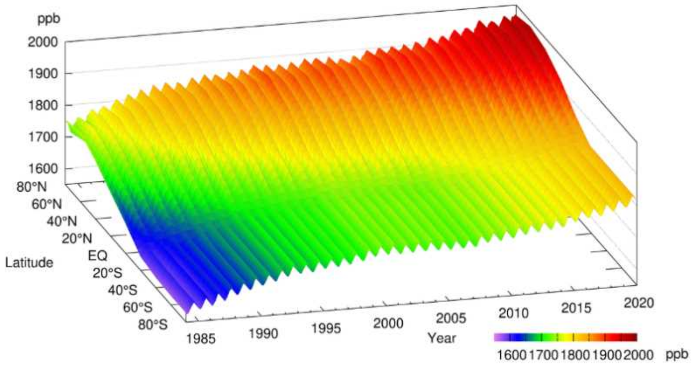

Figure 3.1-17
Latitudinal distribution of atmospheric CH_4 concentrations

The data set and analysis method are as per Figure 3.1-16.

---

[33] Hydroxyl radicals are highly reactive chemicals generated by the reaction of atomic oxygen, which is derived from UV photolysis of ozone, with airborne water vapor. It is particularly abundant at low latitudes, where UV radiation is strong and water vapor is plentiful.

The remarkable increase observed in global mean atmospheric concentrations of CH_4 since the industrial era (+160%) has been much more rapid than that of CO_2 (+48%) (Table 3.1-1). This is partly because the amount of anthropogenic emissions of CH_4 relative to natural emissions exceeds that of CO_2. The long-term trend of CH_4 concentration depends on various factors of uncertainty, including anthropogenic/natural emissions and chemical reactions. Accordingly, further development of the global CH_4 observation network is required.

(2) Concentration of atmospheric methane in Japan

Atmospheric CH_4 concentrations at all of Japan's three observation stations exhibit a trend of increase with seasonal variations in the same way as the global mean concentration (Figure 3.1-18 (a)). Ryori usually observes the highest concentration among the three stations because it is located in the northern part of Japan, where CH_4 sources in the Asian continent are more influential and reaction with hydroxyl radicals is less marked. Although Yonagunijima and Minamitorishima are located at similar latitudes, the former tends to record higher concentrations in winter because CH_4 sources on the Asian continent have a stronger impact there in winter as a result of continental air mass expansion. In summer, meanwhile, a hydroxyl radical-rich maritime air mass covers both stations, and similarly low concentrations are observed. Since 2010, Yonagunijima has occasionally observed concentrations as high as those of Ryori in winter. The annual mean CH_4 concentration in 2020 was 1,967 ppb at Ryori, 1,912 ppb at Minamitorishima and 1,937 ppb at Yonagunijima, all of which are the highest on record (based on preliminary estimations).

The growth rate of atmospheric CH_4 concentration exhibits interannual variations that differ significantly from station to station (Figure 3.1-18 (b)).

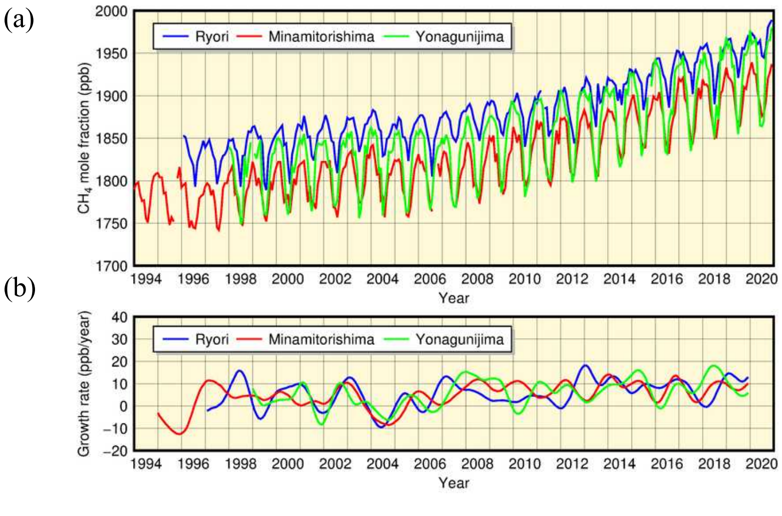

Figure 3.1-18
Monthly mean concentrations (a) and corresponding growth rates (b) of atmospheric CH_4 observed at Ryori (blue), Minamitorishima (red) and Yonagunijima (green)

The method for calculating the growth rate is described in WMO (2009).

3.1.3 Concentration of nitrous oxide

Figure 3.1-19 shows that the global mean concentration of atmospheric N_2O has been continuously increasing. The annual mean concentration in 2019 was 332.0 ppb, which was 23% above the pre-industrial level of 270 ppb (Table 3.1-1). Seasonal variations of N_2O concentrations are lower than those of CO_2 and CH_4 because N_2O has a longer lifetime (121 years). The hemispheric mean concentration is approximately 1 ppb higher in the Northern Hemisphere than in the Southern Hemisphere (Figure 3.1-20) because there are more sources of anthropogenic emissions in the former. This interhemispheric difference is, however, much smaller than those observed with CO_2 and CH_4.

The atmospheric N_2O concentration at Ryori exhibits characteristics similar to those of the global mean (Figure 3.1-21). The annual mean concentration in 2020 at Ryori was 335.5 ppb (based on preliminary estimations).

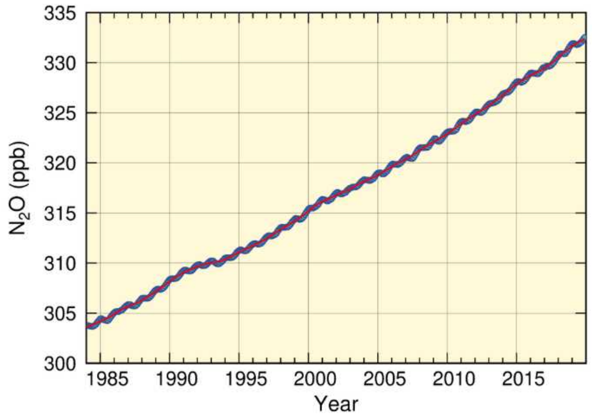

Figure 3.1-19 Global mean concentration of atmospheric N_2O
The blue dots are monthly values, and the red line represents the corresponding sequence after the removal of seasonal variations. Graph content is based on analysis of observation data reported to WDCGG based on the method of WMO (2009). Data contributors are listed in WMO (2021).

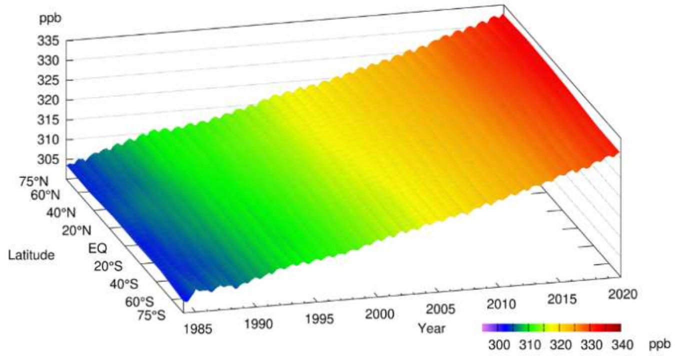

Figure 3.1-20 Latitudinal distribution of atmospheric N_2O concentrations
The data set and analysis method are as per Figure 3.1-19.

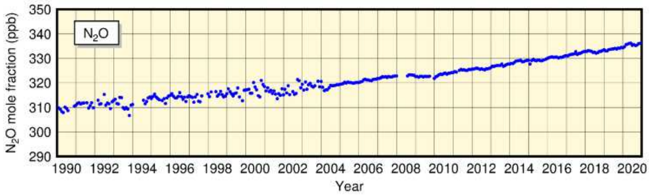

Figure 3.1-21
Monthly mean concentrations of atmospheric N_2O at Ryori
Improvement of observation equipment in 2004 resulted in improved stability of measurements.

3.1.4 Concentration of halocarbons

Halocarbons are generally carbon compounds containing halogens such as chlorine and bromine, many of which are powerful greenhouse gases whose atmospheric concentrations have increased rapidly since the second half of the 20th century due to artificial production. Although their atmospheric concentrations are only around a millionth those of CO_2, their greenhouse effect per unit mass is several thousand times greater.

Chlorofluorocarbons (CFCs: CFC-11, CFC-12 and CFC-113), which are compounds of carbon, fluorine and chlorine, and other halogenated gases are ozone-depleting substances (ODSs). They are regulated under the 1987 Montreal Protocol on Substances that Deplete the Ozone Layer and its Amendments and Adjustments.

Hydrofluorocarbons (a halocarbon variety consisting of carbon compounds containing fluorine and hydrogen, referred to here as HFCs) have no effects on stratospheric ozone depletion and have been used as substitutes for CFCs. However, the Kigali Amendment of 2016 added HFCs to the list of substances subject to regulation under the Montreal Protocol (effective as of 2019) due to their significant greenhouse effects.

(1) Global concentration of halocarbons

Global concentrations of atmospheric CFCs increased rapidly until the 1980s before entering a decreasing trend in the 1990s (Figure 3.1-22). The concentration of CFC-11 peaked in 1992 – 1994, and has since shown a decreasing tendency. The concentration of CFC-12 increased until around 2003, and has also since shown a decreasing tendency. The concentration of CFC-113 reached its maximum in around 1993 in the Northern Hemisphere and around 1996 in the Southern Hemisphere. Differences in the concentrations of these gases between the Northern Hemisphere, where most emissions sources are located, and the Southern Hemisphere, which has significantly fewer sources, have decreased since the 1990s in contrast to the situation of the 1980s. These observations indicate that the CFC emission controls under the Montreal Protocol have been effective.

However, a slowdown in the decline of CFC-11 concentrations has been observed since 2012 (WMO, 2018a; WMO, 2018b; Montzka *et al*., 2018; Rigby et al., 2019), with decreasing rate approximately two thirds of those seen in the preceding decade. Numerical model calculation reporting by Montzka *et al*. (2018) attributed this to increased global CFC-11 emissions with main sources probably located in eastern Asia.

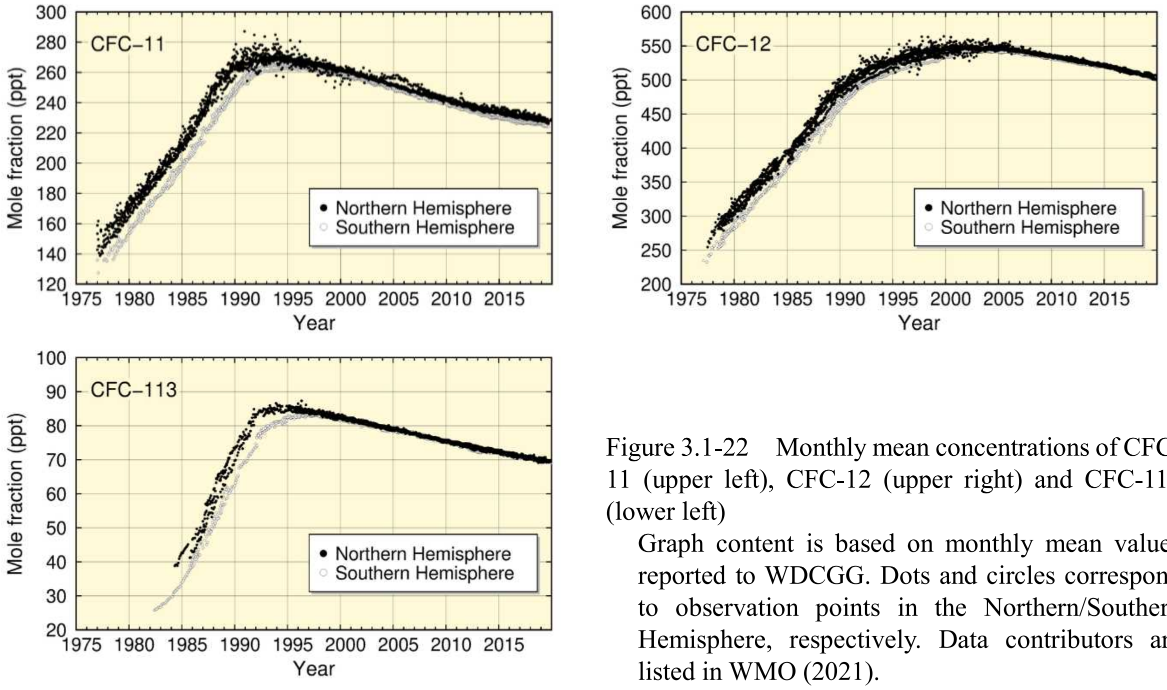

Figure 3.1-22 Monthly mean concentrations of CFC-11 (upper left), CFC-12 (upper right) and CFC-113 (lower left)

Graph content is based on monthly mean values reported to WDCGG. Dots and circles correspond to observation points in the Northern/Southern Hemisphere, respectively. Data contributors are listed in WMO (2021).

As with CFCs, atmospheric concentrations of HFCs are higher in the Northern Hemisphere, where there are more emissions sources than in the Southern Hemisphere (Figure 3.1-23). Atmospheric concentrations of HFC-134a continue to increase, while those of HFC-152a have levelled off in recent years. Atmospheric concentrations of HFC-152a show remarkable seasonal variations.

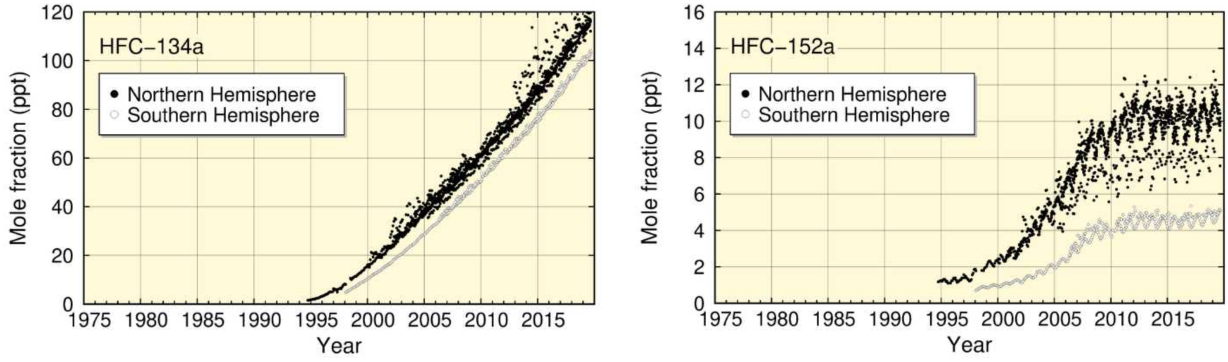

Figure 3.1-23 Monthly mean concentrations of HFC-134a (left) and HFC-152a (right)

The dataset and analysis method are as per Figure 3.1-22.

(2) Concentrations of halocarbons in Japan

Concentrations of CFC-11, CFC-12 and CFC-113 at Ryori have shown decreasing tendencies since reaching maxima in various years (Figure 3.1-24). The concentration of CFC-11 peaked at about 270 ppt in 1993 – 1994, and has since decreased. The distinct peak of concentration observed in 2011 is considered attributable to emissions from polyurethane foam insulation materials released by the Great East Japan Earthquake and the subsequent hugely destructive tsunami of 11 March 2011 (Saito *et al.*, 2015). The rate of increase in CFC-12 concentration slowed around 1995, and a gradual decrease has been seen since 2005. There was no clear tendency of increase or decrease in the concentration of CFC-113 until 2001, but a decreasing tendency has been seen since then.

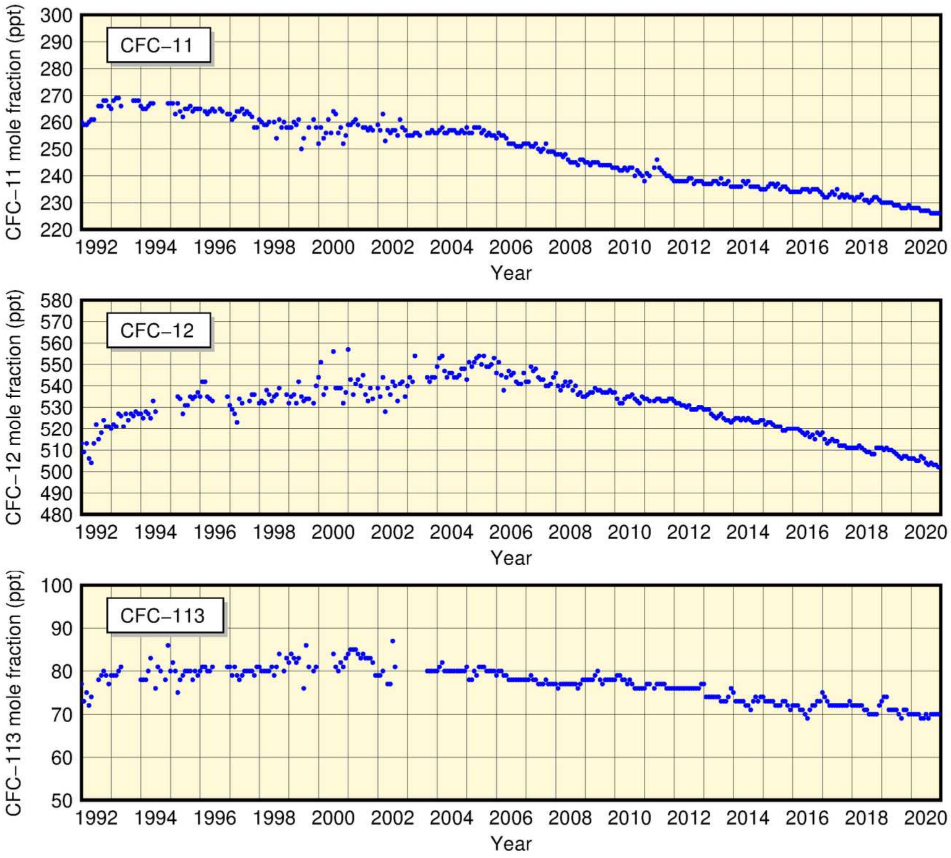

Figure 3.1-24 Monthly mean atmospheric concentrations of CFC-11 (top), CFC-12 (middle) and CFC-113 (bottom) at Ryori

Improvement of observation equipment in 2003 resulted in improved stability of measurements.

The Japan Meteorological Agency began observing atmospheric HFC concentrations at Minamitorishima in April 2020. The results show that values for HFC-134a and HFC-152a are similar to those at other observation sites in the Northern Hemisphere in the context of global observation (Figure 3.1-25). Against this background, ongoing long-term monitoring is considered important.

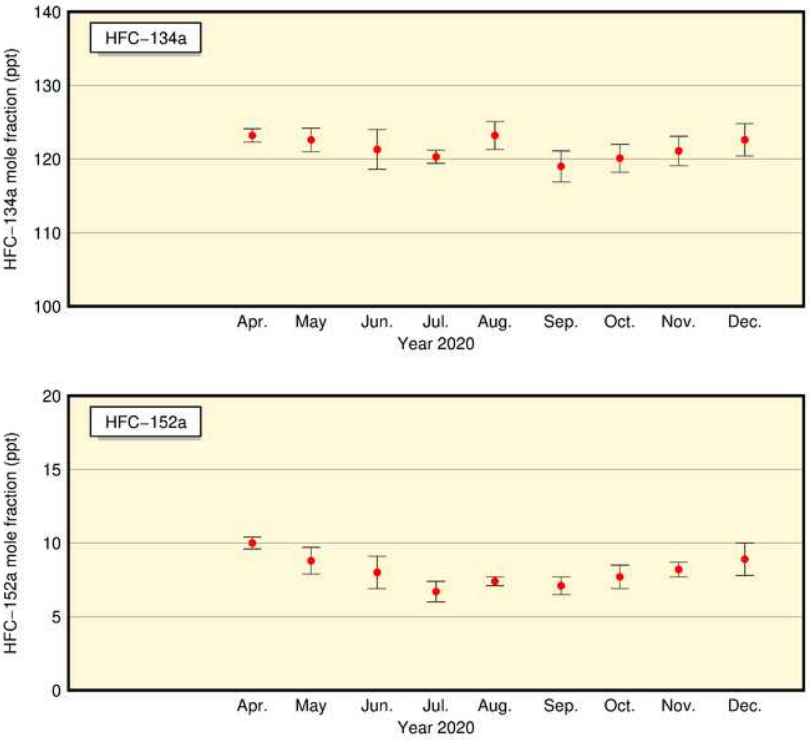

Figure 3.1-25 Monthly mean atmospheric concentrations of HFC-134a (top) and HFC-152a (bottom) at Minamitorishima

Observation of atmospheric HFC concentrations was started in April 2020 at Minamitorishima.

3.2 Monitoring of aerosols and surface radiation[34]

○ In Japan, background atmospheric turbidity coefficient values (which depend on concentrations of aerosols, water vapor and other constituents in the air) have returned to approximate levels seen before the eruption of Mt. Agung in 1963. This is mainly because of no large-scale eruptions impacting the global climate since that of Mt. Pinatubo in 1991.

○ The number of days when any meteorological station in Japan observed Kosa was 5 in 2020, and the total number of stations reporting its occurrence during the year was 10.

3.2.1 Aerosols

Interannual variations in the atmospheric turbidity coefficient[35], which is calculated from direct solar radiation[36] measurements taken at five stations in Japan excluding the fluctuation component of the troposphere, shows a clear impacts of stratospheric aerosols resulting from volcanic eruptions (Figure 3.2-1). The increased turbidity coefficients observed for several years after 1963 and during the periods of 1982 – 1983 and 1991 – 1993 were caused by the eruptions of Mt. Agung (Indonesia) in 1963, Mt. El Chichón (Mexico) in 1982 and Mt. Pinatubo (Philippines) in 1991, respectively. The increased turbidity stems from the persistent presence of sulfate aerosol in the stratosphere resulting from huge amounts of SO_2 released by the volcanic eruptions. The turbidity coefficient has now returned to approximately the same level as that observed before the eruption of Mt. Agung because no large-scale eruptions have occurred since that of Mt. Pinatubo.

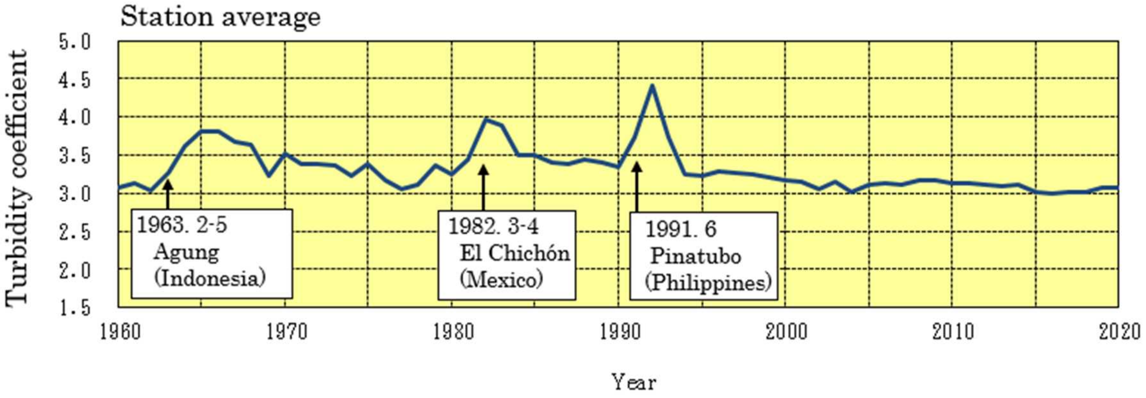

Figure 3.2-1 Time-series representation of annual mean atmospheric turbidity coefficients (1960 – 2020)
To eliminate the influence of variations in tropospheric aerosols such as water vapor, dust and air pollutants, the annual mean atmospheric turbidity coefficient is calculated using the minimum turbidity coefficient for each month. Arrows indicate significant volcanic eruptions.

---

[34] See the Glossary for terms relating to aerosols.
Information on surface radiation and Kosa is published on JMA's website.
https://www.data.jma.go.jp/gmd/env/kosahp/en/kosa.html (Aeolian Dust (Kosa))
https://www.data.jma.go.jp/gmd/env/radiation/en/info_rad_e.html (Solar and Infrared Radiation)

[35] The atmospheric turbidity coefficient indicates the ratio of the atmospheric optical depth affected by aerosols, water vapor and gases in the atmosphere to that uninfluenced by constituents other than air molecules such as oxygen and nitrogen in the atmosphere. Larger values indicate greater amounts of turbid matter in the air.

[36] Direct solar radiation is the incident solar energy acting on the earth's surface from the sun. The atmospheric turbidity coefficient (also known as the Feussner-Dubois turbidity coefficient) can be calculated from direct solar radiation amounts.

3.2.2 *Kosa (Aeolian dust)*

Kosa (Aeolian dust) is a kind of aerosol blown up from semi-arid areas of the Asian continent and transported by westerly winds to Japan. A total of 11 JMA meteorological stations (as of 31 December 2020) perform Kosa monitoring. The phenomenon is recorded when visually observed by station staff. The number of days when any meteorological station in Japan observed Kosa was 5 in 2020 (Figure 3.2-2), and the total number of stations reporting its occurrence during the year was 10 (Figure 3.2-3).

The number of days on which Kosa is observed shows no discernible trend, but the annual total number of stations reporting observation is very likely to have increased (statistically significant at a confidence level of 90%.) An increased trend in the annual total number of stations is reflected in the rich body of observation data for the 2000 – 2010 period. As the phenomenon shows significant interannual variability, ongoing data collection is necessary to clarify related trends.

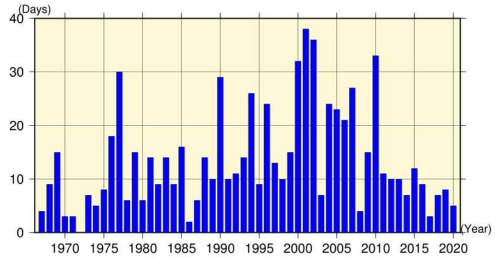

Figure 3.2-2 Number of days when any station in Japan observed Kosa (1967 – 2020) based on the 11 stations that were active for the whole period

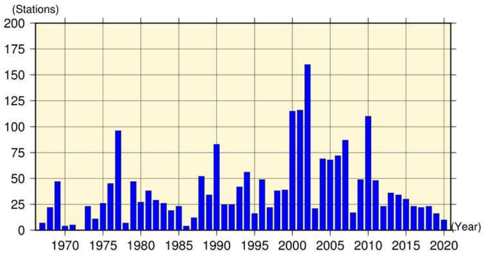

Figure 3.2-3 Annual total number of stations observing Kosa in Japan (1967 – 2020) based on the 11 stations that were active for the whole period

3.2.3 *Solar radiation and downward infrared radiation*

The earth's radiation budget is a source of energy for climate change, and monitoring of its variations is important. To this end, JMA conducts measurements of direct solar radiation, diffuse solar radiation and downward infrared radiation[37] at five stations in Japan (Sapporo, Tsukuba, Fukuoka, Ishigakijima and Minamitorishima) (Figure 3.2-4).

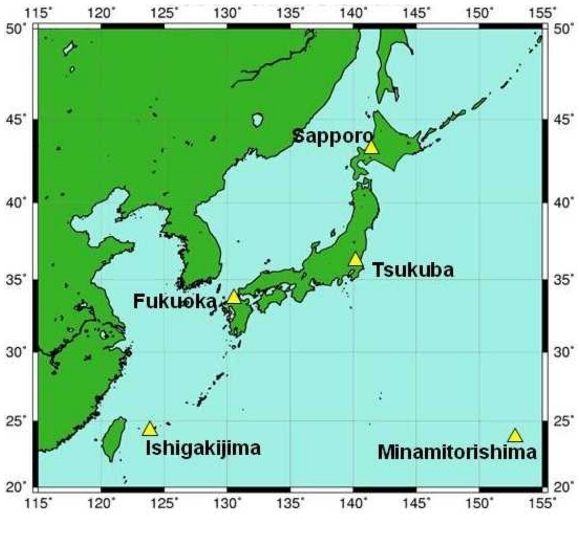

Figure 3.2-4 JMA's solar radiation and infrared radiation observation network

JMA conducts observation of direct solar, diffuse solar and downward infrared radiation at five stations (Sapporo, Tsukuba, Fukuoka, Ishigakijima and Minamitorishima).

---

[37] Downward infrared radiation is the incident infrared radiation acting on the earth's surface from all directions in the sky. It is emitted from clouds and atmospheric constituents such as water vapor and carbon dioxide in proportion to the fourth power of their temperature, and can be used as an index of global warming.

(1) Global solar radiation

Reports indicate that global solar radiation decreased from around 1960 to the late 1980s before increasing rapidly from the late 1980s to around 2000, and no obvious changes have been observed in most regions of the world (Ohmura, 2009).In Japan, global solar radiation declined rapidly from the late 1970s to around 1990 before increasing rapidly from around 1990 to the early 2000s. Since then, data from measurements at the five observation stations show no obvious changes. These long-term variations are consistent with those reported globally (Figure 3.2-5).

Variations are considered to stem mainly from changes in anthropogenic aerosols in the atmosphere, and to be partly attributed to changes in cloud cover and cloud characteristics (Wild, 2009). Norris and Wild (2009) quantitatively estimated the cause of the rapid increase in global solar radiation observed in Japan from around 1990 to the beginning of the 2000s. According to their estimates, two thirds of the increase was due to reduced anthropogenic aerosols in the atmosphere and the other third was due to reduced cloud cover. These results imply that the presence of anthropogenic aerosols has a profound effect on solar radiation variations. Results produced by Kudo et al. (2012) indicated that the solar radiation increase was mainly caused by changes in the optical characteristics of aerosols due to changes in the aerosol composition of the atmosphere.

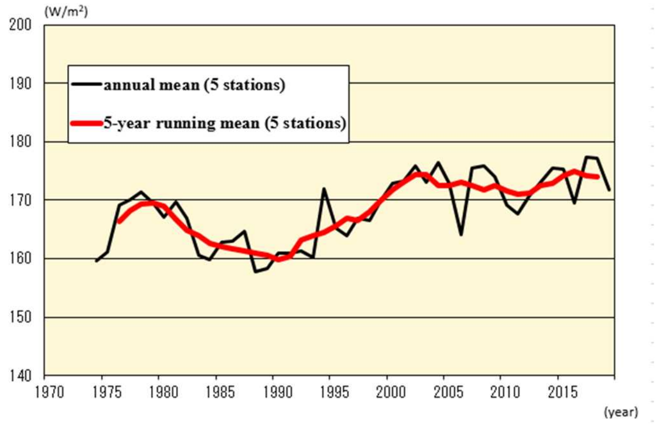

Figure 3.2-5 Time-series representations of annual (black line) and five-year-running (red line) means of global solar radiation at five stations in Japan (Sapporo, Tsukuba, Fukuoka, Ishigakijima and Minamitorishima)
Annual means are based only on monthly mean calculation from more 20 daily datasets. Before March 2010 (and before December 1987 at Tsukuba), observation was global pyranometer-based, while values have since been derived from the sum of direct and diffused pyranometer observations. In 2019 the Sapporo annual mean did not include September data due to instrument issues, and in 2020 could not be calculated because instrument relocation resulted in a lack of data for November and December. The 2018 running mean for Sapporo is created with the means from 2016 to 2019. Calculation of the 2020 annual mean and the 2018 running mean will be based on old- and new-station data.

(2) Downward infrared radiation

Atmospheric concentrations of carbon dioxide and other greenhouse gases, which cause global warming, show increasing yearly trends. Observation of downward infrared radiation is effective for the evaluation of global warming because signals of global warming due to increased greenhouse gases are seen more clearly from increased downward infrared radiation than from increased surface temperatures. While general circulation model experiments suggest that two decades of downward infrared radiation monitoring are necessary to detect statistically significant increases with a confidence level of 95%, analysis of in situ observation data covering about a decade has shown an overall increase (Wild and Ohmura, 2004).

In Japan, downward infrared radiation has been monitored since the early 1990s at Tsukuba.

Analysis of the data obtained shows an increasing trend at a rate of about 0.3 W/m^2 per year during the period from 1993 to 2020 (Figure 3.2-6). This is consistent with the trend seen in the results of analysis using data from 20 BSRN[38] stations worldwide (+0.3 W/m^2 per year during the period from 1992 to 2009) (WCRP, 2010).

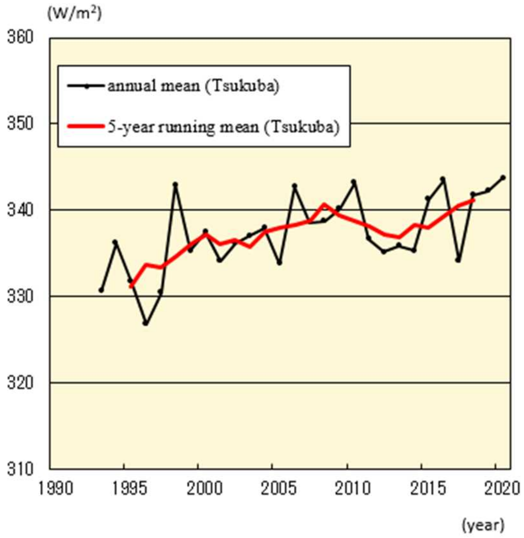

Figure 3.2-6 Time-series representations of annual (black line) and five-year-running (red line) means of downward infrared radiation at Tsukuba

---

[38] The BSRN (Baseline Surface Radiation Network) is a global observation network for measuring high-precision surface radiation balance on an ongoing basis. JMA operates five BSRN stations in Japan (Sapporo, Tsukuba, Fukuoka, Ishigakijima and Minamitorishima) and one in Antarctica (Syowa Station).

Explanatory note on detection of statistical significance in long-term trends

Meteorological observation data, including those relating to temperature and precipitation, are subject to large amplitude fluctuations due to the influence of atmospheric and oceanic dynamics on a broad spectrum of spatial and temporal scales. To examine the possible presence of long-term climate system trends associated with global warming in consideration of natural variability, raw climate data need to be converted into suitable statistical time-series representations and subjected to statistical testing in order to highlight the likelihood of systematic temporal trends that cannot be explained by random variability alone. When the results of such testing allow reasonable conclusion that random variability is unlikely to be the sole factor at work, a change is described as statistically significant.

In this report, the likelihood of a systematic long-term change existing in a time-series representation is based on the results of statistical significance testing performed at confidence levels of 99, 95 and 90%. The following terminology summary describes each level:

Level of confidence	Term
≥ 99%	**Virtually certain** to have increased/decreased (statistically significant at a confidence level of 99%)
≥ 95%	**Extremely likely** to have increased/decreased (statistically significant at a confidence level of 95%)
≥ 90%	**Very likely** to have increased/decreased (statistically significant at a confidence level of 90%)
< 90%	No discernible trend

The following statistical methods are applied for the data used in this report:

i) For statistical variables whose annual fluctuation component can be assumed to follow normal distribution

For temperature anomalies, trend-removed annual variability data are expected to approximately follow normal distribution. T-testing is performed for statistical variables assumed to be normally distributed using a coefficient of correlation between years and values.

ii) For statistical variables whose annual fluctuation component cannot be assumed to follow normal distribution

The assumption of normality may not be applicable to frequency statistics regarding weather conditions, including those for extremely warm days, tropical nights and hourly precipitation amounts exceeding 50 mm. Accordingly, non-parametric testing, which does not depend on underlying assumptions about distribution, is applied to such variables.

It should be noted that statistical tests are in theory inevitably susceptible to the establishment of false conclusions even if the results indicate a statistically significant trend. Even outcomes indicating statistical significance at confidence levels of 90, 95 or 99% imply that there are small inherent probabilities of up to 10, 5 and 1%, respectively, of the significance being erroneously detected when in fact the observed long-term change occurred by mere random chance. Conversely, when a systematic long-term change actually exists, statistical testing may fail to detect the significance correctly. In general, test results are not considered highly stable if they are based on observation records that are temporally limited, influenced by large annual fluctuations/rare events or subject to change when new observations are added to a data sequence. Readers are encouraged to interpret the analytical results presented in the report appropriately with due note of these considerations.

Glossary

Aerosols

Aerosols are airborne solids or liquids in fine particle form. Their many types include particles of natural origin blown up from land/sea surfaces, anthropogenic particles and secondary aerosols formed from anthropogenic and biogenic precursors. In addition to absorbing and scattering sunlight, they also provide condensation nuclei for clouds. Particulate matter 2.5 (PM2.5) is the name given to aerosol particles measuring 2.5 micrometers or less in diameter (about 30 times thinner than a human hair), and is considered to have possible adverse effects on human health when inhaled.

Anthropogenic

Resulting from or produced by human activity.

Arctic Oscillation

The Arctic Oscillation (AO) is a major atmospheric circulation variation exhibiting an annular pattern of sea-level pressure anomalies in a seesaw fashion with one sign over the Arctic region and the opposite sign over the mid-latitudes. Its negative phase, which is characterized by positive and negative sea-level pressure anomalies over the Arctic region and the mid-latitudes, respectively, helps cold Arctic air move into the mid-latitudes. The positive phase, whose sea-level pressure anomaly pattern is reversed, keeps Arctic air over the Arctic region.

Extreme climate event

In general, an extreme climate event is recognized as an unusually severe or rare climate event creating disaster conditions or exerting significant socio-economic influence. The definition includes severe weather conditions covering periods ranging from only a few hours (such as heavy rain or strong wind) to several months (such as drought or cold summer conditions). JMA defines extreme climate events as those occurring once every 30 years or longer.

IPCC (Intergovernmental Panel on Climate Change)

The Intergovernmental Panel on Climate Change (IPCC) is an international organization established by the United Nations Environment Programme (UNEP) and the World Meteorological Organization (WMO) in 1988. It reviews and assesses scientific, technical and socio-economic information on climate change, the potential impacts of such change and related vulnerability, and options for adaptation and mitigation, in collaboration with scientists and experts on an international basis. The Panel's reports highlight common understanding of such information to support political matters such as treaty negotiations on global warming.

Kosa (Aeolian dust)

Kosa (Aeolian dust) is a meteorological phenomenon in which fine dust is blown up to an altitude of several thousand meters by cyclonic or other wind systems from deserts or cropland in semi-arid areas of the Asian continent, and is transported over long distances by westerly winds, resulting in haze or dustfall in downstream areas. It is often observed between March and June in Japan and makes the sky yellow and hazy. Heavy Kosa can affect transportation by obstructing visibility.

Monsoon

The term *monsoon* primarily refers to seasonally reversing winds, and by extension includes related seasonal rainfall change with wet and dry phases. Monsoon climate regions where seasonal winds prevail are found in numerous places around the world, with a major one located over a broad area from the Asian continent to northern Australia.

Normals

Normals represent climatic conditions at meteorological stations, and are used as a base to evaluate meteorological variables (e.g., temperature, precipitation and sunshine duration) and produce generalizations (e.g., cool summer, warm winter and dry/wet months) for particular periods. JMA uses averages for the most recent three decades (currently 1981 – 2010) as normals, which are updated every decade in line with WMO Technical Regulations. The most recent update took place on May 19 2021 based on observation values from 1991 to 2020.

Terms relating to surface temperature variations

El Niño/La Niña events: In an El Niño event, sea surface temperatures (SSTs) are higher than normal across a wide region from near the date line to the area off the coast of South America in the equatorial Pacific for about a year. In a La Niña event, SSTs are lower than normal in the same area. Both occur every few years, and are associated with frequent extreme climate conditions worldwide.

JMA recognizes the occurrence of an El Niño event when the five-month running mean of SST deviations from the climatological means (based on a sliding 30-year period averaged over the NINO.3 El Niño Monitoring Region (5ºN – 5ºS, 150ºW – 90ºW; Figure A)) remains +0.5°C or above for a period of six months or more. Similarly, a La Niña event is recognized when the corresponding figure is −0.5°C or below for the same area/period.

Figure B shows typical SST deviations from the normal during El Niño and La Niña events. The dark red and blue shading seen from the date line to the coast of South America indicates large deviations.

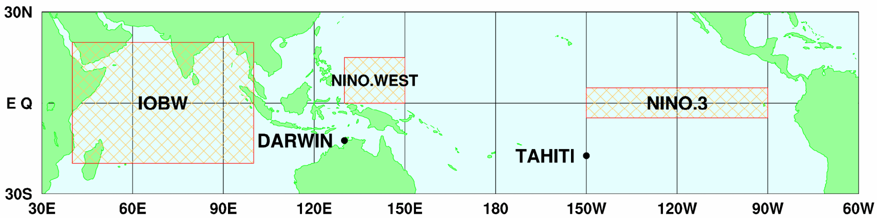

Figure A El Niño monitoring regions

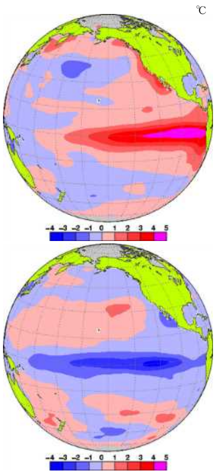

Figure B Left: monthly mean SST anomalies for El Niño (November 1997); right: for La Niña (December 1998)

Red and blue shading represents positive and negative SST deviations, respectively. Darker shading indicates larger deviations. The unit of temperature is degrees Celsius.

Southern Oscillation: El Niño and La Niña events are closely related to trade winds (easterlies blowing around the tropical Pacific), which tend to be weak during the former and strong during the latter. The strength of such winds is closely related to the sea level pressure difference between eastern and western parts of the Pacific. This pressure difference varies in a phenomenon known as the Southern Oscillation. El Niño/La Niña events and the Southern Oscillation are not independent of each other; they are different manifestations of the same phenomenon involving atmospheric and oceanic interaction, and are referred to as ENSO (El Niño – Southern Oscillation) for short.

Pacific Decadal Oscillation (PDO): A phenomenon in which variables in the atmosphere and oceans tend to co-vary with a period of more than ten years in the North Pacific. When sea surface temperatures are lower (higher) than their normals in the central part of the North Pacific, those in its part along the coast of North America are likely to be higher (lower) than their normals, and sea level pressures in the high latitudes of the North Pacific are likely to be lower (higher) than their normals. These atmospheric variations affect meteorological conditions in North America and elsewhere.

Indian Ocean Dipole mode (IOD) event: A phenomenon in which sea surface temperatures (SSTs) are below normal in the south eastern part of tropical Indian Ocean (off the Sumatra Island) and above normal in the western part during the northern hemisphere summer and autumn (June - November). This east-west contrast of SST anomaly pattern is called dipole mode. On the other hand, a phenomenon in which SSTs are above normal off the Sumatra Island and below normal in the western part is called negative IOD event. These phenomena affect the climate near Japan and Australia through the changes of atmospheric circulation caused by atmospheric active (inactive) convections over above (below) normal SST area.

Terms relating to the greenhouse effect

Greenhouse effect: The earth's atmosphere contains small amounts of greenhouse gases, which absorb a large part of the infrared radiation emitted from the earth's surface and re-emit it back, thereby warming the surface. This process is known as the greenhouse effect. Without it, the earth's average surface temperature of around 14°C would be approximately −19°C. Increased concentrations of greenhouse gases enhance the greenhouse effect, thereby producing higher surface temperatures. Major greenhouse gases include carbon dioxide, methane and nitrous oxide. Although water vapor has the strongest greenhouse effect, it is not usually regarded as a greenhouse gas in the context of global warming because the amount of water vapor on a global scale is not directly affected by human activity.

Carbon dioxide: Of all greenhouse gases, carbon dioxide (CO_2) is the most significant contributor to global warming. Since the start of the industrial era in the mid-18th century, its atmospheric concentration has increased as a result of emissions associated with human activity, such as fossil fuel combustion, cement production and deforestation. Around half of all cumulative anthropogenic CO_2 emissions have remained in the atmosphere. The rest was removed from the atmosphere and stored in natural terrestrial ecosystems and oceans (IPCC, 2013).

Methane: Methane (CH_4) is the second most significant greenhouse gas after CO_2. Around 40% of CH_4 released into the atmosphere is of natural origin (wetlands, termites, etc.), and around 60% is from human-related activity sources (ruminant animals, rice paddy fields, fossil fuel mining, landfill, biomass burning, etc.) (WMO, 2020). It is primarily removed from the atmosphere via photochemical reaction with reactive and unstable hydroxyl (OH) radicals.

Nitrous oxide: Nitrous oxide (N_2O) is a significant greenhouse gas because of its large radiative effect per unit mass (about 265 times greater than that of CO_2) and its long lifetime (about 121 years) in the atmosphere. Around 60% of N_2O released into the atmosphere is of natural origin (oceans, soil, etc.), and around 40% is from human activity-related sources (biomass burning, nitrate fertilizers, various industrial processes, etc.) (WMO, 2020). It is photo-dissociated in the stratosphere by ultraviolet radiation.

Halocarbons: Halocarbons are generally carbon compounds containing halogens such as chlorine and bromine, many of which are powerful greenhouse gases whose atmospheric concentrations have increased rapidly since the second half of the 20th century due to artificial production. Although their atmospheric concentrations are only around a millionth those of CO_2, their greenhouse effect per unit mass is several thousand times greater. Chlorofluorocarbons (CFC-11, CFC-12 and CFC-113 among others), carbon tetrachloride, hydrochlorofluorocarbons (HCFCs), 1,1,1-trichloroethane, chloromethane, halons and bromomethane are greenhouse gases and ozone-depleting substances (ODSs). Hydrofluorocarbons (HFC-134a, HFC-152a, etc.) are also included in the definition.

Montreal Protocol: The Montreal Protocol on Substances that Deplete the Ozone Layer (a protocol to the Vienna Convention for the Protection of the Ozone Layer) is an international treaty designed to protect the ozone layer by phasing out the production of numerous substances believed to be responsible for ozone depletion. The treaty was opened for signatures in 1987 and came into force in 1989. Since then, it has undergone several revisions. Japan ratified the protocol in 1988.

ppm, ppb, ppt: In this report, greenhouse gas concentrations are described in terms of mole fractions in units of ppm/ppb/ppt, representing the numbers of molecules of the gas per million/billion/trillion molecules of dry air, respectively.

Terms relating to water masses

North Pacific Subtropical Mode Water (NPSTMW) area: A thermostad between the seasonal and main thermoclines. The NPSTMW area is considered to form in the surface mixed layer just south of the Kuroshio Extension as a result of huge heat loss in winter. It is defined as an area of 16 – 18-degree water at depths of 100 to 400 m at around 20 to 30°N along the 137°E line.

North Pacific Intermediate Water (NPIW) area: The NPIW area forms in the mixed region between the Kuroshio Extension and the Oyashio front. It is defined as water with a salinity level of 34.0 or less at a depth of around 800 m at around 20 to 30°N along the 137°E line.

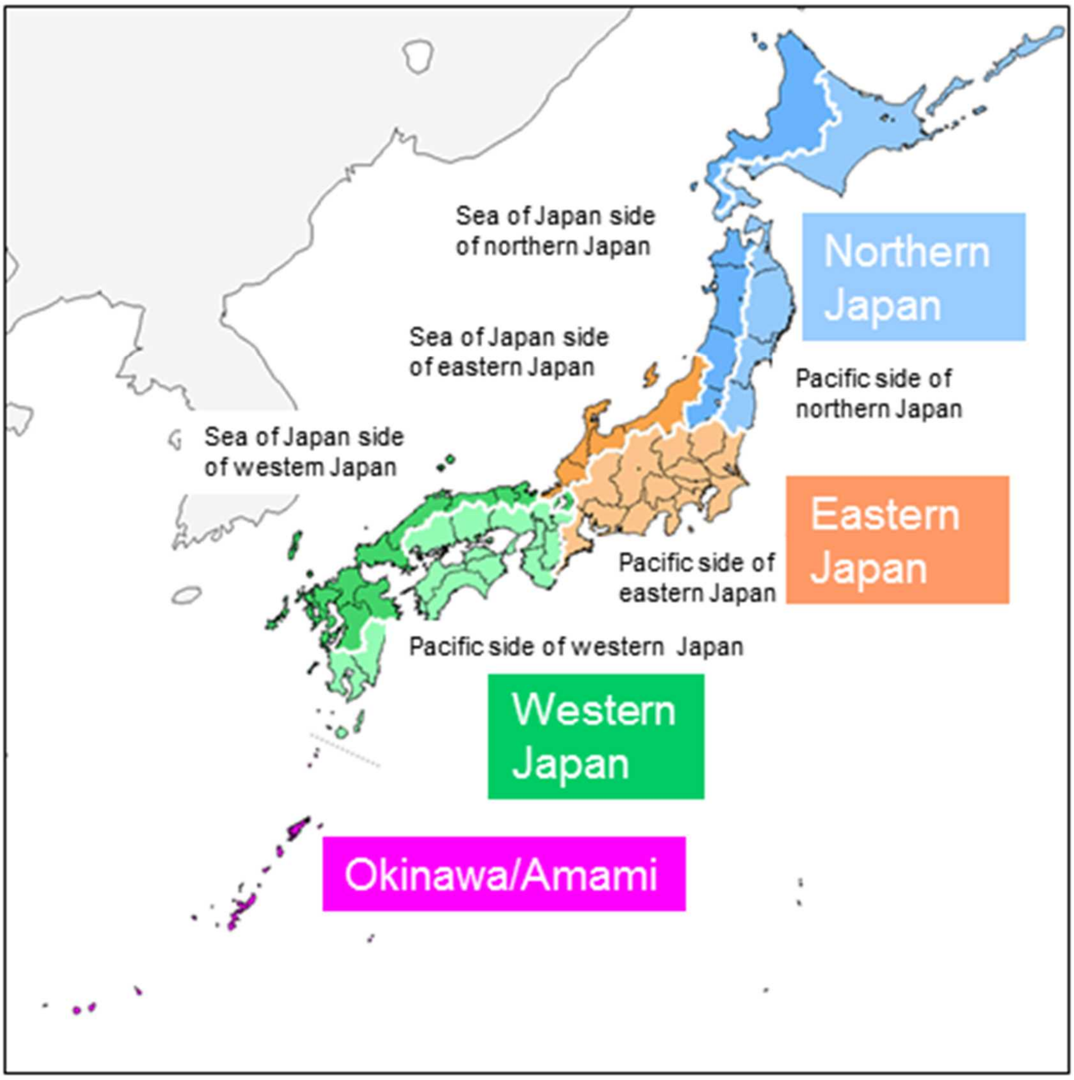

Names of Japanese regions used in this report

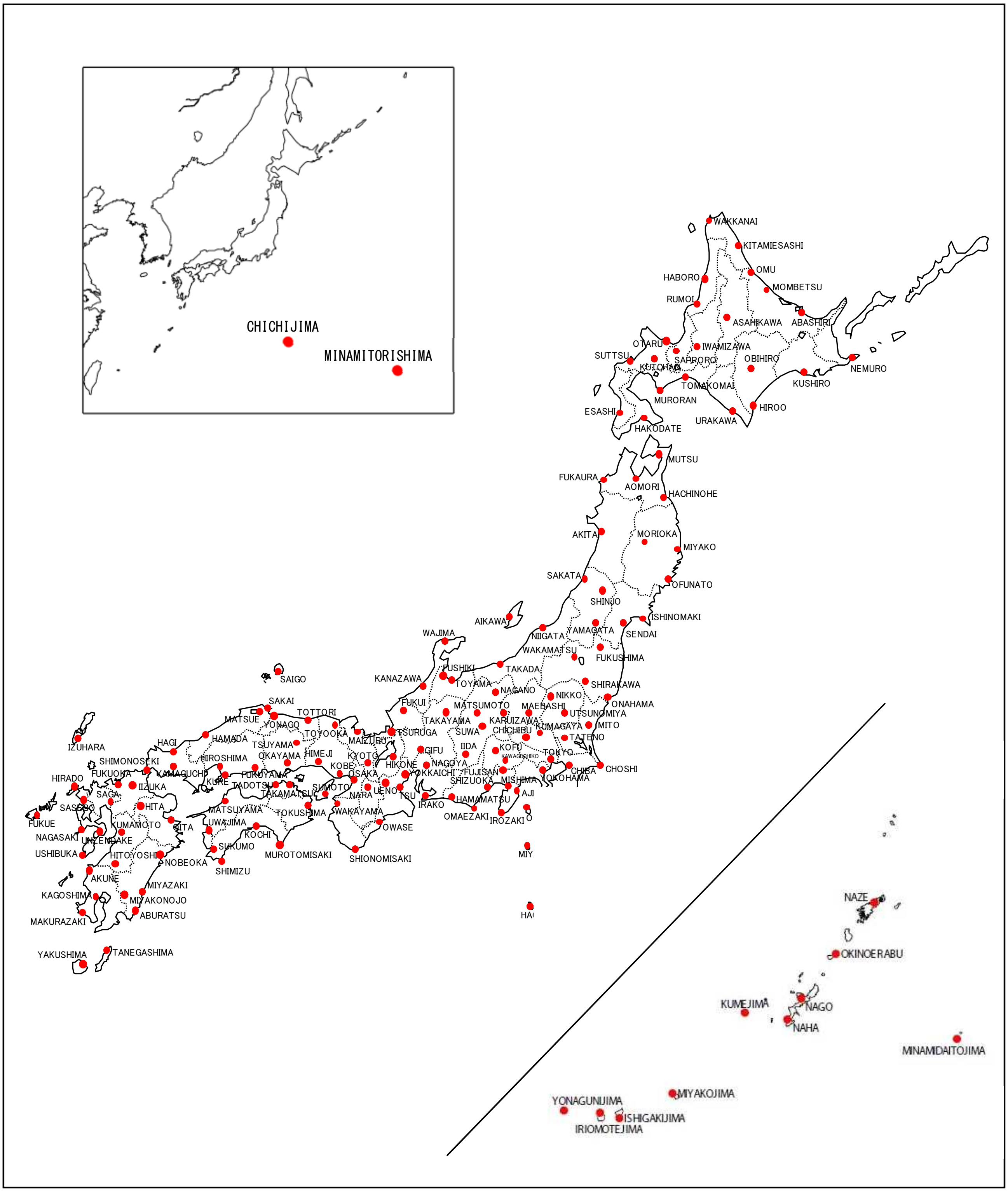

Distribution of surface meteorological observation stations in Japan

References

Topics

Hayashi, M., et al., 2021: The Northwestern Pacific Warming Record in August 2020 Occurred Under Anthropogenic Forcing. Geophys. Res. Lett., 48, doi: 10.1029/2020GL090956.

Chapter 1

EM-DAT: The OFDA/CRED International Disaster, Database – www.emdat.be – Université Catholique de Louvain – Brussels – Belgium

IPCC, 2013: Climate Change 2013: The Physical Science Basis. Contribution of Working Group I to the Fifth Assessment Report of the Intergovernmental Panel on Climate Change [Stocker, T.F., D. Qin, G.-K. Plattner, M. Tignor, S.K. Allen, J. Boschung, A. Nauels, Y. Xia, V. Bex and P.M. Midgley (eds.)]. Cambridge University Press, Cambridge, United Kingdom and New York, NY, USA, 1535 pp.

JMA, 1997: Monthly Report on Climate System, June 1997.

Chapter 2

IPCC, 2019: IPCC Special Report on the Ocean and Cryosphere in a Changing Climate [H.-O. Pörtner, D.C. Roberts, V. Masson-Delmotte, P. Zhai, M. Tignor, E. Poloczanska, K. Mintenbeck, A. Alegría, M. Nicolai, A. Okem, J. Petzold, B. Rama, N.M. Weyer (eds.)]. In press.

IPCC, 2013: Climate Change 2013: The Physical Science Basis. Contribution of Working Group I to the Fifth Assessment Report of the Intergovernmental Panel on Climate Change [Stocker, T.F., D. Qin, G.-K. Plattner, M. Tignor, S.K. Allen, J. Boschung, A. Nauels, Y. Xia, V. Bex and P.M. Midgley (eds.)]. Cambridge University Press, Cambridge, United Kingdom and New York, NY, USA, 1535 pp.

Mantua, N. J. and S. R. Hare, 2002: The Pacific decadal oscillation. J. Oceanogr., 58, 35–44.

Trenberth, K. E., J. M. Caron, D. P. Stepaniak and S. Worley, 2002: The evolution of El Niño–Southern Oscillation and global atmospheric surface temperatures, J. Geophys. Res., 107, D8, doi: 10.1029/2000JD000298.

Chapter 3

Dettinger, M. D. and M. Ghil, 1998: Seasonal and interannual variations of atmospheric CO_2 and climate. Tellus, 50B, 1–24.

Doney, S. C., V. J. Fabry, R. A. Feely and J. A. Kleypas, 2009: Ocean acidification: The other CO_2 problem, Annu. Rev. Mar. Sci., 1, 169–192, doi:10.1146/annurev.marine.010908.163834.

Friedlingstein, P., et al., 2020: Global Carbon Budget 2020, Earth Syst. Sci. Data, 12, 3269–3340, doi.org/10.5194/essd-12-3269-2020.

Iida, Y., et al., 2020: Global trends of ocean CO2 sink and ocean acidification: an observation-based reconstruction of surface ocean inorganic carbon variables. J. Oceanogr., doi.org/10.1007/s10872-020-00571-5.

IPCC, 2013: Climate Change 2013: The Physical Science Basis. Contribution of Working Group

I to the Fifth Assessment Report of the Intergovernmental Panel on Climate Change [Stocker, T.F., D. Qin, G.-K. Plattner, M. Tignor, S.K. Allen, J. Boschung, A. Nauels, Y. Xia, V. Bex and P.M. Midgley (eds.)]. Cambridge University Press, Cambridge, United Kingdom and New York, NY, USA, 1535 pp.

Ishii, M., et al, 2011: Ocean acidification off the south coast of Japan: A result from time series observations of CO2 parameters from 1994 to 2008, J. Geophys. Res., 116, C06022, doi:10.1029/2010JC006831.

Keeling, C. D., T. P. Whorf, M. Wahlen and J. van der Plicht, 1995: Interannual extremes in the rate of rise of atmospheric carbon dioxide since 1980. Nature, 375, 666–670.

Keeling, R. F., S. C. Piper, and M. Heinmann, 1996: Global and hemispheric CO_2 sinks deduced from changes in atmospheric O_2 concentration. Nature, 381: 218-221.

Kudo, R., et al, 2012: Aerosol impact on the brightening in Japan. J. Geophys. Res., 117(D07208), doi:10.1029/2011JD017158.

Le Quéré, C., et al., 2016: Global Carbon Budget 2016, Earth Syst. Sci. Data, 8, 605-649, doi:10.5194/essd-8-605-2016.

Montzka, S. A. et al., 2018: An unexpected and persistent increase in global emissions of ozone-depleting CFC-11, Nature, 557, 413-417, doi:10.1038/s41586-018-0106-2.

Niwa, Y., et al, 2014: Seasonal Variations of CO_2, CH_4, N_2O and CO in the Mid-Troposphere over the Western North Pacific Observed Using a C-130H Cargo Aircraft. J. Meteorol. Soc. Japan, 92(1), 50-70, doi:10.2151/jmsj.2014-104.

Norris, J. R. and M. Wild, 2009: Trends in aerosol radiative effects over China and Japan inferred from observed cloud cover, solar ‘‘dimming,’’ and solar ‘‘brightening,’’. J. Geophys. Res., 114(D00D15), doi:10.1029/2008JD011378.

Ohmura, A., 2009: Observed decadal variations in surface solar radiation and their causes. J. Geophys. Res., 114(D00D05), doi: 10.1029/2008JD011290.

Rayner, P. J., I. G. Enting, R. J. Francey, and R. Langenfelds, 1999: Reconstructing the recent carbon cycle from atmospheric CO_2, $\delta^{13}C$ and O_2/N_2 observations. Tellus, 51B, 213-232.

Rigby, M., et al., 2019: Increase in CFC-11 emissions from eastern China based on atmospheric observations, Nature, 569, 546-550, doi:10.1038/s41586-019-1193-4.

Saito, T., et al, 2015: Extraordinary halocarbon emissions initiated by the 2011 Tohoku earthquake. Geophys. Res. Lett., 42, doi:10.1002/2014GL062814.

Sweeney, C., et al., 2015: Seasonal climatology of CO_2 across North America from aircraft measurements in the NOAA/ESRL Global Greenhouse Gas Reference Network, J. Geophys. Res. Atmos., 120, 5155-5190, doi:10.1002/2014JD022591.

Tsuboi, K., et al, 2013: Evaluation of a new JMA aircraft flask sampling system and laboratory trace gas analysis system. Atmos. Meas. Tech., 6, 1257–1270, doi:10.5194/amt-6-1257-2013.

Umezawa, T., et al, 2018: Seasonal evaluation of tropospheric CO_2 over the Asia-Pacific region observed by the CONTRAIL commercial airliner measurements, Atmos. Chem. Phys., 18, 14851-14866, doi:10.5194/acp-18-14851-2018.

WCRP, 2010: Summary Report from the Eleventh Baseline Surface Radiation Network (BSRN) Scientific Review and Workshop. WCRP Informal Report No. 08/2010, 21 pp.

Wild, M., 2009: Global dimming and brightening: A review. J. Geophys. Res., 114(D00D16), doi:10.1029/2008JD011470.

Wild M. and A. Ohmura, 2004: BSRN longwave downward radiation measurements combined with GCMs show promise for greenhouse detection studies, GEWEX news, 14(4), 20pp.

WMO, 2009: Technical Report of Global Analysis Method for Major Greenhouse Gases by the World Data Center for Greenhouse Gases. GAW Report, 184, WMO/TD No.1473.

WMO, 2018a: Scientific Assessment of Ozone Depletion: 2018. Global Ozone Research and Monitoring Project-Report, 58.

WMO, 2018b: WMO Greenhouse Gas Bulletin No.14.

WMO, 2020: WMO Greenhouse Gas Bulletin No.16. http://www.wmo.int/pages/prog/arep/gaw/ghg/GHGbulletin.html

WMO, 2021: WMO WDCGG DATA SUMMARY, WDCGG No.45, GAW Data Volume IV-Greenhouse Gases and Other Atmospheric Gases, published by the Japan Meteorological Agency in co-operation with World Meteorological Organization. Available at https://gaw.kishou.go.jp/publications/summary. (in preparation)